International Journal of Heat and Mass Transfer 217 (2023) 124639

Contents lists available at ScienceDirect

International Journal of Heat and Mass Transfer

journal homepage: www.elsevier.com/locate/ijhmt

Review

Review of the dynamic Leidenfrost point temperature for droplet impact on a heated solid surface

Chang Cai [a], Issam Mudawar [b,*]

[a] Key Laboratory of Ocean Energy Utilization and Energy Conservation of Ministry of Education, School of Energy and Power Engineering, Dalian University of Technology, Dalian 116024, PR China
[b] School of Mechanical Engineering, Purdue University Boiling and Two-Phase Flow Laboratory (PU-BTPFL), 585 Purdue Mall, West Lafayette, IN 47907, USA

ARTICLE INFO

Keywords:
Dynamic Leidenfrost point temperature
Droplet impact
Vapor layer
Droplet rebound

ABSTRACT

Droplet impact on a high-temperature solid surface in the film boiling regime is widely encountered in various modern industrial and technological applications. The present article provides a systematic overview of the lower threshold of film boiling, the dynamic Leidenfrost point temperature, for a single impacting droplet. An extensive literature survey is conducted which includes both experimental and theoretical works. The first section of the review focuses on the parameter influences of the dynamic Leidenfrost point temperature, including impact conditions, surface characteristics, fluid properties, and the external environment. It is shown that, despite extensive prior work, there are many inconsistent conclusions regarding the effects of different parameters. Overall, contradictory experimental findings point to a need for future work using different types of fluids, and broad ranges of operating conditions and surface parameters. This is followed by a review of prior theoretical models which are derived using different fundamental hypotheses, including bubble nucleation theory, transient heat conduction, the vapor-gas layer analogy, and the pressure balance criterion, the majority of which are semiquantitative and rely on measured or simulated parameters for closure. In addition, measurement and modeling of the vapor layer thickness beneath an impacting droplet are discussed, which has a pivotal influence on the dynamic Leidenfrost phenomenon. It is concluded that future experimental investigations taking advantage of modern sophisticated imaging techniques are required to accurately capture the evolution and characteristics of the vapor layer. This information will play a crucial role in the development of a theoretical and experimentally-validated model for the dynamic Leidenfrost point temperature.

1. Introduction

1.1. Droplet impact on high-temperature surfaces

As a highly transient and multiscale process, droplet impact involves mutual interactions of mass, momentum, and energy between different phases. Therefore, this phenomenon has stimulated numerous investigations over the past few decades in pursuit of a detailed understanding of both its hydrodynamic and thermodynamic characteristics and mechanisms. Research showed that surface temperature exerts an important effect on droplet impact. Depending on the relative magnitude of surface temperature and liquid saturation temperature, an impacting droplet may experience *film evaporation, nucleate boiling, transition boiling,* or *film boiling* [1]. In different heat transfer regimes, the impacting droplet exhibits distinct heat transfer performance and morphological characteristics.

As illustrated in Fig. 1, droplet impact on a solid surface with an ultrahigh temperature is frequently encountered in various modern industrial and technological applications, where the definition of ultrahigh temperature is relative to the liquid saturation temperature. Examples include, but are not limited to, emergency core cooling in a loss-of-coolant accident of light water reactors [2,3], spray cooling of metal castings in the metallurgical industry [4,5] and for fire extinguishment [6,7], pre-cool of human skin with cryogenic refrigerants in laser treatments [8,9], thermal protection of high-power equipment [10,11] and precision machining [12], fuel droplet impact in internal combustion engines with direct fuel injection [13,14], water droplet impact on steam turbine blades [15], as well as urea-water-solution droplet impact during the selective catalytic reduction process [16,17].

Under these circumstances, the surface temperature is considerably higher than the coolant saturation temperature. Film boiling generally

* Corresponding author.
E-mail address: mudawar@ecn.purdue.edu (I. Mudawar).

https://doi.org/10.1016/j.ijheatmasstransfer.2023.124639
Received 29 April 2023; Received in revised form 18 July 2023; Accepted 23 August 2023
Available online 5 September 2023

Nomenclature

A	parameter in Table 5 [-]
B_1, B_2	parameter in Table 5 [-]
C	parameter in Table 5 [-]
c	sound velocity in liquid [m/s]
c'	sound velocity in vapor [m/s]
c_p	constant-pressure specific heat [J/(kg·°C)]
Bo	Bond number [-]
D	micropillar diameter [μm]
d	droplet diameter [mm]
E	parameter defined in Eq. (23) [-]
e	thermal effusivity [$W{\cdot}s^{1/2}/(°C{\cdot}m^2)$]
G	parameter defined in Eq. (12) [-]
g	gravitational acceleration [m/s^2]
H	microstructure height [μm]
H_0	impact height [mm]
h	heat transfer coefficient [$W/(m^2{\cdot}°C)$]
h_0	height of the center of gravity [mm]
h_{fg}	latent heat of vaporization [J/kg]
h''_{fg}	modified latent heat of vaporization [J/kg]
K	parameter defined in Eq. (12) [-]
K_p	permeability [m^2]
K_{UC}	effective permeability in a unit cell [m^2]
k	accommodation coefficient [-]
L	microstructure spacing [μm]
J	heterogeneous nucleation rate [$m^{-3}{\cdot}s^{-1}$]
Ja	Jacob number [-]
m	mass [kg]
Nu	Nusselt number [-]
n	exponent [-]
Oh	Ohnesorge number [-]
P	pressure [Pa]
Pr	Prandtl number [-]
q	heat flux [W/m^2]
Re	Reynolds number [-]
R	droplet radius [mm]
R_a	average height of surface roughness [μm]
R_p	peak height of surface structures [μm]
R_q	root mean square roughness [μm]
R_{UC}	thermal conduction resistance [$m^2{\cdot}°C/W$]
r_c	critical bubble radius [mm]
S	microchannel wall width [μm]
St	Stokes number [-]
T	temperature [°C]
T^*	temperature defined in Eq. (11) [°C]
t	time [s]
u	velocity [m/s]
v	vapor production rate [m/s]
We	Weber number [-]
W	microchannel width [μm]
z	vertical coordinate [m]

Greek symbols

α	impact angle [°]
β	adjustable parameter in Eq. (21) [-]
δ	thickness [μm]
ε	surface porosity [-]
η	adjustable coefficient in Eq. (16) [-]
θ	contact angle [°]
λ	thermal conductivity [W/(m·°C)]
ξ	acceleration [m/s^2]
ρ	density [kg/m^3]
σ	surface tension [N/m]
ψ	parameter in Table 5 [-]
φ	trapezoidal groove angle [°]
χ	mass proportion in Eq. (20) [-]

Subscripts

0	initial
a	air
c	contact
D	dynamic
d	dimple region
f	fluid
g	vapor
imp	impact
LFP	Leidenfrost point
max	maximum
min	minimum
n	neck region
r	residence
ref	reference
sat	saturation
sp	spinodal
th	thermal
WH	water hammer
w	heated surface

Superscript

eff	effective

Abbreviations

CA	contact angle [°]
CMC	critical micelle concentration [mol/L]
erfc	complementary error function
dpm	droplets per minute
LFP	Leidenfrost point

occurs when the droplet is separated from the heated wall immediately upon impact by a continuous insulating vapor layer. In this case, film boiling is also referred to as the Leidenfrost effect, and the levitating droplet is called the Leidenfrost droplet. Due to the low thermal conductivity of the vapor layer, heat transfer significantly deteriorates in the film boiling regime, which may cause serious safety challenges. With a decreased surface temperature due to the cooling effect, the vapor layer becomes unstable and discontinuous, and local direct liquid-solid contact is induced in the transition boiling regime. Heat transfer is then dramatically enhanced and a more rapid decrease in the surface temperature can be achieved. Therefore, the Leidenfrost effect is undesirable for cooling purposes, and it is important to exit the film boiling regime as early as possible to ensure safety and reliability.

On the other hand, the thermally-induced hydrophobicity in the film boiling regime has been widely utilized in the area of material transportation and microfluidic systems. The superior mobility of its non-wetting behavior makes it possible for the droplet to frictionlessly self-propel in a preferential direction controlled by either thermal gradients [18] or asymmetric surface topologies [19–21]. Leidenfrost droplets can also be used for power generation [22], nanomaterial fabrication [23], phase-change modulated thermal switch [24], chemical reaction acceleration [25], vibration isolation [26], and ultrasensitive Raman spectroscopy detection [27], where in all cases the Leidenfrost effect is favorable. Consequently, understanding the fundamentals of droplet impact in the film boiling regime and postponing and/or accelerating the transition from film boiling to transition boiling

are of essential significance both in terms of theory and practice.

1.2. Dynamic Leidenfrost point temperature

Early insight into the Leidenfrost phenomenon, i.e., film boiling of a single droplet, dates back to the pioneering work of J.G. Leidenfrost [28], who observed water droplet levitation on a sufficiently hot iron spoon by an evaporative vapor layer. This experimental finding acted as a foundation for follow-up studies on the droplet impact Leidenfrost phenomenon. The lower limit for the Leidenfrost effect, or the demarcation between film boiling and transition boiling, is generally known as the Leidenfrost point (LFP) temperature. To differentiate the LFP temperatures associated with sessile and impacting droplets, the term *dynamic LFP temperature* is used for the latter case in this paper. It is noted that several other terms have also been used in previous studies to denote the dynamic LFP temperature (T_{LFP}), although they may not be exactly synonymous, e.g., wetting transition temperature [29], lift-off temperature [30,31], rewetting temperature [32], boiling crisis temperature [33], and dry rebound temperature [34].

A commonly used technique to determine the dynamic LFP temperature relies on the droplet evaporation curve from the thermodynamic perspective, with which different heat transfer regimes can be distinguished over a wide range of surface temperatures. As shown in Fig. 2(a), the dynamic LFP temperature corresponds to the local maximum droplet evaporation time [35–37]. However, different from a sessile droplet, accurate measurement of the evaporation time of an impacting droplet over a wide range of surface temperatures is sometimes difficult, especially when the dynamic LFP temperature is approached with diversified droplet patterns. The impacting droplet may undergo rebound, breakup, atomization, and some more intricate compound behaviors rather than always deposition on the heated surface, which may cause considerable uncertainty when measuring evaporation time. Staat et al. [38] indicated that the most accurate method to determine the dynamic LFP temperature is to measure the vapor layer directly, and the critical temperature can be identified by observing whether there is any liquid-solid contact [39–43], as shown in Fig. 2(b). As will be discussed in Section 4, the vapor layer thickness ranges from a few hundred nanometers to a few dozen micrometers within a few milliseconds after droplet impact. This brings forward high demand for both high spatial and temporal resolutions of optical equipment to ensure measurement accuracy.

Instead, the simpler and more practical hydrodynamic criterion is more prevalent to identify the dynamic LFP temperature, which is equal to the lowest surface temperature at which droplet rebound or breakup occurs without atomization or splash [44–48]. In the transition boiling regime, numerous atomized tiny droplets can be observed whether the droplet finally rebounds from the surface or breaks up into several parts depending on the impact momentum (see Fig. 2(c)). This is caused by vigorous bubble nucleation triggered by local liquid-solid contact underneath the droplet. While in the film boiling regime, with a continuous vapor layer that completely prevents liquid-solid contact, the droplet will spread and recoil laterally, then either rebound or break up while the atomization phenomenon disappears. Therefore, transition/film boiling regimes and the dynamic LFP temperature can be identified. It should be noted that atomization may also occur during film boiling, which is called spray film boiling by Tran et al. [49], at surface temperatures much higher than the measured dynamic LFP temperature with high Weber numbers. Overall, the hydrodynamic criterion prevails for dynamic LFP temperature determination according to many researchers.

As mentioned previously, a high dynamic LFP temperature is beneficial to achieve an earlier transition from film boiling to transition boiling for efficient cooling purposes. However, superior heat transfer seems incompatible with a high dynamic LFP temperature to some extent. To ensure the safe and stable operation of the high-temperature equipment, heat needs to be rapidly and continuously dissipated from the hot surface. This process will contribute to massive vapor production, which in turn impedes liquid-solid contact and is disadvantageous

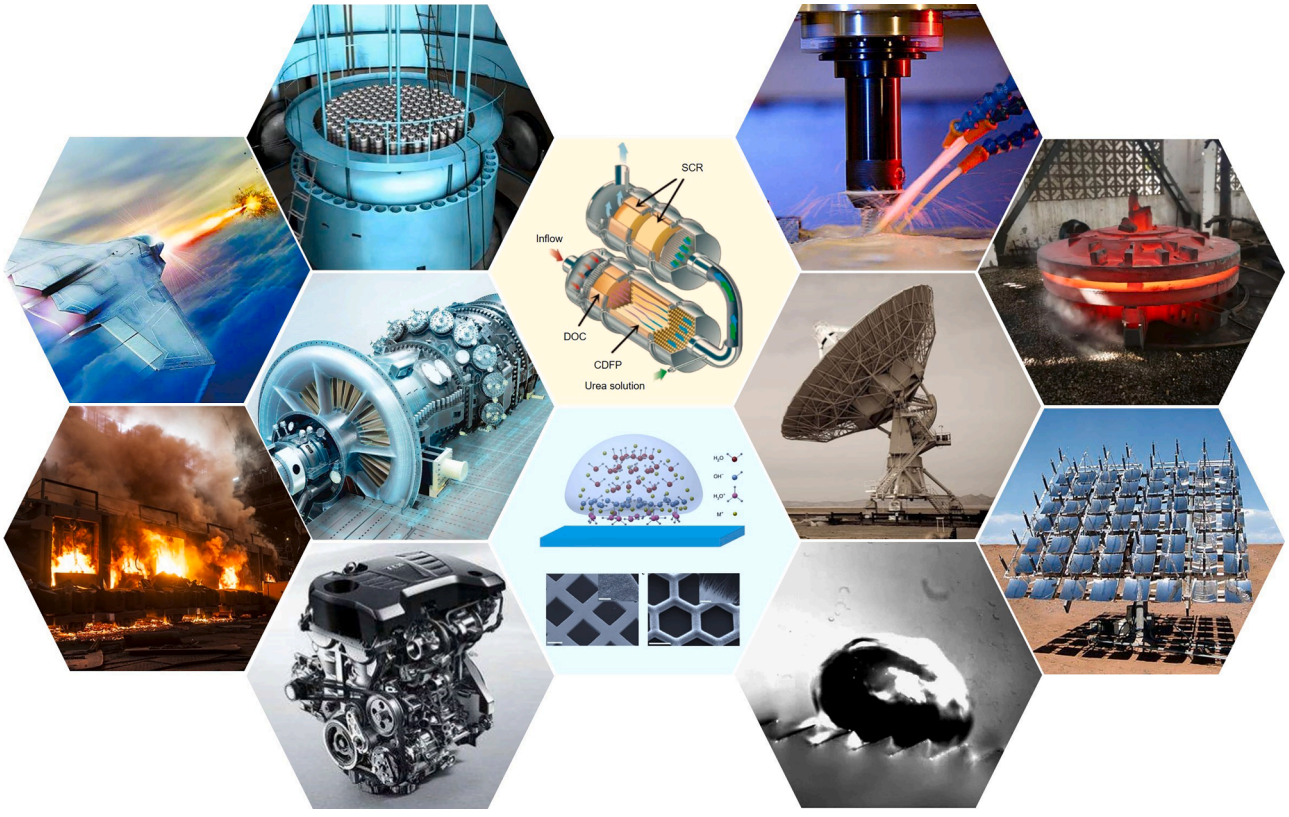

Fig. 1. Examples of applications involving droplet impact on high-temperature surfaces.

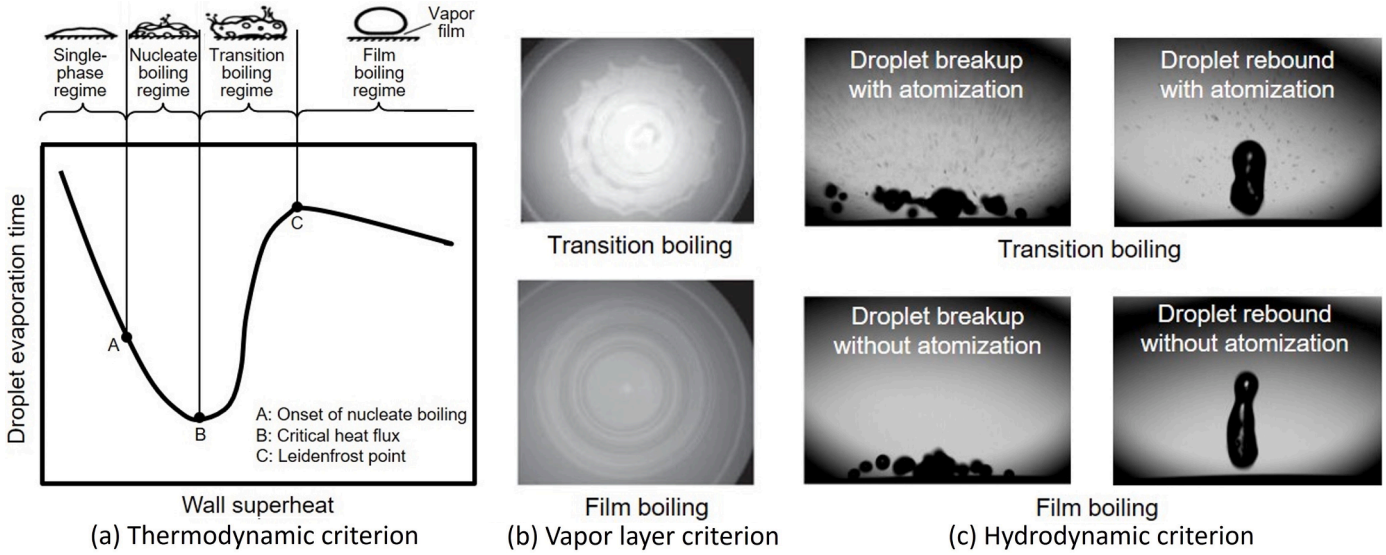

Fig. 2. Identification of dynamic LFP temperature: (a) the thermodynamic criterion, (b) the vapor layer criterion adapted from Wang et al. [39], and (c) the hydrodynamic criterion.

for increasing the dynamic LFP temperature. Therefore, elevating the dynamic LFP temperature without sacrificing heat transfer capacities remains an urgent issue to achieve high-efficiency cooling.

Several review articles concerning the Leidenfrost effect of a single droplet have been published in the past, most of which are dedicated entirely to a sessile droplet, while others incidentally mention the dynamic cases. A pioneering study by Bernardin and Mudawar [50] summarized and assessed the prediction models of the sessile droplet LFP temperature. Zhong and Guo [51], as well as Talari et al. [52], focused primarily on the effect of surface topography and wettability on sessile droplet LFP temperature and also discussed the underlying mechanisms. Quéré [53] reviewed the fundamentals of a sessile Leidenfrost droplet, including the interfacial hydrodynamics, vapor layer flow, droplet shape, stability and motion.

Some investigations also provided a comprehensive review of droplet behaviors accompanied by the Leidenfrost phenomenon. For instance, the droplet bouncing dynamics [54] and self-propulsion mechanisms [55] in the film boiling regime were addressed in detail. Recently, Stewart [56] elaborated on various dynamic motions of a Leidenfrost droplet, including gliding, spinning, self-propulsion, bobbing and bouncing, vibrating star-shaped patterns, fluttering and humming, crackling and explosion, as well as droplet internal motion.

1.3. Objective of the present study

To the best knowledge of the present authors, the dynamic LFP temperature for an impacting droplet has not been reviewed so far. The present paper will systematically review both experimental and theoretical studies on the dynamic LFP temperature, as well as some critical issues concerning the thin vapor layer thickness beneath the impacting droplet. This review is limited to the case of a single droplet impact on a solid surface and excludes liquid films (pre-wet walls), deep liquid pools, and spray impacts.

Unlike the aforementioned reviews, the present study summarizes the parametric influence of impact parameters, surface characteristics, fluid properties, and external conditions on the dynamic LFP temperature. The triggering mechanisms, available prediction models, and correlations will be also reviewed. In addition, the modeling and measurement of vapor layer thickness formed between the dynamic Leidenfrost droplet and the heated surface are discussed. Finally, recommendations for future research are proposed.

2. Experimental studies on dynamic LFP temperature

Extensive experimental investigations have been conducted on the dynamic LFP temperature for a single droplet impact on a solid surface in the past few decades. Most studies focus on the influencing factors, which can be categorized into four types as shown in Fig. 3, including the impact parameters, fluid properties, surface characteristics, and external conditions, which will be elaborated on in this section. Generally, these factors can have a combined effect on the dynamic LFP temperature, which further complicates the underlying mechanism.

Considering so many influencing parameters, several dimensionless numbers are frequently adopted for ease of analysis. Typical examples include the Weber, Reynolds, Ohnesorge, Bond, and Jacob numbers, which are respectively expressed as [57]

$$\mathrm{We} = \frac{\rho_f u^2 d}{\sigma} = \frac{\text{Inertia force}}{\text{Surface tension force}} \tag{1}$$

$$\mathrm{Re} = \frac{\rho_f u d}{\mu_f} = \frac{\text{Inertia force}}{\text{Viscous force}} \tag{2}$$

$$\mathrm{Oh} = \frac{\mathrm{We}^{1/2}}{\mathrm{Re}} = \frac{\mu_f}{\sqrt{\rho_f d \sigma}} = \frac{\text{Viscous force}}{\text{Surface tension force}} \tag{3}$$

$$\mathrm{Bo} = \frac{\rho_f g R^2}{\sigma} = \frac{\text{Gravitational force}}{\text{Surface tension force}} \tag{4}$$

$$\mathrm{Ja} = \frac{\rho_f c_{pf}(T_w - T_{sat})}{\rho_g h_{fg}} = \frac{\text{Sensible heat}}{\text{Latent heat of vaporization}} \tag{5}$$

where ρ_f, σ, μ_f, c_{pf}, T_{sat}, and h_{fg} are, respectively, droplet density, surface tension, viscosity, constant-pressure specific heat, saturation temperature, and latent heat of vaporization. As for the remaining, g and T_w are the gravitational acceleration and surface temperature, while d, R, and u are the droplet diameter, radius, and impact velocity, respectively.

2.1. Effects of impact parameters

In different application scenarios, a single droplet impact occurs under diverse conditions with wide ranges of impact velocity, impact angle, and impact frequency, the effects of which are summarized in this section.

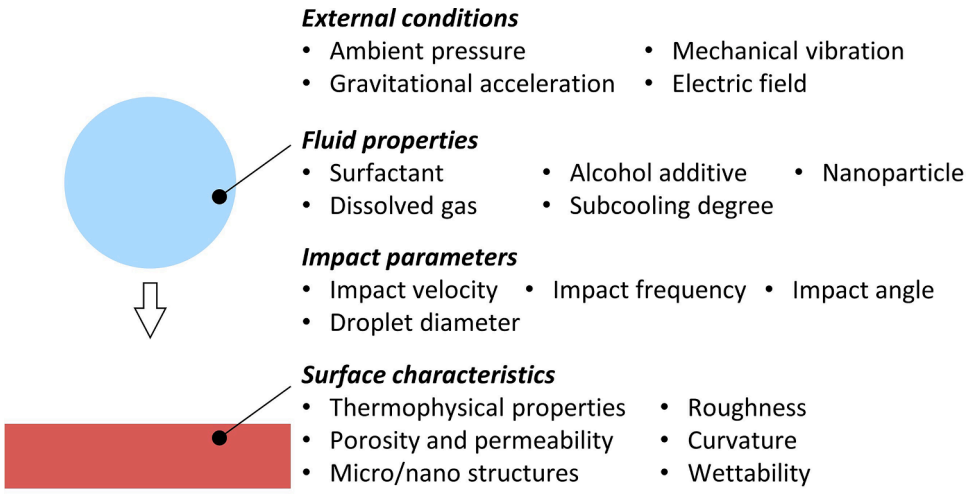

Fig. 3. Influencing factors on the dynamic LFP temperature of droplet impact.

2.1.1. Impact velocity

In experimental investigations, different impact velocities are generally realized by changing the impact height, or equivalently, the impact momentum. Fig. 4 summarizes the measured dynamic LFP temperature in some previous studies, and it is seen that no consensus has been reached concerning the impact velocity effect. It is commonly recognized, by a majority of studies, that an increased impact velocity corresponds to a higher dynamic LFP temperature, while the increment can be dramatical [34,45,46,49,58-61], slight [14,30], or dependent on the velocity range [39,62,63], just to name a few of the findings. This can be explained by the fact that for an impacting droplet with a large velocity, the vapor beneath the droplet is compressed to a greater extent and can be squeezed out more easily. Thus, more vapor should be generated to prevent droplet-solid contact. Also, a higher impact momentum enhances droplet spreading to form a thinner liquid lamella, which is vulnerable to bubble bursting. Thus, a higher dynamic LFP temperature is required.

On the other hand, many researchers, such as Chaves et al. [31], Manzello and Yang [64], Castanet et al. [65], Nagai et al. [66], Staat et al. [38], Sen et al. [67], Börnhorst et al. [68], Wu et al. [44], Zhang et al. [69] and Chausalkar et al. [70], reported a negligible effect within a wide range of impact velocity. It was further indicated that the critical temperature for the nonwetting droplet impact with no direct liquid-solid contact is even lower than the static LFP temperature determined from the sessile droplet evaporation curve [71,72].

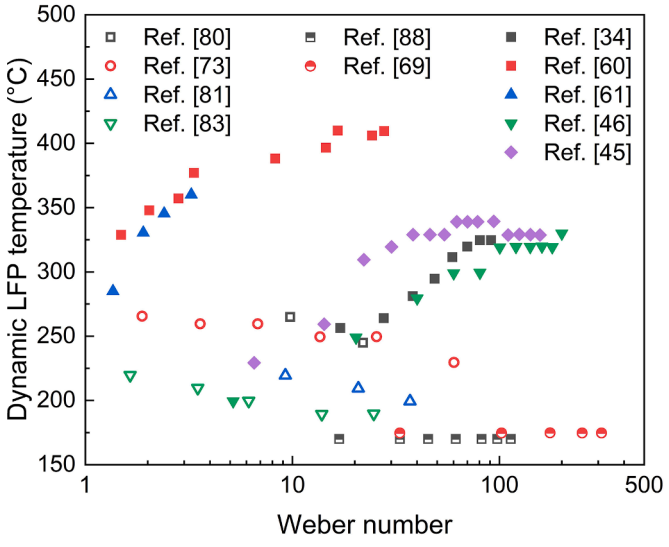

Fig. 4. Variation of dynamic LFP temperature with Weber number for pure water droplet impact on smooth substrates without any surface modification. The Weber number is changed solely by altering the impact velocity. Hollow, semi-hollow, and solid symbols indicate the experimental data with downward, invariable, and upward trends, respectively.

Nevertheless, the experimental results presented by Celata et al. [73], Mezbah et al. [74], Kompinsky et al. [75], Tong et al. [76], Jowkar et al. [77–79], Lee et al. [42], Dhar et al. [80], Kuhn et al. [16], Prasad et al. [81], as well as Luo et al. [82] demonstrated a totally different trend where the dynamic LFP temperature decreases either considerably or slightly with an increased impact velocity. It is speculated that improved spreading caused by higher impact velocities induces a larger contact area available for heat transfer [80,81]. Accordingly, the effective availability of nucleation sites at the liquid-solid interface increases, which benefits vapor layer formation and leads to droplet rebound at a lower dynamic LFP temperature. Prasad et al. [83] noticed that a higher impact velocity increases the area of nanoparticulate residue deposition under a nanoparticle-added droplet, while the significant increment in the nucleation sites promotes bubble coalescence and accelerates vapor layer formation. A similar trend was also found by the same authors for the nanobubble-dispersed impacting droplets [84]. Wang et al. [71,72] attributed the decreased dynamic LFP temperature within the low-velocity range to the squeeze film effect. They regarded the vapor layer as a spring to bounce the droplet. The squeezing effect weakens at a lower impact velocity, and the spring force becomes smaller while the damping force dominates. Therefore, a higher temperature is required to intensify vapor generation.

Meanwhile, Lamini et al. [85], Shirota et al. [41], and Gonzalez Recio [62] pointed out that the impact velocity effect is relevant to the liquid type, e.g., negligible influence for ethanol and FC-72 (Fluorinert™ Electronic Liquid) but significant enhancement for water and FC-84. This dependence may stem from the different evaporation and spreading characteristics of liquids with diverse thermophysical properties, including surface tension, latent heat of vaporization, and liquid density, for example.

It is inferred from the impact regime map by Zhang et al. [86] that the effect of impact velocity on the dynamic LFP temperature is related to the surface texture. For example, the dynamic LFP temperature seems to decrease first and then increase with impact velocity on flat silicon, but increases monotonously on dense micropillar arrays, and remains nearly constant on sparse micropillar arrays. The case is even more complex for micropillar surfaces with superhydrophobic graphene nanosheet coating. Later, Clavijo et al. [87] revealed a wettability-related effect, i.e., the dynamic LFP temperature increases

on the whole with impact velocity on superhydrophilic, hydrophilic, and hydrophobic substrates, but exhibits no difference on superhydrophobic surfaces. More recently, Zhou et al. [88] found that the dynamic LFP temperature remains unchanged on plain titanium surfaces, but increases with impact velocity on nanotube surfaces.

2.1.2. Impact angle

In some practical applications, the coolant droplet may impact a heated surface with various inclinations. Compared to a perpendicular impact, the droplet also slides along the substrate with concurrent spread or retraction under the oblique impact condition. To avoid any ambiguity, the impact angle in this section is defined as the angle between the droplet impact velocity vector and the normal direction of the heated surface, i.e., an impact angle of 0° corresponds to the normal impact.

Yao and Cai [32] experimentally found that a small impact angle of less than 45° induces an insignificant reduction, while further increasing inclination obviously lowers the dynamic LFP temperature. This is due to the more pronounced effect of the tangential velocity component, which contributes to gas entrainment beneath the droplet. This gas layer resembles a vapor layer that insulates droplet-solid contact and reduces the dynamic LFP temperature for less vapor production.

Subsequently, this trend was further corroborated by Celata et al. [73]. Wang et al. [39] indicated that the decrease in the dynamic LFP temperature associated with an inclined impact is caused by a lower effective impact velocity. It is interesting to note in Fig. 5 that the measured data at different impact angles collapse roughly onto a single curve when the Weber number is calculated based on the perpendicular velocity component.

2.1.3. Impact frequency

Some researchers conducted droplet stream impact experiments and attempted to figure out the dependence of dynamic LFP temperature on the impact frequency. Both Bernardin et al. [89,90] and Senda et al. [91] reported a negligible effect, while the experimental results by Zhang et al. [92] demonstrated that the dynamic LFP temperature was elevated by increasing the impact frequency.

The possible reason for this contradiction might be relevant to the relative magnitude of the residence time, t_r, which spans the moments from droplet impact to rebound, to the time interval Δt between the impact of two successive droplets. Using the freely oscillating approximation [93] for simplicity, the residence time expressed as $t_r = \pi/4$ $(\rho_f d^3/\sigma)^{1/2}$ is approximately 15 ms and 1 ms for water droplets with diameters of 3.0 mm [89,90] and 0.5 mm [91], respectively, which are relatively shorter than a Δt of 400 ms (150 dpm) [89,90] and 66.7 ms (900 dpm) [91]. Therefore, the subsequent droplet does not interact with the former one, and the impact condition is equivalent to a single droplet with no frequency effect. With a high impact frequency of 71–72 kHz [92], t_r (0.15–0.22 ms for 0.139–0.181 mm water droplets) is longer than the Δt (0.08–0.14 ms). That is, the inevitable interaction between successive droplets will significantly affect heat transfer and impact hydrodynamics. The orderly droplet stream induces periodical vapor release, which is unfavorable for the formation of a continuous vapor layer. Therefore, the dynamic LFP temperature is greatly elevated.

Although beyond the scope of the present review, it is noted that the identification method of the dynamic LFP temperature for high-frequency droplet streams (e.g., Zhang et al. [92]) is completely different from that for a single droplet. In the former case, the droplet splash angle decreases linearly with increased surface temperature when approaching the dynamic Leidenfrost condition. Once the splash angle reaches a minimum value, the appearance of stable and orderly splash morphology and abrupt heat transfer deterioration designates the dynamic LFP temperature.

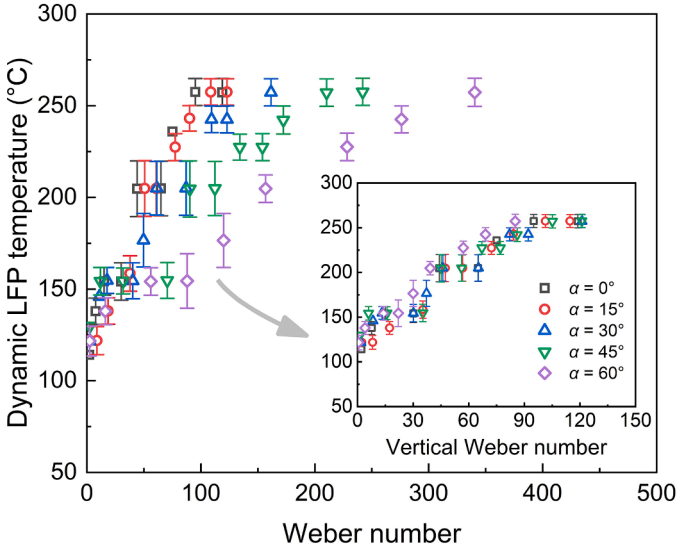

Fig. 5. Effect of the impact angle on the dynamic LFP temperature. Adapted from Wang et al. [39]. $\alpha = 0°$ corresponds to the normal impact.

2.1.4. Droplet diameter

It is generally accepted that with a larger droplet diameter, the Weber number increases and in turn elevates the dynamic LFP temperature. Since a larger droplet size prolongs the residence time and spreading diameter, it is less likely to form a vapor layer when the droplet retracts to a spherical shape before rebounding from the substrate. Thus, the dynamic Leidenfrost condition is achieved at a higher surface temperature [94].

Nevertheless, Tamura et al. [95], as well as Xiong and Yuan [96] showed that the dynamic LFP temperature is mostly independent of droplet diameter for a wide range of liquid types. Deng and Gomez [97] observed the rebound of electrically charged nanoliter droplets and the adhesion of picoliter droplets at the same surface temperature. Recall the hydrodynamic criteria that the dynamic LFP temperature can be regarded as the lowest temperature for droplet rebound. It is inferred that a smaller droplet diameter corresponds to a higher T_{LFP} value, which is contrary to the broad consensus for impacting droplets without electric charge. They suggested that the impact time is longer than the charge relaxation time for a larger droplet, for which charge transport occurs during droplet-surface contact, and the effect of image force on postimpact behaviors is negligible. However, smaller droplets are subject to the image force, therefore, droplet rebound is significantly suppressed.

2.2. Effects of surface characteristics

Since the dynamic Leidenfrost effect is closely related to the interaction between the droplet and heated substrate, a considerable amount of effort has been devoted to the effect of surface characteristics on the dynamic LFP temperature.

2.2.1. Thermophysical property

Experimental results showed that the dynamic LFP temperature can be quite different on heated substrates with similar roughness parameters but diverse surface materials [2,98]. Therefore, it is speculated that solid thermophysical properties play a significant role. The dynamic LFP temperature was found to remarkably increases on aged die surfaces [94], where the aging effect mainly lowers the thermal conductivity of the surface oxidation layer relative to the bare steel. However, when comparing the dynamic LFP temperatures on aluminum, copper, and stainless steel surfaces, Lamini et al. [85] found that T_{LFP} is not related to surface thermophysical properties. They stated that the possible reason may be the inevitable forming and gradual thickening of the oxidation layer with increased surface temperature during the experiment on stainless steel and copper substrates.

Several other investigations found that the dynamic LFP temperature is higher on surfaces with a lower thermal effusivity [3,44,99], which is a dominant factor rather than the solid thermal diffusivity [44], capillary wicking, and permeability effects [99]. Wu et al. [44] further demonstrated that the increase in the dynamic LFP temperature with impact velocity is more remarkable on surfaces with lower thermal effusivity. The solid thermal effusivity, which is expressed as $e_w = (\rho_w c_{pw} \lambda_w)^{0.5}$, indicates how fast the substrate is able to transfer heat to the droplet [100]. Therefore, the droplet-solid interfacial temperature will decrease as the thermal effusivity decreases. To produce enough vapor for droplet levitation, a higher interfacial temperature, and, accordingly, a higher dynamic LFP temperature is required.

Considering heat transfer between the impacting droplet and the heated surface, the substrate temperature may decrease due to droplet cooling. Baumeister and Simon [101] classified solid surfaces into three categories: isothermal (e.g., aluminum), intermediate (e.g., stainless steel), and non-isothermal (e.g., glass). Generally, metallic surfaces can effectively eliminate the non-isothermal effect during droplet impact, but it is disadvantageous to directly identify the liquid-vapor interface compared to transparent nonmetals [63]. Limbeek et al. [102,103] observed a delayed touch-down phenomenon where the droplet is levitated initially but shortly regains contact for ethanol droplet impact on the glass surface. They supposed that this is caused by significant cooling during the early stage of droplet impact on glass with poor heat transport characteristics, which results in a decrease in the surface temperature. Moreover, this effect occurs only when the thermal time scale $t_{th} = \lambda_w \rho_w c_{pw} h^{-2}$ is smaller than the impact time scale $t_{imp} = d/u$, where h is the heat transfer coefficient. Therefore, a higher dynamic LFP temperature is required under these conditions. However, they indicated that for microscale droplets with $t_{imp} < t_{th}$, the heated surface can also be considered isothermal during the impact process. This conclusion was confirmed by Shirota et al. [41] since the dynamic LFP temperature on sapphires with relatively higher heat transport properties is lower by about 50 K than that on glass [43].

Incidentally, a similar cooling effect is also noteworthy for droplet impact on a thin substrate [102], which corresponds to a higher dynamic LFP temperature. As shown in Fig. 6, the cooling front penetrates through the thin substrate where heat can only be provided from the periphery of the impact area, while a thick substrate can provide heat from below. Misyura [104] indicated that this cooling effect is related to the ratio of droplet diameter to substrate thickness.

2.2.2. Surface roughness

Table 1 summarizes the experimental conditions of some previous studies on the surface roughness effect. It is widely recognized that the static LFP temperature increases with increasing surface roughness [50,105] since surface protrusions play an important role in penetrating the vapor layer underneath a sessile droplet [106]. However, the case is much different for an impacting droplet. Decreased dynamic LFP temperatures were reported by the same authors on similar surfaces to that in sessile droplet experiments (i.e., polished, particle-blasted and rough-sanded copper [89,90], and polished aluminum with different classes [105]). They believed that higher surface roughness is disadvantageous to the stability of the liquid frontal edge during droplet spreading, which would result in droplet disintegration. As a result, the pressure under the impacting droplet decreases, which requires a lower surface temperature to attain the critical dynamic Leidenfrost state. The same trend was also observed in a recent study by Wang et al. [2] on CVD-SiC surfaces grinded with different diamond pastes, where they observed droplet contact with the protruding roughness during droplet receding and the resultant secondary atomization. The contradiction between sessile and impacting droplets also probably originates from the fact that the dynamic LFP temperature dependence on surface roughness is subject to many other factors. For instance, the relative magnitude of roughness height to droplet height during spreading will undoubtedly affect the possibility of either droplet disintegration or vapor layer penetration by the surface features.

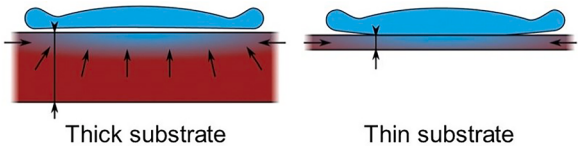

Fig. 6. Droplet impact on silicon substrates with different thicknesses [102]. The thermal boundary layer in the solid phase is indicated in blue, where the arrows show the dominant heat fluxes. (For interpretation of the references to colour in this figure legend, the reader is referred to the web version of this article.)

Table 1
Experimental conditions for prior studies centered on surface roughness effects on the dynamic LFP temperature.

Reference	Liquid type	Surface condition	Test conditions
Dynamic LFP temperature decreasing with increasing surface roughness			
Bernadin et al. [89,90]	water	copper (R_a = 0.097–2.96 μm)	We = 20–220
Misyura [105]	water	aluminum (R_q = 0.04–6 μm)	We = 8–110
Wang et al. [2]	water	CVD-SiC (R_q = 5.4–10.5 μm)	We = 10–120
Dynamic LFP temperature increasing with increasing surface roughness			
Zabala et al. [94]	lubricant	steel (R_a = 0.025–1.85 μm)	We = 9–64
Lee et al. [107]	water	zirconium (R_a = 0.36–1.9 μm)	We = 7.6
Guo et al. [108]	diesel	aluminum alloy (smooth and etched)	H_0 = 10 mm

Some researchers, however, hold a contrary opinion since they have found that the dynamic LFP temperature increases with surface roughness. Zabala et al. [94] proposed that a higher surface roughness hinders the droplet-solid contact and weakens heat transfer. Therefore, a higher surface temperature is needed to generate sufficient vapor to attain the dynamic Leidenfrost effect. It is known that different treatments to obtain different roughness levels may also simultaneously change the surface wettability and thermophysical properties. For instance, a higher surface roughness generally improves the hydrophilicity of a hydrophilic surface, while a hydrophobic surface will be more hydrophobic. Lee et al. [107] successfully separated the surface roughness effect from the wetting characteristics. They polished zirconium surfaces with different abrasive papers to achieve similar wettability (with water contact angles of 7° and 11°) but different roughness levels. It was observed that the rougher surface elevates the dynamic LFP temperature. They proposed that microscale roughness induces additional friction that impedes droplet retraction and in turn causes a longer contact time, prolonging the transition boiling regime. The same trend was observed by Guo et al. [108], and the surface roughness effect is similar to the case of a sessile droplet discussed in Ref. [106]. Considering the aforementioned contrary conclusions, it is unclear whether surface roughness could increase the dynamic LFP temperature and still needs further investigation.

Also, it should be noted that the surface roughness discussed in this section is randomly distributed without any additional surface modifications, which is different in terms of its physical mechanism from those shown in subsequent sections where the increased roughness is caused by fabricating micro/nanostructures.

2.2.3. Porosity and permeability

Avedisian and Koplik [109] found that compared with polished stainless steel, the dynamic LFP temperature on 10% porosity and 25% porosity alumina-ceramic surfaces is elevated, respectively, by about 100 K and 200 K for a methanol droplet. With a higher porosity of 40%, film boiling could not occur even when the surface temperature reaches 620 K. The same trend was also observed for n-heptane droplets with a higher Weber number [110]. Such an obvious enhancement is mainly

caused by vapor absorption into the porous structures during droplet spreading, which decreases the vapor pressure to levitate the droplet. More recently, Lipson and Chandra [111] further verified the increased dynamic LFP temperatures for n-heptane droplets on porous surfaces, where no Leidenfrost effect occurs for water droplets within the test range of surface temperatures. Similarly, Kuhn et al. [16] indicated that the dynamic LFP temperature increases with pore diameter since the vapor penetration lowers the effective vapor layer thickness.

Meanwhile, Wang et al. [3] found that the dynamic LFP temperature is significantly elevated with the existence of surface oxidization. With energy dispersive spectrometer analysis, they pointed out that the oxidized surface experiences further corrosion during the droplet impact process, where the increased surface porosity by the oxide particles results in an increased dynamic LFP temperature.

On the other hand, when conducting droplet impact experiments on porous substrates with sintered glass beads of different sizes, Kim and Lee [112] found that the dynamic LFP temperature decreases with a higher surface permeability caused by larger glass beads. This is because the pores play a role similar to nucleation cavities, and higher permeability corresponding to more nucleation sites is favorable to vapor generation. Zhao et al. [113] observed no droplet rebound phenomenon on a porous substrate, even if the surface temperature is much higher than the dynamic LFP temperature on impermeable surfaces. However, they attributed it to the significant cooling effect (which is discussed in Section 2.2.1) rather than the porous structure.

Diverging from the conventional wisdom that vapor penetrates into porous structures, Lee et al. [99] detected a negligible influence of permeability for a sintered porous surface with submicron particles. This is proved by theoretical analysis that the decrease in the normalized vapor layer thickness is insignificant within the test range of permeability. Instead, they attributed the variation of dynamic LFP temperature to the effects of thermal effusivity (for both water and ethanol) and capillary wicking (only for water).

2.2.4. *Surface structure*

Enabled by the latest development of microfabrication and nanotechnology, micro/nanoscale structures with precisely controlled geometries and dimensions can be fabricated on a smooth substrate. The existing experimental studies illustrated that surface structure modification can significantly shift the dynamic LFP temperature towards either higher or lower values.

(a) Microscale texture

As shown in Fig. 7, Wang et al. [114] utilized the selective laser melting technique to fabricate several types of microstructured surfaces. Compared to a smooth surface, the medium-density cylindrical fins, medium-density and low-density clavate fins, as well as conical fins were observed to increase the dynamic LFP temperature, while the high-density cylindrical fins exhibited lower T_{LFP} values. For the surfaces with low-density cylindrical fins and cylindrical-clavate composite fins, no dynamic Leidenfrost condition was detected under the test experimental conditions.

Tran et al. [115] found that the dynamic LFP temperature is much lower with the existence of micropillar arrays. They attributed this reduction to the increased heat transfer area caused by the microstructures. The same trend was also observed by Clavijo et al. [87], although the micropillar surface is more hydrophilic than the bare silicon. Tran et al. [115] also reported decreased dynamic LFP temperatures with increased micropillar height at fixed micropillar interspacing and width. They supposed that the droplet does not penetrate the micropillar interspacing so only a very thin vapor layer is needed to separate the droplet from the pillar top surface where the local heat transfer is much stronger than the interspacing locations. The microstructures inhibit the vapor outflow, and, therefore, a lower surface temperature is required to produce sufficient vapor pressure to levitate the droplet.

However, other studies indicated that the dynamic LFP temperature increases with micropillar interspacing [116] and micropillar width [117], while no difference was also observed between smooth and micropillar silicon [98]. Park et al. [118] concluded that the dynamic LFP temperature either increases or decreases on the micropillar surfaces, and this indeterminate variation trend is relevant to the pitch-to-width ratio and height-to-width ratio. Auliano et al. [119] verified higher dynamic LFP temperatures on the surface with tapered submicron pillars than on a plain substrate, and the increment is more remarkable at higher impact velocities. They explained it through increased hydrophilicity which enhances capillary wicking and prevents dry-out, and a higher roughness that enables a larger heat transfer area.

Later, Park and Kim [120,121] reported a nonmonotonic effect of micropillar arrays. Compared with a water droplet impacting on a smooth surface, the dynamic LFP temperatures are significantly lower on microtextured surfaces with small pillar spacings, but much higher with large pillar spacings. The case is even more complicated for ethanol

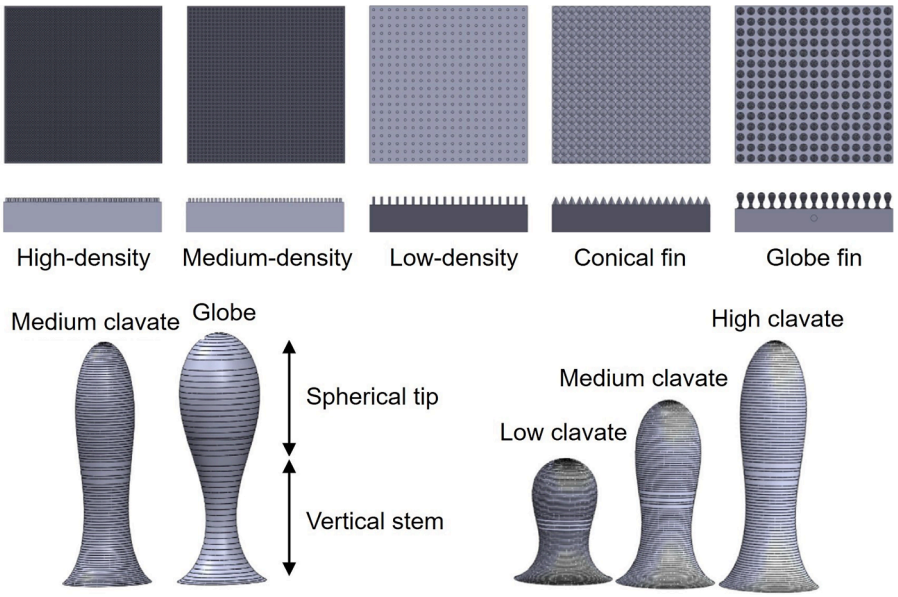

Fig. 7. Schematic of different microstructures adopted by Wang et al. [114].

droplets. For example, higher T_{LFP} occurs on the textured surfaces compared to the smooth surface at We = 3, while T_{LFP} values with small pillar spacings are lower than the smooth case at We = 5. With a further increased Weber number, all the textured surfaces show decreased dynamic LFP temperatures. Also, the effect of pillar spacing is no longer monotonic. Furthermore, the dynamic LFP temperature is also reported to exhibit different variation trends with micropillar diameter at different micropillar heights, all higher than that on a smooth surface [122]. While with a much wider range of micropillar spacing [123,124], the dynamic LFP temperature was reported to increase first and then decrease with increased pillar spacing, showing that there exists a highest T_{LFP} value at the optimal spacing.

It is interesting to note that there exist two distinct local maxima of evaporation time on micropillar surfaces from the results by Wei et al. [125], which respectively correspond to the contact nonwetting state and dynamic Leidenfrost condition. Compared to a flat surface, they found higher dynamic LFP temperatures on the micropillar surface with a strong capillary effect. They attributed the increased T_{LFP} with larger pillar spacing and pillar height to the lower effective thermal conductivity and heat transfer area with sparse micropillars and higher thermal resistance associated with taller pillars.

Jerng and Kim [126] conducted droplet impact experiments on microchannel surfaces. They found that an increased channel gap elevates the dynamic LFP temperature, which is caused by lower hydraulic resistance to the evaporating vapor flow underneath the droplet and, in turn, decreased vapor pressure. However, it was shown in Fig. 8 that the T_{LFP} values with small channel widths are lower than a smooth surface. Recently, Ogata and Nakanishi [127] found that the dynamic LFP temperature is significantly increased on microscale wire mesh surfaces, and T_{LFP} increases with decreased wire spacing. This is because the neck-like filaments formed on the meshes prevent droplet rebound, and the enhanced capillarity at small wire spacings facilitates solid-liquid contact, which ultimately elevates the dynamic LFP temperature. Cao and Chen [128] noted that the dynamic LFP temperature increases with trapezoidal microgroove width and decreases with microgroove depth, but in each case is higher than the T_{LFP} values on a smooth surface. Guo et al. [129] further indicated an obvious elevation in the dynamic LFP temperature with microgroove depth, which they attributed primarily to the microgroove-induced spreading and escaping of the generated vapor.

(a) Nanoscale texture

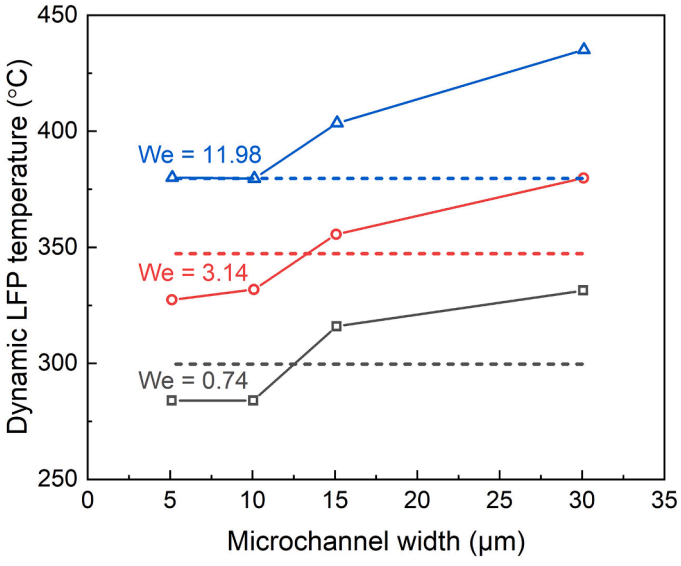

Fig. 8. Variation of dynamic LFP temperature with microchannel width [126]. Dashed lines indicate the dynamic LFP temperature for smooth surfaces.

Fig. 9 shows some scanning electron microscopy images of different nanoscale structures adopted in previous studies. Elevated dynamic LFP temperatures were reported on the nanopillar surfaces relative to the smooth substrate [130]. With the electrospun polymer nanofiber mats, Weickgenannt et al. [131] and Sinha-Ray et al. [132] observed complete adhesion instead of droplet rebound even at surface temperatures sufficiently higher than T_{LFP} on a bare substrate. This implies that the dynamic Leidenfrost effect is suppressed, i.e., the dynamic LFP temperature is prominently increased. Nair et al. [133] further proposed that the dynamic LFP temperature increases with the nanofiber length. They compared several time scales related to nanofiber cooling, nanofiber exposure to the vapor flow, and heat flow inside the nanofiber, where the time scale of nanofiber cooling is much shorter than that of the latter two. They concluded that the nanofibers are effectively cooled by the vapor flow to achieve a temperature much lower than the core substrate. This is responsible for a higher dynamic LFP temperature to sustain stable film boiling.

Similarly, Auliano et al. [35,134] experimentally detected much higher dynamic LFP temperatures on nanowire surfaces, which is due to the following four factors induced by nanowires: (1) increased surface roughness and nucleation cavity density, (2) the thermal fin effect which increases effective heat transfer area, (3) capillary wicking to prevent dry-out, and (4) better superhydrophilicity to promote intermittent liquid-solid contact. Furthermore, Sahoo et al. [135] indicated that the T_{LFP} value increases with nanowire height, which is caused by capillary wicking and also a strong vapor dispersion into the nanowire array.

Tong et al. [76] also observed no dynamic Leidenfrost phenomenon on a titanium surface covered with TiO_2 nanotubes which, however, occurs on a bare substrate within the same range of surface temperature. This indicates that the dynamic LFP temperature is significantly increased, and the dynamic Leidenfrost effect can even be completely inhibited with the nanotube structures. They attributed it to the capillary effect and improved surface wettability, while Kim et al. [36] highlighted the slip effect adjacent to the substrate, where the nanotubes enable the vapor to radially disperse so that less vapor remains to levitate the droplet. Later, the nanotube-induced increase in the dynamic LFP temperature was further confirmed [88,136], and this effect is more obvious at higher Weber numbers [88].

Lim et al. [137] showed that the dynamic Leidenfrost effect for droplet impact on a slightly inclined surface can also be successfully suppressed by coating graphene nanoplatelets. It was observed that the transition from film boiling to contact boiling occurs when a Leidenfrost droplet rolls from bare to coated sections of the aluminum substrate. They explained this phenomenon through the permeation characteristics of graphene, which enables vapor to flow through the nanostructures and hinders the formation of a continuous vapor layer.

On the other hand, some studies hold different opinions on the nanostructure effect. For example, Liu et al. [138] reported decreased dynamic LFP temperatures by fabricating nanopillar arrays. They supposed that the nanotextures enhance heat transfer and in turn decrease the required surface temperature for complete droplet rebound. Ogata and Nakanishi [127] found no difference in the dynamic LFP temperature on smooth and nanoparticle-coated surfaces. They supposed that the smooth surface is hydrophilic enough (CA = 18.5°), and that the further improved wettability by nanoparticles (CA = 5.5°) had a negligible effect.

(a) Multiscale structure

The above-reviewed studies compared the dynamic LFP temperatures on either microscale or nanoscale structured surfaces to that of smooth substrates. Meanwhile, comparisons between different scales of surface textures were also conducted. Kim et al. [37] found that the nanotube surface shows a higher dynamic LFP temperature than the microtextured surface, both surpassing the bare surface. They also attributed this enhancement to capillary wicking, the effect of which is

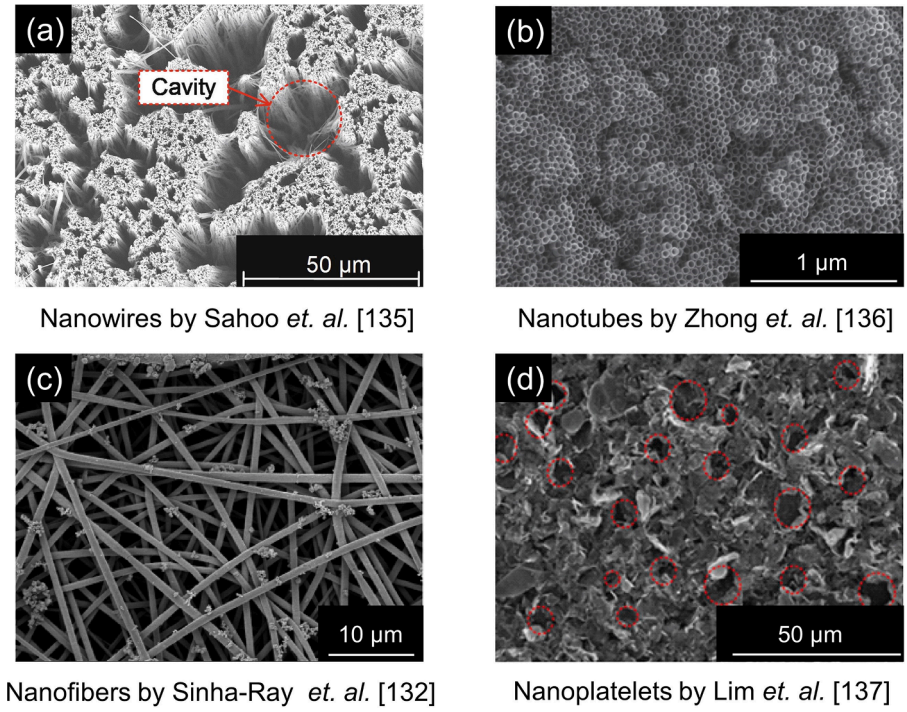

Fig. 9. Scanning electron microscopy images of different nanoscale structures.

stronger on nanotextured surfaces. Since the generated vapor is partly absorbed into the micro/nanostructures, higher evaporation rates and surface temperatures are required compared to a smooth surface. Wang et al. [29] and Farokhnia et al. [139] also verified that the nanostructures show superior improvement than microstructures.

It is shown that the microstructures facilitate intermittent liquid-solid contact, although they may induce excessive vapor generation or vapor flow blockage, while the nanoscale structures tend to promote capillary wicking. Thus, considering these factors, several researchers turned to the multiscale structures, which combine the advantages of

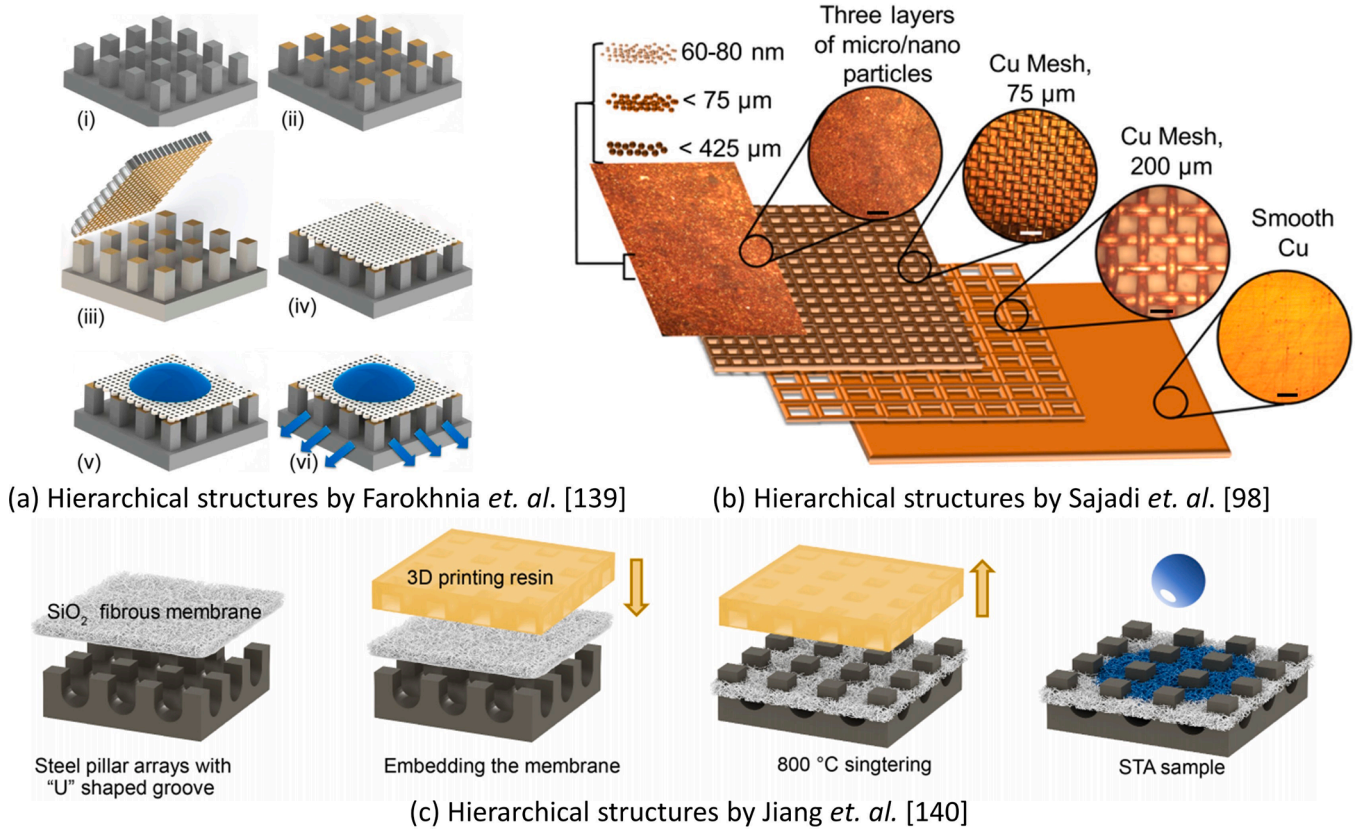

Fig. 10. Fabrication of hierarchical structures for dynamic LFP temperature enhancement.

surface textures with different length scales to achieve superior suppression of the dynamic Leidenfrost effect. For instance, Lee et al. [107] found that the dynamic LFP temperature is higher on the micro/nano multiscale textured surface (nanoneedles with micro-roughness) than on the microscale rough surface. This is due to the capillary wicking effect and the unique precursor wetting front. Ogata and Nakanishi [127] also reported that the dynamic LFP temperatures on a nanoparticle-coated microscale mesh surface increase significantly compared with the microscale mesh surface. However, no distinct difference can be detected between the micropillar-nanowire composite surfaces and the micropillar surfaces [29].

The decoupled hierarchical structures developed by Farokhnia et al. [139] and Sajadi et al. [98], as shown in Fig. 10(a) and (b), were found to effectively elevate the dynamic LFP temperature. The hierarchical structures have separate functions, e.g., the anodic aluminum oxide (AAO) nanomembrane enhances droplet-solid contact through capillary wicking, while the high-aspect ratio micropillars provide a path for vapor flow [139]. Therefore, the hierarchical structures show much better capacity than the surfaces with only microscale or nanoscale structures [98,127,139].

Jiang et al. [140] innovatively designed a new-type structured thermal armor (see Fig. 10(c)), which mainly consists of three functional units, including steel pillars as thermal bridges, a porous SiO_2 membrane for liquid wicking, and U-shaped channels for vapor evacuation. It was reported that this hierarchical structure could inhibit the dynamic Leidenfrost effect up to 1150 °C for water and even for low-boiling point nitrogen droplets. Also, the elevation is much more significant than the control tests with only membranes or channels. Recently, Du et al. [141] observed droplet impact on bare, micro/nanostructured (micron-terrace structures with a nanoneedle-like thin layer) and pillar array (with a size ranging in the hundreds of micrometers) aluminum surfaces. The greatly elevated dynamic LFP temperature on the micro/nanostructured surface is due to vapor dispersion that causes vapor pressure reduction and intermittent liquid-solid contact, while the strong capillary wicking and high vapor permeability triggered by pillars can completely suppress the dynamic Leidenfrost effect under the test conditions.

In addition to the above micro/nanoscale structures, Li and Weisensee [142] recently observed the droplet impact behavior on a single millimetric post. They found an increased static LFP temperature compared to the flat substrate due to the pinning force induced by mixed boiling modes along the post height (i.e., film boiling on the base, and contact boiling at the periphery and top surface). However, the dynamic LFP temperature shows an opposite trend over a wide range of Weber numbers, which they supposed to be caused by an increased heat transfer area. It is noted that the post with a similar dimension to the droplet plays a much different role from the previously discussed microstructures or nanostructures. Generally speaking, small-scale structures influence the dynamic LFP temperature by modulating the vapor dynamics beneath the droplet. For example, micro/nanoscale textures affect vapor flow through the structures, penetrate the vapor layer to improve solid-liquid contact, and change the surface wettability. However, large-scale textures also significantly alter the droplet morphology and impact dynamics. Overall, the mechanism of dynamic LFP temperature elevation or reduction with different scales of surface modification still needs further detailed elucidation.

2.2.5. Surface wettability

It is believed that the contact angle is an influential parameter related to the stability of the vapor layer between the liquid and the heated surface [143]. To ascertain the wettability effect on the dynamic LFP temperature, many researchers modified the chemical and/or geometric properties of plain surfaces to achieve an entire wettability spectrum from superhydrophilic to superhydrophobic. Kim et al. [144] indicated that conditions favoring bubble nucleation accompanied by unstable interface dynamics can effectively shift the dynamic LFP temperature to higher values. Therefore, more hydrophilic surfaces correspond to higher T_{LFP} values [87,145]. It was shown that the micro/nanoscale structured surfaces, which could have effectively suppressed the dynamic Leidenfrost effect, even markedly reduce the dynamic LFP temperature with hydrophobic fluoroalkylsilane coating [29,117].

Takata et al. [146,147] successfully isolated wettability as an exclusive parameter with the other surface characteristics unchanged by simply exposing the TiO_2-coated substrate to UV light (hydrophilic) or shielding it from UV light (hydrophobic), and found that the dynamic LFP temperature increases at a lower contact angle. Recently, Ma et al. [46] investigated the dynamic LFP temperature on surfaces with different wettabilities but similar roughness levels. They also found that the dynamic LFP temperature increases with better surface wettability. This is because hydrophobicity enables vapor bubbles to grow in a flat manner and to spread out, where a large bubble departure diameter is required. These two factors both contribute to the vapor layer formation and lower the surface temperature to attain the dynamic Leidenfrost condition. In a subsequent study by the same authors [148], they conducted potential barrier analysis, where better surface wettability corresponds to a greater change in the Gibbs free energy, and, in turn, film boiling is inhibited. However, the impact velocity effect was excluded in their theoretical analysis, which was dedicated to impacting droplets with low Weber numbers.

With diesel being the working fluid, Guo et al. [108] and Chen et al. [149] showed that an oleophobic surface facilitates vapor layer formation with easier bubble coalescence and a lower potential barrier for the transition to film boiling. Consequently, the dynamic LFP temperature reduces, which is similar to the case of water on hydrophobic surfaces. While on the oleophilic surfaces (which are similar to hydrophilic substrates for water), isolated bubbles are difficult to merge but it is easier to penetrate the thinner liquid lamella with better spreadability. However, Huang et al. [150] reported the opposite phenomenon. That is, the dynamic LFP temperature on a hydrophobic double-reentrant microgroove array surface is much higher than that on a hydrophilic microgroove array surface. This is because the overhanging structure on top of the microgrooves impedes the upward vapor flow. Instead, vapor escapes more easily along the microgroove direction, resulting in a decreased vapor pressure. It implies that the adverse effect of hydrophobicity can be neutralized by well-designed surface structures.

2.2.6. Surface curvature

In practical applications, some curved substrates can be involved as the impact target, such as the coating of spherical particles and the cooling of cylindrical fuel rods. Therefore, some efforts have been devoted to studying the surface curvature effect on the dynamic LFP temperature.

Jadidbonab et al. [151] reported a slightly decreased dynamic LFP temperature on a spherical surface compared to a flat substrate, and this curvature-induced shift results from additional droplet interface perturbation and gravitational force. Guo et al. [152] illustrated that the convex surface possessed a higher dynamic LFP temperature than the concave surface. This is because the tangential gravity component impedes droplet spreading in the circumferential direction on a concave substrate. The resulting thicker liquid lamella hampers bubble bursting and thus benefits vapor layer formation. Jowkar and Morad [77,78] presented the droplet impact patterns on flat, semi-cylindrical concave and convex surfaces with impact regime maps over broad ranges of surface temperatures and Weber numbers. Different from film boiling on a flat surface, they observed no thermal atomization on the concave surface, while droplet rebound and thermal atomization also diminish on the convex surface. Although not explicitly mentioned, it is speculated that the surface curvature also exerts a significant effect on the lower boundary of film boiling, i.e., the dynamic LFP temperature.

Recently, Luo et al. [82] summarized the peculiarity concerning the dynamic Leidenfrost phenomenon for droplet impact on a cylindrical surface compared with a flat surface. First, the curvature-induced

tangential velocity makes the Kelvin-Helmholtz instability more likely to occur to trigger droplet disintegration. Also, the droplet tends to spread to a greater extent in the circumferential direction, resulting in a thinner liquid lamella that is vulnerable to being penetrated by vapor bubbles. They proposed that it is easier to levitate these produced small droplets with less mass, exhibiting the dynamic Leidenfrost state.

Lee et al. [153] studied a limiting case of a cylindrical surface, i.e., droplet impact on a nichrome wire, which shows a higher dynamic LFP temperature than a flat surface. Due to the high wire curvature, the droplet-solid contact area is relatively smaller than two-dimensional surfaces. Consequently, an excessive heat transfer at a higher surface temperature is required to facilitate a jumping mode.

2.3. Effects of fluid properties

Although topographical modification of the heated substrate can elevate the dynamic LFP temperature, this method is not suitable in some applications with specified surface features (e.g., metal quenching). In these cases, adding secondary components to the base liquid is known to significantly affect droplet impact heat transfer and dynamic LFP temperature.

Compared with single-component droplet impact, the case with a binary liquid mixture is much more complicated, which additionally features the following complications. First, in addition to the temperature and pressure, the droplet thermophysical properties are also highly dependent on the component concentration, which may change dramatically during the impact process with a violent phase change. Second, due to the different saturation temperatures of each component, the more volatile component is consumed more quickly, resulting in a decreased concentration near the liquid-vapor interface. Therefore, a concentration gradient appears in the liquid phase, where transient heat transfer and mass diffusion strongly couple and compete with each other. Kompinsky et al. [75] observed a unique impact pattern for a bicomponent mixture droplet when the surface temperature lies between the dynamic LFP temperatures of n-hexane and n-decane. The droplet undergoes dry rebound first (i.e., film boiling), but then nucleation boiling occurs after the low-volatility fuel is consumed. Therefore, the dynamic LFP temperature of a mixture droplet increases with the concentration of the heavy component. The same conclusion has also been reached by other studies with diesel and dodecane [154], n-heptane/n-decane mixtures across a wide range of ambient pressures [70,155], as well as ethanol and 10% ethanol/90% n-decane mixtures [156]. Furthermore, it was proposed that the dynamic LFP temperature of binary mixtures falls within the limits of each component [157], while explosive boiling may occur at a surface temperature between the T_{LFP} values of each component with low concentrations of the more volatile component [158].

As will be discussed in the following subsections, various types of additives were adopted to alter the thermophysical properties of an impacting water droplet (e.g., surface tension, latent heat of vaporization), thereby regulating the dynamic LFP temperature. On the other hand, the subcooling degree, which is relevant to heat transfer, is another influential parameter affecting fluid properties, and therefore the dynamic LFP temperature.

2.3.1. Dissolved gas

Generally, the liquid coolant used in industries inevitably contains some dissolved non-condensable gasses from the piping system or the processing environment, which were shown to increase the liquid saturation temperature and contact angle [159,160]. Therefore, the dissolved gas may change the LFP temperature. Bernardin and Mudawar [50] reported a minimal difference between the static LFP temperatures of non-degassed and degassed sessile droplets. Cui et al. [161] found that the dissolved carbon dioxide can effectively suppress heterogeneous bubble formation for droplet impact in the film boiling regime, but the gas effect on the dynamic LFP temperature was not explicitly pointed out. Recently, Prasad et al. [84] noted that the dynamic LFP temperature increases at higher nanobubble concentrations. When the nanobubble-dispersed droplet impacts the surface, the nanobubbles at and near the liquid-solid interface are thermally destabilized and expand rapidly. The released gas forms a micrometer-scale thin layer to reduce the effective contact area between droplet and substrate, which delays the generation of a stable vapor layer. To date, the dissolved gas effect on the dynamic LFP temperature has not been fully revealed and remains an open question worthy of further study.

2.3.2. Surfactants

Several studies reported that the dynamic LFP temperature of a saline solution droplet increases with the NaCl concentration [157,162,163]. Such an elevation was regarded to be caused by droplet breakup accompanied by promoted bubble formation [161], salt crystal deposition [163], as well as increased surface tension and delayed vapor bubble coalescence [164]. It was also reported that increasing water hardness [94] and using plasma-activated water [165] can slightly increase the dynamic LFP temperature while keeping a constant contact angle. Meanwhile, a higher water content in an emulsion droplet may result in a decrease [166], an increase [167], or exhibit a negligible effect regarding the dynamic LFP temperature [13]. While the elevated dynamic LFP temperature by graphite lubricant is assumed to be related to the deposited layer and pinning of the contact line [168].

Nagai et al. [66] indicated that the dynamic LFP temperature increases at higher lubricant concentrations (i.e., lower surface tension), and the increment is more obvious within the low concentration range. Mach et al. [169] proposed that the surfactant can reduce the droplet evaporation rate and enhance the molecular attractive force between the droplet and solid surface, both beneficial to elevate the dynamic LFP temperature. On the other hand, the droplet spreads to a larger lamella with reduced surface tension, and the vapor pressure increases. Therefore, a lower dynamic LFP temperature is needed to levitate the more deformed droplet. The combined effect of these three factors leads to the trend that the dynamic LFP temperature is independent of the surfactant below a threshold concentration, after which T_{LFP} sharply decreases and remains unchanged with further increased surfactant concentrations. This abrupt reduction implies that the dominant effect is the decreased surface tension, which accords with the fact that a certain surfactant content is necessary to achieve complete monolayer surface coverage, and higher surfactant concentrations no longer have any effects. However, also considering the limited effect within a certain concentration range, Zabala et al. [94] showed that the dynamic LFP temperature steeply increases first, then remains stabilized and finally decreases with increased lubricant concentrations. They ascribed the initial elevation to the requirement of higher surface temperatures to produce the critical evaporation rate for droplet levitation. While the stabilization of the dynamic LFP temperature is due to the droplet surface being saturated with the lubricant, any further addition of lubricant is deemed ineffective.

Qiao and Chandra [170] reported an inhibiting effect of an anionic surfactant (sodium dodecyl sulfate, SDS) on the dynamic LFP temperature of water droplets. They suggested that heterogeneous nucleation is suppressed along with the surfactant-induced decrease in the contact angle. Therefore, the droplet evaporation rate increases in the transition boiling regime, and the maximum evaporation time shifts to a lower surface temperature. Zhang et al. [171] also found that the dynamic LFP temperature significantly decreases with the concentrations of SDS and cationic cetyltrimethylammonium bromide (CTAB) before the critical micelle concentration (CMC) is reached. They attributed this change to the nonpolar chains of the absorbed surfactant monomers that support bubble growth and coalescence. Although the same additives as those by Qiao and Chandra [170] and Zhang et al. [171] were adopted, Prasad et al. [81] found that the dynamic LFP temperature increases with SDS and CTAB concentrations as a whole, accompanied by surfactant-induced inhibition of droplet spreading, while the increment

is more prominent for the former additive. They ascribed this contradiction to different surface conditions and droplet diameters. Also using SDS, Cai et al. [172] reported that the dynamic LFP temperature increases first and then decreases with surfactant concentration. The same trend was also observed for other additives, including dodecyl trimethylammonium bromide (DTAB), Pluronic F127, Pluronic P123, and Tween-20. They proposed a possible reason that the enhancements of wetting capacity and boiling heat transfer capacity are not synchronized with the change of surfactant concentration. The abovementioned disagreement between various studies using the same types of surfactants may also stem from diverse experimental conditions, as shown in Table 2.

Bertola and Sefiane [34,173] found that the dynamic LFP temperatures with polyethylene oxide are much lower than pure water droplets. It was postulated that the polymer solution with elongational viscosity increases stability at the droplet surface, reduces the possibility of liquid-solid contact, and prevents bubble bursting for atomization. However, Li et al. [174] observed an opposite trend with the same polymer additive. Meanwhile, Dhar et al. [80] detected a nonmonotonic effect of polyacrylamide, where the dynamic LFP temperature first markedly increases and then decreases with additive concentration, and finally even becomes lower than pure water droplets. The enhancement is due to the viscoelasticity-induced filament formation during droplet retraction, which prevents the droplet from fully rebounding. However, droplet viscosity appreciably increases with high polymer contents, which reduces the shear rate and deteriorates the strengthening effect.

2.3.3. Alcohol additives

Alcohol additives are also widely adopted in heat transfer studies to avoid the potential sedimentary thermal resistance and corrosion caused by nanoparticles and soluble salts. Chen et al. [47] found that the addition of a small amount of 1-octanol or 2-ethyl-hexanol to water droplets could observably increase the dynamic LFP temperature at the same impact velocity, and the increase is more obvious at higher alcohol concentrations. They attributed this phenomenon to the joint effect of bubble bursting and bubble coalescence. The lower surface tension caused by the alcohol additive induces better droplet spreadability, and the accompanied thinner liquid lamella is more conducive to vapor bubble bursting. On the other hand, lower surface tension decreases the bubble departure diameter, which impedes both bubble coalescence and the formation of a continuous vapor layer. Recently, Cai et al. [48] observed a more significant elevation using low-carbon alcohol additives at low concentrations. That is, the lowest dynamic LFP temperature of the bi-component droplet at an impact velocity of ~0.44 m/s still surpasses the highest value of the water droplet at an impact velocity of ~1.32 m/s. This indicates that a small amount of low-carbon alcohol additives can effectively compensate for the negative influence of inferior impact momentum.

Zhang et al. [171] pointed out the different effects of polyethylene glycol (PEG-100) and octylphenoxypolyethoxyethanol (Triton X-100). The former additive increases the dynamic LFP temperature with negligible concentration effect, while T_{LFP} decreases sharply and then increases with Triton X-100 concentration. On the other hand, an inhibited dynamic Leidenfrost effect was reported in other investigations when a high content of ethanol was added to an impacting water droplet. For instance, Kudra et al. [157], Sen et al. [158] and Zhong et al. [136] all found that the dynamic LFP temperature decreases with alcohol concentration. They supposed that the decrease may be relevant to the observed unique phenomena during droplet impact, such as the hemi-wicking liquid evaporation involving the central jet [136] and explosive disintegration involving the preferential evaporation of the more volatile ethanol [158].

The experimental conditions of the above studies are tabulated in Table 3. Apart from alcohol type, solid material, and surface finish, it is speculated by the present authors that the alcohol concentration is mainly responsible for the abovementioned contradictions. With a high ethanol content, the markedly reduced contact angle results in a larger liquid lamella for heat transfer. Also, recall that the latent heat of vaporization of ethanol is much lower than that of water. Therefore, the vapor generation is dramatically improved compared to the cases of dilute alcoholic solution and pure water. Accordingly, a lower surface temperature is required for the dynamic Leidenfrost threshold. However, when the alcohol concentration is low, the decreased surface tension plays a predominant role, as stated by Chen et al. [47].

It is also noteworthy that considering the concentration-related enhancement or deterioration, there probably exists an optimal alcohol concentration to achieve the highest dynamic LFP temperature since a water droplet possesses a much higher T_{LFP} value than an alcohol droplet ceteris paribus. Further research is needed to ascertain the alcohol additive effect over a wide range with small enough intervals of concentration.

2.3.4. Nanoparticles

Nanofluid with nanoparticles uniformly dispersing in the conventional base fluid has attracted considerable attention in the heat transfer community. However, no consensus has been reached on its effect on the

Table 2
Experimental conditions for prior studies centered on surfactant effects on the dynamic LFP temperature.

Reference	Additive concentration	Surface material	Test condition
Dynamic LFP temperature decreasing with increasing surfactant concentration			
Qiao and Chandra [170]	100–1000 ppm SDS	polished stainless steel	H_0 = 50 mm
Zhang et al. [171]	1/9–10/9 CMC* SDS or CTAB	hydrophilic and hydrophobic silicon	We ~ 1
Dynamic LFP temperature increasing with increasing surfactant concentration			
Prasad et al. [81]	1/8–1 CMC SDS or CTAB	stainless steel	We = 9.2–49.8
Dynamic LFP temperature non-monotonically changing with surfactant concentration			
Cai et al. [172]	0.002–0.05 wt.% SDS	stainless steel	H_0 = 300 mm

* CMC = 9×10^{-3} mol/L and CMC = 9×10^{-4} mol/L respectively for SDS and CTAB [171].

Table 3
Experimental conditions for prior studies centered on alcohol effects on the dynamic LFP temperature.

Reference	Additive type	Surface material	Weber number
Dynamic LFP temperature decreasing with increasing alcohol concentration			
Kudra et al. [157]	20–75 wt.% ethanol	polished stainless steel	We < 80
Sen et al. [158]	12.5–91.5 vol.% ethanol	polished aluminum	We = 20–50
Zhong et al. [136]	25–90 vol.% ethanol	titanium with TiO_2 nanotubes	We = 9–13
Dynamic LFP temperature increasing with increasing alcohol concentration			
Chen et al. [47]	0.02–0.1 wt.% 1-octanol or 2-ethyl-hexanol	sanded copper	We = 8–50
Dynamic LFP temperature non-monotonically changing with alcohol concentration			
Zhang et al. [171]	1/9–10/9 CMC* Triton X-100	hydrophilic and hydrophobic silicon	We ~ 1
Dynamic LFP temperature independent of alcohol concentration			
Zhang et al. [171]	1/9–10/9 CMC PEG-1000	hydrophilic and hydrophobic silicon	We ~ 1
Cai et al. [48]	2–8 vol.% ethanol or isopropanol, 1–7 vol.% n-butanol, 0.5–2.5 vol.% n-pentanol	polished red copper	We < 80

* CMC = 3.0×10^{-4} mol/L and CMC = 1.5×10^{-2} mol/L respectively for Triton X-100 and PEG-100 [171].

static LFP temperature of sessile droplets among a limited number of studies. Paul et al. [175] observed an evident increase in the static LFP temperature for droplets with abundantly dispersed nanoparticles, compared to pure water and sparsely dispersed nanofluid droplets. Through topography analysis of the heated surface, they argued that this concentration-related enhancement is owed to the existence of a nanometric porous structure caused by nanoparticle deposition. The resultant capillary pressure overwhelms vapor pressure, requiring a higher surface temperature to trigger the Leidenfrost phenomenon. In a recent experimental study by Ulahannan et al. [176], however, much lower static LFP temperatures for different types of nanofluid droplets were observed when compared to pure water. They proposed that the high-conductivity nanoparticles enhance heat transfer and accelerate vapor layer formation, which contributes to droplet levitation.

As for an impacting droplet, Prasad et al. [83] found that the dynamic LFP temperature significantly increases with the Al_2O_3 nanoparticle concentration. This is because the nanoparticulate residue deposition during the spreading and retraction stages alters the surface roughness, and provides additional bubble nucleation sites. The residue strongly influences the bubble departure diameter, and prevents bubble coalescence and vapor layer formation. Therefore, a higher surface temperature is needed to trigger the dynamic Leidenfrost condition.

2.3.5. Subcooling degree

As for the influence of the droplet subcooling degree, there are also varied opinions. The experimental measurements by Nagai et al. [66] indicated that the dynamic LFP temperature increases initially and decreases afterward with the subcooling degree. This is because a lower surface tension and better wettability are achieved with a lower subcooling degree (i.e., a higher droplet temperature), resulting in a higher T_{LFP} value. Meanwhile, the correspondingly increased liquid-solid contact temperature shows a weakening effect on the dynamic LFP temperature. Therefore, the joint result is that the dynamic LFP temperature reaches a peak at a certain subcooling degree.

On the other hand, Kudra et al. [157], and Park and Kim [60] reported a consistent elevation by droplet subcooling. It is expected that as the subcooling degree increases, more energy is used for droplet heating rather than for phase change. Consequently, a higher surface temperature is needed to generate more vapor to reach the critical dynamic Leidenfrost condition. This disagreement with Nagai et al. [66] may stem from dissimilarities in the operating conditions since the dynamic LFP temperature is affected by multiple parameters.

2.4. Effects of external conditions

Apart from impact conditions, surface features, and fluid properties, it is expected that the external environment also potentially affects both the thermodynamic and hydrodynamic behaviors of an impacting droplet. Accordingly, the dynamic LFP temperature also appreciably varies. The parametric studies of external conditions are discussed in this section.

2.4.1. Ambient pressure

Previous experiments on a sessile droplet showed that much lower static LFP temperatures can be achieved at reduced pressures [177,178]. As for an impacting droplet, it was observed that the dynamic Leidenfrost effect becomes less important as the ambient pressure increases [179], and the dynamic LFP temperature increases at higher ambient pressures [151]. As shown in Fig. 11, Buchmüller [180] mapped the water droplet impact patterns on a pressure-temperature diagram to demarcate different heat transfer regimes. Higher dynamic LFP temperatures are detected at elevated ambient pressures, which are always lower than the liquid-solid contact temperature at a surface temperature equal to the liquid critical temperature. Furthermore, it is interesting to note that $\Delta T_{LFP} = T_{LFP} - T_{sat}$ seems to remain unchanged within the test range. Recently, Chausalkar et al. [155,181] also reported increased dynamic LFP temperatures but distinctly decreased ΔT_{LFP} values within the super-atmospheric pressure range. They indicated that the fuel droplet dynamic LFP temperature is consistently bounded by the superheat limit temperature and saturation temperature.

Testa and Nicotra [182] indicated that the dynamic LFP temperature increases with increased subatmospheric pressure accompanied by slightly higher ΔT_{LFP} values. Yu et al. [183] also reported a monotonically elevated dynamic LFP temperature when the ambient pressure ranges from 6 kPa to 20 kPa. However, it is inferred from the impact regime map that the dynamic LFP temperature decreases with ambient pressure below 6 kPa. This is because they detected a unique explosive rebound behavior at extremely low ambient pressures (0.26 kPa), which is caused by the dramatic formation and explosion of vapor bubbles. Elsewhere, Limbeek et al. [184] experimentally found that the dynamic LFP temperatures remained nearly constant at the ambient pressures ranging from 13 kPa to 54 kPa, all slightly below the value at atmospheric pressure. They supposed that more vigorous vapor generation (i.e., a higher surface temperature) is required to levitate the droplet due to the compressible gas at reduced pressures. Meanwhile, the droplet spreads to a greater extent when decreasing the ambient pressure, which in turn enhances vapor production and partially counteracts the gas-compressibility effect. Therefore, the dynamic LFP temperature

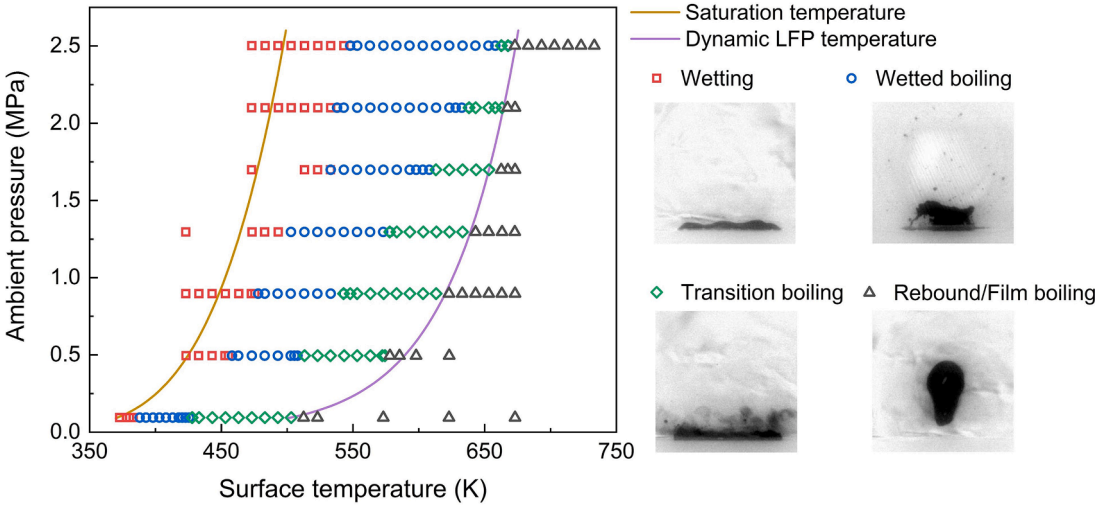

Fig. 11. Impact regime map of water droplet (We = 5) on polished aluminum. Adapted from Buchmüller [180].

subject to the coupling effect of these two mechanisms shows neglible change.

It is indicated from the above studies that a higher ambient pressure generally elevates the dynamic LFP temperature at either subatmospheric or super-atmospheric pressure ranges. However, to what extent the dynamic LFP temperature is increased and its deviation from the saturation point still requires further research.

2.4.2. Gravitational acceleration

Maquet et al. [185] pointed out a slight but consistent increase in the static LFP temperature for sessile droplets with an increased acceleration of gravity. Qiao and Chandra [186,187] conducted droplet impact experiments under low gravity conditions. They found it difficult to find a local maximum evaporation time (corresponding to the dynamic LFP temperature) while droplet film boiling was not observed. The droplet was pushed away from the surface upon impact since the vapor pressure can no longer be balanced by the droplet weight in low gravity. Instead, they turned to droplet impact photographs and surface temperature measurements, and found that the dynamic LFP temperature of n-heptane droplets equals the gravity-independent thermodynamic superheat limit. However, they proposed that the dynamic LFP temperature of water droplets is irrelevant to any change in droplet impact dynamics or heat transfer, and cannot be determined in low gravity.

2.4.3. Other active techniques

Ng et al. [188] proposed a new technique to effectively suppress the dynamic Leidenfrost effect by exerting low-frequency vibrations on the heated surface. They found that film boiling of an impacting droplet on a stationary surface (Fig. 12(a)) gradually transforms into gentle film boiling (Fig. 12(b)), contact boiling with ejection of tiny droplets (Fig. 12(c)), and contact boiling with the disintegration of spreading lamella (Fig. 12(d)) when increasing the surface acceleration, indicating a higher dynamic LFP temperature. This is because a stronger vibration results in a higher value of impact force, which facilities droplet-solid contact and increases the critical temperature for droplet levitation.

Great attention has also been given to the effective suppression of the static Leidenfrost effect for sessile droplets by generating AC/DC electric fields [189–191] or high-frequency acoustic waves [192], which respectively induce an extra electrostatic force and acoustic radiation pressure to propel the liquid-vapor interface towards the heated surface. Nevertheless, there is a gap in the literature concerning the electrostatic and acoustic effects on the dynamic LFP temperature. As for the impact case, Deng and Gomez [97], as well as Xu et al. [193], found that the external electric field can suppress or delay droplet rebound in the film boiling regime, which shows the potential to increase the dynamic LFP temperature, and it may motivate future investigations on this issue.

2.5. Experimental correlations

In view of the extensive industrial applications of droplet impact on high-temperature surfaces, accurate prediction of the dynamic LFP temperature is crucial to equipment safety and reliability. Table 4 summarizes the empirical correlations of dynamic LFP temperature provided in the literature, which involve various experimental conditions.

These correlations are convenient for practical application due to their simplicity and ease of calculation. Although these correlations provide satisfactory predictions of dynamic LFP temperature under certain conditions, their validity is limited only to the ranges of parameters specific to each correlation. The predictions by various empirical correlations developed for water droplets are compared in Fig. 13. Obvious distinctions can be observed between different correlations. Additionally, most correlations ignore the influences of several parameters, especially ones associated with surface conditions. Also, the dynamic LFP temperature should converge to the static LFP temperature of sessile droplets when the Weber number approaches zero, while some expressions do not satisfy this condition. This issue clearly points to the need for correlations with more factors considered and wider applicability.

2.6. Discussion

It is seen from the above sections that contradictions between various studies concerning the effect of certain factors still remain unresolved. First and foremost, despite diverse ranges of experimental conditions, the inconsistency between different investigations may also originate from the uncertainties in experimentally identifying the dynamic LFP temperature. As mentioned in Section 1.2, there has been no universal standard to determine the dynamic Leidenfrost transition. It can be considered as the maximum evaporation time temperature, the lowest temperature for droplet rebound/breakup without atomization (also taken as the onset of rebound in some studies), or the lowest temperature to form a continuous vapor layer, which are, respectively, referred to as *thermodynamic, hydrodynamic*, and *optical* dynamic LFP temperatures in this section for the convenience of discussion. It is so far still doubtful whether the dynamic LFP temperatures obtained with three different approaches are equivalent under the same working conditions.

It is indicated by Liu and Craig [195], as well as Kim et al. [36,37,107,145] that the thermodynamic dynamic LFP temperature greatly deviates from the hydrodynamic value. A relatively large bias was also observed when determining the thermodynamic value with the aid of measurements of surface temperature evolution [69]. However, Kim and Kang [144] found that measured thermodynamic and hydrodynamic dynamic LFP temperatures coincided with each other. On the other hand, Khavari and Tran [33] showed that there exist some discrepancies, although not significant, between the hydrodynamic and optical dynamic LFP temperatures.

Appreciably, it is intractable to accurately measure the evaporation time of an impacting droplet, especially for those with high impact velocities and near the critical dynamic Leidenfrost condition. The impacting droplet may rebound, disintegrate, atomize, and even behave much more intricately, which brings great uncertainty to judging the end time of complete evaporation. As for the hydrodynamic criterion, which is mainly based on the analysis of side-view high-speed images, whether the atomized tiny droplets can be detected depends on several factors, such as the illumination conditions, camera exposure time, sensitivity, and spatial resolution [45]. Also, it was proposed that the hydrodynamic impact phenomenon cannot always be unequivocally associated with heat transfer classification [71,196] since the time scale

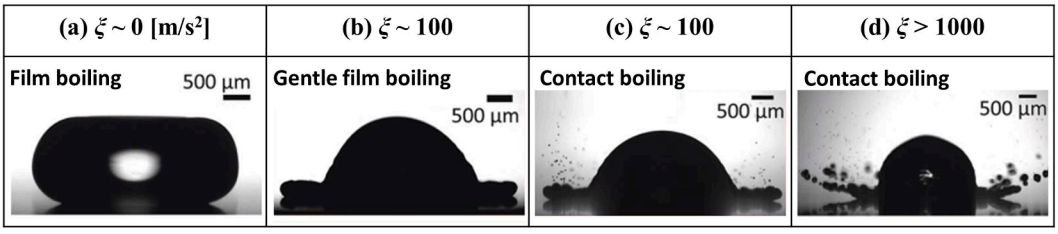

Fig. 12. Water droplet patterns after impact on a vibrating substrate with different accelerations. All the surface temperatures are equal to T_{LFP} on a stationary surface. Adapted from Ng et al. [188].

Table 4
Experimental correlations of dynamic LFP temperature.

Reference	Correlation	Liquid type	Surface material	Test range
Bertola and Sefiane [34]	$T_{LFP} = 164.72 + 29.79We^{0.38}$ $T_{LFP} = 157.62 + 2.11We^{0.54}$	water water + polymer	polished aluminum	We = 20–100
Chen et al. [47]	$T_{LFP} = (13We^{0.5} + 22)Oh^{-0.2} + 48$	water, water + 1-octanol, water + 2-ethyl-hexanol	red copper	We = 8–50
Prasad et al. [81]	$T_{LFP} = (365Oh^{0.594} + 128)We^{-0.15} + 142$	water, water + SDS, water + CTAB	smooth stainless steel	We = 9.2–49.8
Prasad et al. [83]	$T_{LFP} = (407.5We^{-0.125} + 13{,}600)Oh^{0.6}$	water, water + Al_2O_3 nanoparticles	smooth stainless steel	We = 10–168
Prasad et al. [84]	$T_{LFP} = (16.5Oh^{-0.45} + 160)We^{-0.15} + 18$	water, water + oxygen nanobubbles	smooth stainless steel	We = 11–28
Wu et al. [44]	$T_{LFP} = 141.02 + 5.44u^{0.5}$ $T_{LFP} = 141.01 + 5.47u^{0.5}$ $T_{LFP} = 153.02 + 6.76u^{0.5}$ $T_{LFP} = 359.79 + 80.49u^{0.5}$ $T_{LFP} = 279.78 + 144.78u^{0.5}$ $T_{LFP} = 136.63 + 193.06u^{0.5}$ $T_{LFP} = 100.51 + 212.43u^{0.5}$ $T_{LFP} = 251.1 + 28.82u^{0.5}$ $T_{LFP} = 70.41 + 105.38u^{0.5}$ $T_{LFP} = 164.29 + 36.13u^{0.5}$ $T_{LFP} = 117.31 + 55.95u^{0.5}$ $T_{LFP} = 49.76 + 89.96u^{0.5}$	ethanol ethanol water water water ethanol ethanol FC-84 FC-72	polished aluminum polished brass polished Armco iron sapphire sapphire polished aluminum polished aluminum glass sapphire sapphire sapphire	We = 51–1030 We = 51–1030 We = 51–1030 We = 5–383 [102] We = 1.3–28 [60] We = 7–160 [45] We = 20–100 [34] We = 16–1480 [103] We = 1.3–38 [60] u = 0.4–4.3 m/s, d = 2.8 mm [41] u = 0.4–3.85 m/s, d = 1.8 mm [41] We = 4.2–82 [60]
Yao and Cai [32]	$T_{LFP} = T_{sat} + 135.6We^{0.09}$	water	oxidized brass	We = 22–62
Luo et al. [82]	$T_{LFP} = 464.52 + 2855.68We^{-1.07}$*	water	stainless steel	We = 26–107
Issa [194]	$T_{LFP} = T_{LFP}\|_{1\ atm} + 7.024 + 195\log_{10}P$**	water	molybdenum	H_0 = 10–20 mm, d = 2 mm [182]
Guo et al. [129]	$T_{LFP} = 185.4 + 8.7R_a - 0.41R_a^2 + 1.06We - 0.115We^2$	cutting fluid solution	smooth/ microgrooved cemented carbide	We = 3.7–59.2

* Droplet impact on a cylindrical surface.
** Ambient pressure is expressed in atm.

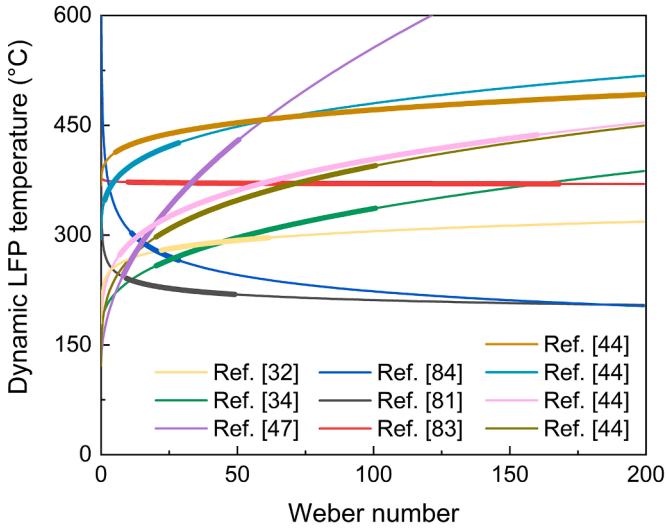

Fig. 13. Dynamic LFP temperatures for water droplets predicted according to different prior correlations. A droplet diameter of 2 mm is used to calculate the Ohnesorge number. The bolded portions of the predictions correspond to the Weber number range of the respective correlation.

for the dynamic Leidenfrost effect is much longer than the hydrodynamic transient droplet impact [72]. For instance, in the spray film boiling regime shown in Fig. 14(a), numerous atomized droplets were still observed at surface temperatures much higher than the dynamic LFP temperature [49]. Meanwhile, atomization can be absent at low superheat degrees for low-We droplet impact on superhydrophobic and hydrophobic surfaces [87], while tiny-scaled direct droplet-solid contact is still considered to occur for droplet rebound without atomization [197]. With the aid of high-speed X-ray imaging and total internal reflection imaging, Lee et al. [42] indicated that droplets can rebound even without the formation of a complete vapor layer (see Fig. 14(b)). That is, purely photographic techniques may be not sufficient to determine the non-wetting conditions [198]. Therefore, Lee et al. [107] proposed that the dynamic LFP temperature is characterized by two key features: the rebound phenomenon and the formation of a stable vapor layer.

Kwon et al. [58] observed a momentary contact phenomenon on aluminum alloy with excellent heat transport properties, i.e., the vapor layer recovered from temporary collapse in a few microseconds. Since the droplet experiences the transition from contact boiling to film boiling, they deemed this surface temperature condition as transition boiling. They indicated that detecting this momentary contact requires various observation angles and a high-spatiotemporal-resolution imaging system, especially for opaque metallic surfaces, which is insufficiently studied in many experiments and will cause a difference in the measured dynamic LFP temperature. It is also noteworthy that in most studies, the reported dynamic LFP temperature is the measured temperature by thermocouples embedded several millimeters directly below the impact point. This temperature, however, can be quite different from the surface temperature when the impact substrate is placed on a heating block. Bertola et al. [45] pointed out that the effects of contact thermal resistance, free convection, and radiative heat transfer cannot be neglected when adopting the experimental setup in ref. [49]. Therefore, direct measurement of surface temperature is suggested, particularly for nano-scaled and hierarchically structured surfaces to avoid underestimating the dynamic LFP temperature [35].

Considering the aforementioned uncertainties, it was suggested that the dynamic LFP temperature lies within a certain range rather than being a constant value [31,41,199], where the lower threshold, T_{LFP}^{-}, is controlled by hydrodynamic instability or surface roughness [199]. Chantelot and Lohse [199] analogized the dynamic Leidenfrost effect

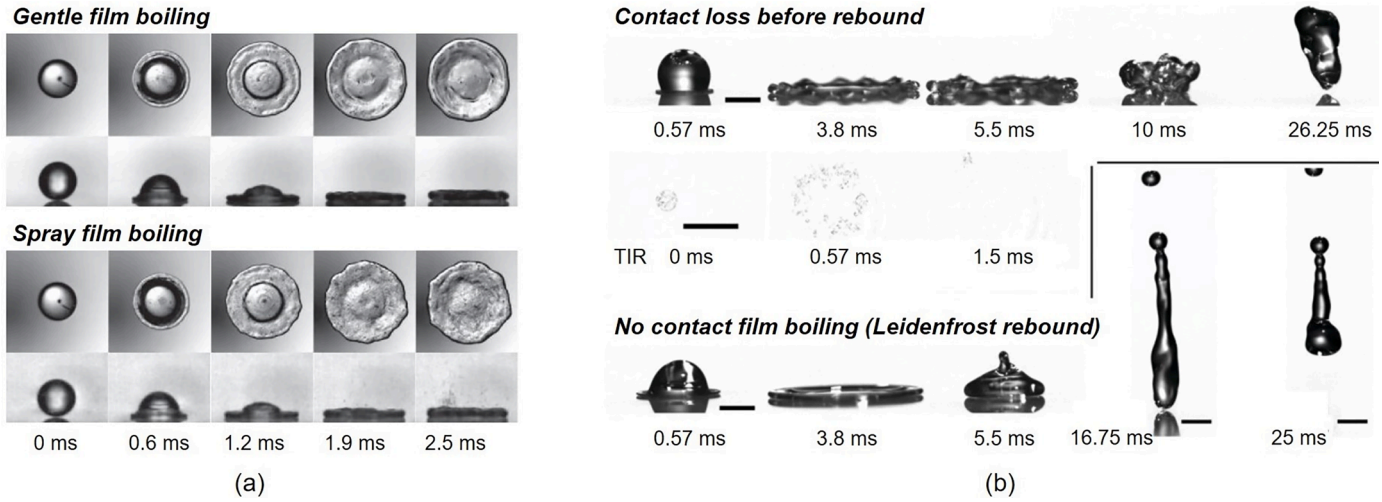

Fig. 14. Droplet impact patterns. (a) Water droplet (We = 32) impact on polished silicon at T_w = 500 °C (gentle film boiling with no atomization) and T_w = 580 °C (spray film boiling with atomization) [49]. The measured dynamic LFP temperature is ~425 °C. (b) Ethanol droplet (We = 71.6) impact on sapphire at T_w = 204 °C (rebound with droplet-solid contact) and T_w = 323 °C (rebound without droplet-solid contact) [42]. The measured dynamic LFP temperature is ~320 °C.

incipience to a nonequilibrium-directed percolation phase transition, and proposed that the upper threshold, $T^{+}_{LFP,}$ corresponds to the balance between the spreading and receding of wet regions. They emphasized that this definition expresses the resilience of Leidenfrost droplets to contact when $T_w > T^{+}_{LFP}$ rather than hydrodynamic droplet levitation by the vapor layer. In a study by the same authors [200], they further proposed multiple mechanisms that trigger the gas (air and vapor) layer collapse during different time scales associated with droplet impact, including short-time contact, late-time contact, and contact caused by evaporation-induced vertical oscillations of the gas layer. Droplet evaporation and gas drainage are both responsible for the transition toward the dynamic Leidenfrost effect. Furthermore, due to the fact that the transient stability of the gas layer facilitates droplet rebound, the dynamic LFP temperature in the low-velocity range can be lower than that the static LFP temperature.

In addition, it is seen that previous studies qualitatively interpreted the contrary effect of certain parameters from a similar perspective. For example, researchers attributed both increased and decreased dynamic LFP temperature to better spreading characteristics. As shown in Fig. 15, whatever the cause of the improved extent of spreading (e.g., by higher impact velocity, reduced surface tension, modified surface structure, etc.), the resultant larger and thinner liquid lamella is beneficial to enhance heat transfer and bubble nucleation. In this case, there are two different outcomes according to the literature. One is the vapor bubble bursting where the liquid lamella is penetrated by the generated bubbles, which requires a higher dynamic LFP temperature to prevent droplet-solid contact. The other is faster vapor layer formation to achieve easier droplet levitation, and, in turn, to lower the dynamic LFP temperature. Then, the following questions arise: (a) When changing a certain parameter to improve droplet spreading with all other factors being fixed, will the dynamic LFP temperature decrease or increase, and to what extent? (b) Which parameters are predominantly responsible for this outcome? To deal with these issues, future experiments are indispensable to account for the influence of various parameters under wide and highly controlled conditions.

Another important issue concerns the influence of surface characteristics. Both increased and decreased dynamic LFP temperatures have been reported for the topographically patterned surfaces with either regular or irregular textures. This originated from the fact that surface modification simultaneously changes various surface characteristics [99], such as thermophysical properties [52], surface roughness, wettability, permeability and porosity, etc. Additionally, the inevitable formation and thickening of the oxidation layer accompanied by

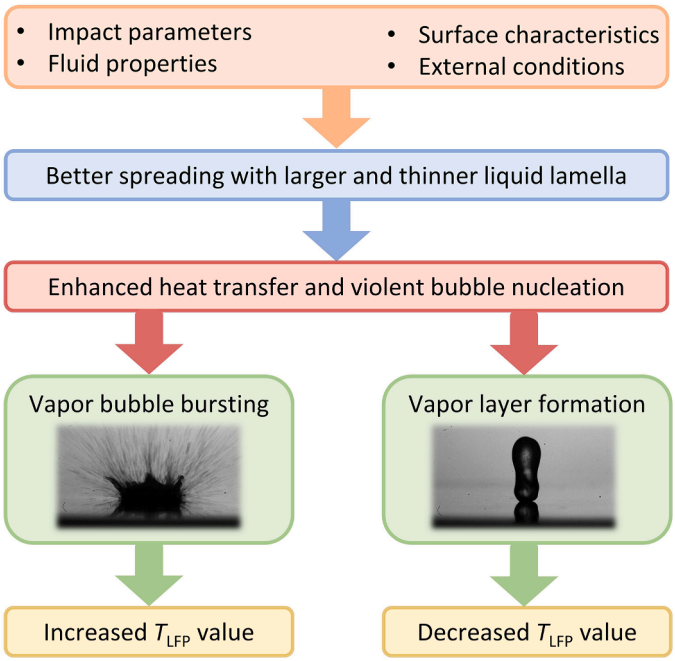

Fig. 15. Different outcomes accompanied by enhanced spreading ability.

continuous heating during experiments with some metallic materials also change their surface characteristics. The best solution is to decouple the effects of different surface features to reveal their respective effect. For instance, Lee et al. [99] found that the difference in the capillary wicking rates is negligible for ethanol droplets on surfaces with different porosities. Thus, they were able to eliminate the capillary wicking effect from analysis, and solely consider the influence of solid thermophysical properties. Kim et al. [201] separated the effects of different surface characteristics on the static LFP temperature. Specifically, the silicon surface fabricated with large-spacing micropillars, which excludes capillary wicking with no change in wettability, was used to study the surface roughness effect. The nano-smooth gold layer (CA = 83°) and silicon oxidation layer (CA = 19°) were compared to ascertain the wettability effect, while the silicon oxide nanoparticle layer with a negligible change in roughness was aimed at the nanoporosity effect. However, the accurate measurement of some surface features on

irregularly shaped structured surfaces is quite difficult. Consequently, the extension of this method to broader ranges of operating conditions warrants further in-depth studies to clarify the underlying physics.

3. Theoretical modeling of dynamic LFP temperature

Despite the extensive experimental investigations on the dynamic LFP temperature, the underlying mechanism is still far from fully theoretically understood because of its inherent complexity. There is no generally accepted theoretical model for dynamic LFP temperature prediction with satisfactory accuracy at present. The existing models can be classified according to their rationales as those based on bubble nucleation theory, the transient heat conduction equation, the vapor-gas layer analogy, and the pressure balance criterion, which will all be discussed.

3.1. Bubble nucleation theory

The dynamic Leidenfrost phenomenon is caused by rapid and intensive bubble generation to form a continuous vapor layer once a droplet impacts a high-temperature surface. Therefore, it can be hypothesized that the dynamic LFP temperature is related to bubble dynamics.

Taking vapor bubble nucleation, growth, and merging behaviors on a heated surface into consideration, Bernardin and Mudawar [202] postulated that when the liquid-solid interface temperature reaches the static LFP temperature, sufficient surface cavities will be activated to generate a high enough bubble growth rate, which enables the almost instantaneous formation of a continuous vapor layer upon liquid-solid contact. Based on this triggering mechanism, they developed a mechanistic model to predict the static LFP temperature of a sessile droplet, into which the surface cavity size distribution was integrated.

Later, the above sessile droplet model was further extended to the case of an impacting droplet [203], where the impact-induced increase in the interfacial pressure was considered to modify the fluid properties at the liquid-solid interface. They adopted the 20% elastic impact pressure relation [204,205] to calculate the interfacial pressure increase during droplet impact, and the calculated dynamic LFP temperatures of impacting water droplets on a polished aluminum surface were correlated as

$$T_{\mathrm{LFP}} = 162 + 24.3u^{0.64} \tag{6}$$

As shown in Fig. 16, the predicted dynamic LFP temperatures using Eq. (6) agree quite well with experimental data for both water droplet streams and sprays on different polished metal surfaces. The authors revealed that for substrates with surface roughness parameters orders of magnitude higher than the nucleation cavities (0.1–1.0 μm), this model is also capable of providing an upper limit of dynamic LFP temperature, which is also validated against data on various particle-blasted surfaces in Fig. 16.

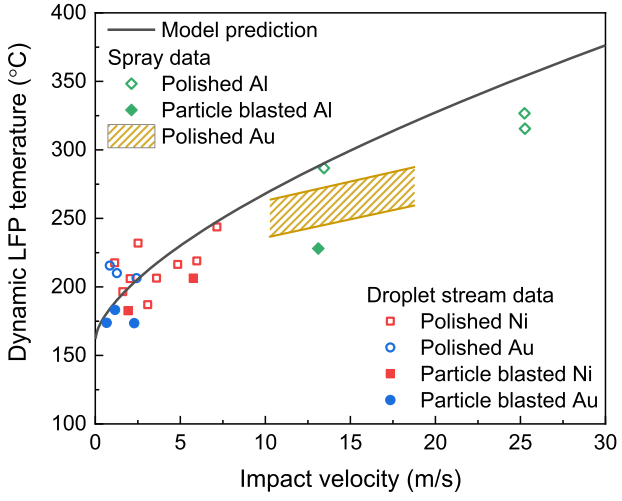

Fig. 16. Comparison of predicted and measured dynamic LFP temperatures for water droplets impacting smooth and rough surfaces. Adapted from Bernardin and Mudawar [203].

Despite some uncertainties in the surface cavity size distribution, cavity cancelation parameter, and effect of droplet velocity and surface roughness on the impact pressure, the model by Bernardin and Mudawar [203] is the first one that integrates the surface roughness effect to theoretically predict the dynamic LFP temperature, and successfully captures the impact velocity dependence with high accuracy. Also, it should be noted that since this model is constructed based on the cavity activation and bubble growth criterion, the dynamic Leidenfrost condition is approached from the transition boiling regime, which is different from the other models dedicated to a Leidenfrost droplet reviewed in the subsequent sections.

3.2. Transient heat conduction

From the perspective of heat transfer, heat is delivered from the hot surface to the impacting droplet, resulting in the formation of a vapor layer. The surface temperature first decreases to a minimum and then returns to the initial value. Considering the one-dimensional transient heat conduction process in a semi-infinite substrate, the surface temperature during droplet impact can be expressed as

$$\frac{T_w(t) - T_{sat}}{T_{w0} - T_{sat}} = \exp\left(\frac{t}{t_{th}}\right)\mathrm{erfc}\left(\frac{t}{t_{th}}\right) \tag{7}$$

where $t_{th} = (e_w/h)^2$ is the thermal time scale, h being the heat transfer coefficient of vapor flow, T_{w0} being the initial surface temperature before droplet impact, and erfc is the complementary error function.

Different methods were proposed to determine the initial surface temperature to trigger the dynamic Leidenfrost effect, i.e., the dynamic LFP temperature. Limbeek et al. took the value $T_w(t)$ as the static LFP temperature for sessile droplets, where t is the cooldown time [102] or the measured time during which the impacting droplet is within 100 nm above the heated surface [103], and t_{th} is fitted using experimental data. On the other hand, Wang et al. [3] assumed that $T_w(t)$ equals the homogeneous nucleation temperature with t being the time interval spanning the instants of impact and maximum spreading state, and t_{th} is calculated using the heat transfer coefficient value obtained from the fully developed laminar duct flow equation.

Castanet et al. [206] assumed that the minimum surface temperature during droplet impact cooling equals the spinodal temperature T_{sp}, above which no wetting is physically possible. The corresponding expression of the dynamic LFP temperature is

$$T_{\mathrm{LFP}} = T_{sp} + \sqrt{5}(T_{sp} - T_0)e_f / e_w \tag{8}$$

where T_0 is the initial droplet temperature, and e is the thermal effusivity. They indicated that Eq. (8) is valid for droplets with high impact velocities when liquid inertia is predominant over viscous and capillary forces. However, it seems that the impact velocity is neither explicitly nor implicitly included in Eq. (8).

Wu et al. [44] also adopted the transient heat conduction assumption and applied the one-dimensional unsteady Navier-Stokes equation to study the droplet flow by neglecting the viscous friction effect. With appropriations and scaling relations of the characteristic vapor pressure and vapor layer thickness, they derived the superheat degree at the dynamic Leidenfrost condition as

$$\Delta T_{\mathrm{LFP}} \sim \left(\frac{\sqrt{\pi R}}{e_w} + \frac{\sqrt{\mu_g R}}{\lambda_g \sqrt{\rho_f}}\right)\frac{h_{fg}\rho_g\rho_f}{\mu_g R}\sqrt{u} \tag{9}$$

where R is the droplet radius. As illustrated in Eq. (9), ΔT_{LFP} scales with the root square of the impact velocity and the inverse of the solid thermal effusivity. Wu et al. verified these two qualitative trends with experimental data, and good agreement was achieved. It is also indicated by the authors that the assumption of $Re_g = \rho_g u_g \delta_g / \mu_g \ll 1$ is involved during the model derivation with δ_g being the vapor layer thickness. Therefore, Eq. (9) may need further modification beyond this range since the vapor velocity can be relatively high within the thin vapor layer [207].

As can be seen from Eqs. (7–9), this type of model considers the cooling effect during droplet impact and enables the integration of the surface thermal effusivity effect on the dynamic LFP temperature, which is much different from other categories of theoretical models.

3.3. Vapor layer-air layer analogy

For droplet impact on an unheated surface, an air layer is entrapped between the droplet and substrate, which is similar to the generated vapor layer under the dynamic Leidenfrost condition. In either case, as shown in Fig. 17(a), the bottom surface of the impacting droplet is not flat but curved in a dimple-like shape. The air/vapor layer thickness reaches a minimum in the neck region but is much higher in the center. Several studies have scaled the central dimple height and neck region radius of the air layer respectively as $\delta_d = 2.8R\mathrm{St}^{-2/3}$ [208,209] and $R_n = R(3ut/R)^{1/2}$ [210], with St being the Stokes number $\mathrm{St} = \rho_f u R/\mu_a$, which have also been verified for droplet impact in the film boiling regime [41,200].

With analogy to the isothermal case, Gordillo and Riboux [211] assumed that when the dynamic LFP condition is reached, the vapor production rate at the dimple region equals the growth rate of a central cylindrical vapor bubble with radius R_n and height δ_d, i.e., the contribution of the vapor produced in the neck region was neglected. Then, the mass conservation equation yields the following expression of the dynamic LFP temperature as

$$\Delta T_{LFP} = 2.8\mathrm{Pr}_g \mathrm{St}^{1/3} \frac{\rho_{g0}\mu_a h_{fg} T_{sat}}{\rho_f \mu_g c_{pg} T_{ref}} \tag{10}$$

where ρ_{g0} is the vapor density at atmospheric pressure and liquid saturation temperature, and T_{ref} is the average of surface and saturation temperatures. It is noted that the air viscosity is used to calculate the Stokes number in Eq. (10), although the viscosity should correspond to the vapor phase, or more precisely, the vapor-air mixture.

The predicted dynamic LFP temperatures by Eq. (10) agree with low-velocity data reported by Shirota et al. [41], while the deviation increases slightly in the higher impact velocity range. As mentioned by Gordillo and Riboux [211], Eq. (10) is only valid when the characteristic size of the surface protrusions is smaller than the dimple height. Otherwise, the surface asperities with sizes comparable to the dimple height will facilitate vapor layer destabilization and cause droplet-solid contact, inducing a higher dynamic LFP temperature.

3.4. Pressure balance criterion

When a Leidenfrost droplet impacts a high-temperature substrate, the liquid-vapor interface is subject to several pressures (or forces), which can be classified as nonwetting and wetting pressures (see Fig. 17 (b)). The vapor pressure induced by intensive vapor production acts as the nonwetting pressure since it lifts the liquid-vapor interface away from the heated surface. On the contrary, the wetting pressure, which pushes the droplet bottom surface towards the substrate and tends to destabilize the vapor layer, includes the droplet gravity by its own weight, dynamic pressure caused by droplet inertia, and water hammer pressure due to the acoustic wave being accompanied by abrupt deceleration. The droplet gravity is generally neglected since it is several orders of magnitude smaller than the latter two, which are respectively expressed as $P_D = 0.5\rho_f u^2$ and $P_{WH} = k\rho_f uc$. Here c is the speed of sound in the droplet, and the accommodation coefficient k depends on the impact characteristics, droplet size, surface material, and surface morphology [126]. For topographically patterned surfaces, the interaction between the droplet and surface structures can induce an additional wetting pressure component, i.e., capillary pressure associated with the capillary wicking effect. The droplet-vapor interface will maintain separation from the heated substrate (i.e., film boiling) so long as the nonwetting pressure exceeds the wetting ones. Therefore, the dynamic Leidenfrost condition is reached when the two sets are in equilibrium. Overall, this type of model prevails among the theoretical studies of dynamic LFP temperature.

3.4.1. Smooth surfaces

Nigmatulin et al. [212] measured the wetting area of a heated surface during droplet impact and indicated that the transitional droplet-solid contact temperature T^* separating wetting and non-wetting regimes can be determined by equating the vapor pressure and impact pressure to give $P_{sat}(T^*) = 0.5k\rho_f uc$. Further considering the heat diffusion properties of both liquid and solid, the dynamic LFP temperature (which they called the maximum moistening temperature) is expressed as

$$T_{LFP} = T^* + e_f\left(T^* - T_f\right) / e_w \tag{11}$$

When k equals 0.2, Nigmatulin et al. [212] indicated that the root-mean-square deviation of predictions was 22 K compared with their own experimental data.

Liu et al. [138] followed the scaling analysis of droplet spreading characteristics by Tran et al. [115] where a pancake-shaped Leidenfrost droplet was assumed to levitate on a vapor layer with uniform thickness. They supposed that the dynamic pressure is balanced by the vapor pressure to attain the Leidenfrost condition so that the dynamic LFP temperature can be expressed as

$$\Delta T_{LFP} \sim \frac{2G + K}{K} \frac{\rho_g \sigma h_{fg} \delta_g^4}{\mu_g \lambda_g d^3} \mathrm{We}^{1-2n} \tag{12}$$

In Eq. (12), the maximum spreading diameter $d_{max} \sim d_0 \mathrm{We}^n$ is implicitly integrated, and the dimensionless coefficients G and K stem

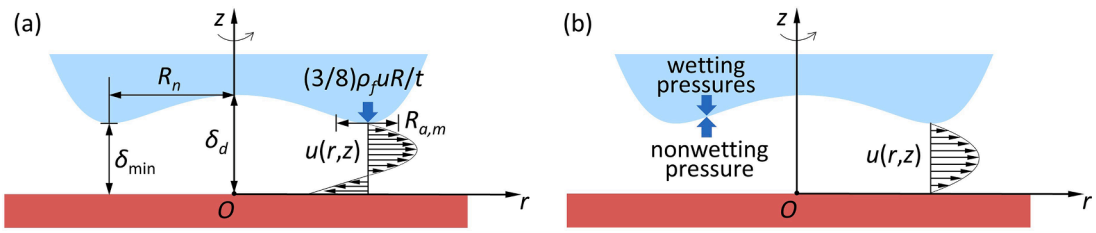

Fig. 17. Schematic of an impacting droplet in the film boiling regime. (a) The pressure difference in a region of width $R_{a,m}$ and the relative motion between the neck region and the heated wall induce Poiseuille and Couette flows. Adapted from Riboux and Gordillo [211]; (b) Wetting and nonwetting pressures acting on the liquid-vapor interface. In the pressure balance criterion, Poiseuille flow is generally assumed.

from the contact temperature expression of $T_c = (2GT_{sat} + KT_w)/(2\ G + K)$ by Breitenbach et al. [213].

Park et al. [60,61] combined the one-dimensional steady-state Darcy equation and mass conservation equation to scale the vapor pressure. When it comes to the water hammer pressure, they considered the unsteady term in the Navier-Stokes equation to yield $P_{WH} \sim \rho_f d_0(u/t)$, which is different from the expression in other studies ($P_{WH} = k\rho_f cu$). It was pointed out that $t \sim \delta_g/u$ is the time scale related to the triggering of the dynamic Leidenfrost effect. By equating the water hammer pressure and vapor pressure, they derived the following expression as

$$\Delta T_{\mathrm{LFP}} \sim \frac{\rho_f \rho_g h_{fg} u^2}{\mu_g \lambda_g}\delta_g^2 \tag{13}$$

It is seen from Eq. (13) that the value of vapor layer thickness is intrinsically required to calculate the dynamic LFP temperature. They further focused on the initial formation of the vapor layer upon droplet impact, and proposed the scaling of vapor layer thickness (this will be introduced in Section 4). Then, the explicit relation of the dynamic LFP temperature is derived as

$$\Delta T_{\mathrm{LFP}} \sim \frac{\rho_g h_{fg} \sigma d}{\mu_g \lambda_g}\mathrm{We}^n \tag{14}$$

where the exponent depends on the Weber number, i.e., $n = 1/2$ or $1/3$ for $\mathrm{We} < 10$, otherwise, $n = 1/5$.

Park and Kim [120] neglected the dynamic pressure since it is several orders of magnitude smaller than the water hammer pressure. Assuming laminar Poiseuille flow of the vapor phase, they combined the mass conservation and Fourier's conduction law to derive the following expression of the dynamic LFP temperature

$$\Delta T_{\mathrm{LFP}} \sim \frac{\rho_f \rho_g h_{fg} kuc\delta_g^4}{\mu_g \lambda_g d^2} \tag{15}$$

Another theoretical study by the same authors [121] considered the transient growth of vapor layer thickness during the early stage of impact with the aid of the energy conservation equation, and the vapor layer thickness was obtained as a function of surface temperature. They also derived another expression of water hammer pressure as $P_{WH} = \eta\rho_f u^2 d/\delta_g$, where η is an adjustable coefficient related to the length scale of rapid deceleration of the liquid particles inside the droplet. Simultaneously solving the equations of vapor layer thickness and pressure balance, they obtained the following equation to calculate the dynamic LFP temperature

$$\Delta T_{\mathrm{LFP}} = \frac{2\rho_f \rho_g h_{fg} u^2 \delta_g^4 \left(1 + 2\eta d/\delta_g\right)}{3\mu_g \lambda_g d^2} \tag{16}$$

where η is fitted to be 0.0287 to achieve agreement with experimental data.

Following the same procedure, Du et al. [141] and Guo et al. [129] also developed theoretical formulae for dynamic LFP temperature prediction, which are respectively expressed as

$$\Delta T_{\mathrm{LFP}} = \frac{4\rho_g h_{fg} \delta_g^4}{\mu_g \lambda_g d^2}\left(\frac{4\sigma\cos\theta}{d} + \frac{2\rho_f g d}{3}\right) \tag{17}$$

$$\Delta T_{\mathrm{LFP}} = \frac{\rho_g h_{fg} \delta_g^4}{6\mu_g \lambda_g R_c^2}\left(\frac{2}{3}\pi\rho_f g d + \rho_f u^2 + \frac{2\eta\rho_f u^2 d}{\delta_g^4}\right) \tag{18}$$

where θ is the contact angle. Du et al. [141] pointed out that they neglected the dynamic pressure since it only plays a role during the initial impact stage. Therefore, the vapor pressure is balanced by the sum of capillary and gravitational pressures in Eq. (17).

3.4.2. Structured surfaces

The above-reviewed models are applicable to droplet impact on a smooth substrate. However, as shown in Section 2.2, surface topography greatly affects the dynamic LFP temperature, and some theoretical studies have been correspondingly conducted. Dimension parameters of different surface microstructures involved in these models are shown in Fig. 18.

Applying the one-dimensional Darcy equation and effective thermal conductivity λ_g^{eff}, Park and Kim [120,121] further extended their dynamic LFP temperature models for droplet impact on smooth surfaces to microtextured surfaces as

$$\Delta T'_{LFP,MT} \approx 12K_p \Delta T_{LFP} \frac{\delta_g^2 \lambda_g}{\delta_g^4 \lambda_g^{eff}} \tag{19}$$

where ΔT_{LFP} is expressed by Eqs. (15) and (16) for a smooth surface, and δ_g' is the vapor layer thickness on the micropillar array surfaces. The Darcy permeability for vapor flow, K_p, can be calculated by applying the one-dimensional flow resistance concept, while the three-dimensional heat diffusion equation is numerically solved to obtain the effective thermal conductivity, λ_g^{eff}, both dependent on the vapor layer thickness, δ_g' [121]. Sahoo et al. [135] also provided a similar theoretical analysis of the dynamic LFP temperature on a nanowire array surface. However, their expression did not include the effect of impact momentum, and the vapor layer thickness value of a sessile droplet was adopted. Therefore, the prediction agreed well only with low-We data. Recently, Guo et al. [129] also derived a similar formulation to Eq. (19) for microgroooved surfaces.

Li et al. [116] developed a dynamic LFP temperature model for droplet impact on a structured surface with a micro-post array gradient. They attributed the shear loss to both the vapor layer above the post arrays (with a thickness of δ_g) and vapor flow inside the post arrays (with a mass proportion of χ), and then calculated the total pressure gradient using the parallel circuit concept. By balancing the water hammer pressure with the vapor pressure, the superheat degree required for the dynamic Leidenfrost condition is expressed as

$$\Delta T_{\mathrm{LFP}} \sim \frac{c\delta_g k u \rho_f \rho_g h_{fg}\left(\delta_g + H\right)}{\mu_g \lambda_g R_c^2}\left[\frac{\chi}{L^2} + \frac{1}{\left(\delta_g + H\right)^2}\right]^{-1} \tag{20}$$

where L and H are, respectively, the post-to-post spacing and post height shown in Fig. 18(a), R_c is the contact radius between the droplet bottom and the vapor phase, and k is calculated using a correlation with the capillary pressure [214].

Kim [123] theoretically analyzed the nonwetting vapor pressure and wetting pressure (the sum of capillary, water hammer, and dynamic pressures) acting on the liquid-vapor interface for droplet impact on a micropillar array surface, and the pressure balance is expressed as

$$\frac{\mu_g R_c^2 \Delta T_{\mathrm{LFP}}}{6K_{UC} H h_{fg} \rho_g R_{UC}} = \frac{\pi\sigma D\cos\theta_r}{\varepsilon L^2} + \beta\rho_f u^2 + 0.5\rho_f u^2 \tag{21}$$

where θ_r is the receding contact angle.

In Eq. (21), they newly defined the water hammer pressure as $P_{\mathrm{WH}} = \beta\rho_f u^2$, where β is an adjustable parameter that can be fitted with the surface porosity $\varepsilon = 1 - \pi D^2/4L^2$ (see Fig. 18(b)). K_{UC} is the total effective permeability for the vapor flow in a unit cell, which can be calculated by considering the velocity gradient effect in different flow directions. R_{UC} is the total thermal conduction resistance per unit area in the vapor region of the unit cell, which can be obtained from numerical simulations. The contact radius R_c is fitted as $R_c \sim t_c^{0.2}$, where t_c is the characteristic time spanning from the instant of droplet impact to the onset of the dynamic Leidenfrost phenomenon.

In the model proposed by Jerng and Kim [126], the acoustic wave absorption into the compressible vapor layer was considered (see Fig. 19 (a)). An analytical approach was integrated to calculate the coefficient k in the water hammer pressure relation under the effect of microchannel

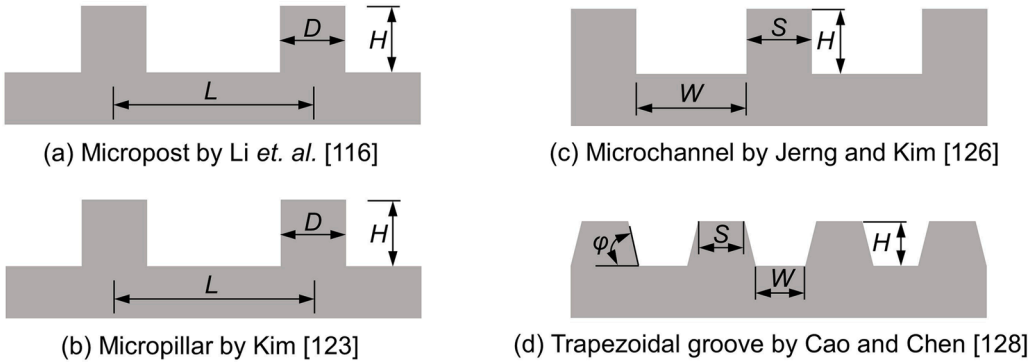

FIg. 18. Dimension parameters of different surface microstructures.

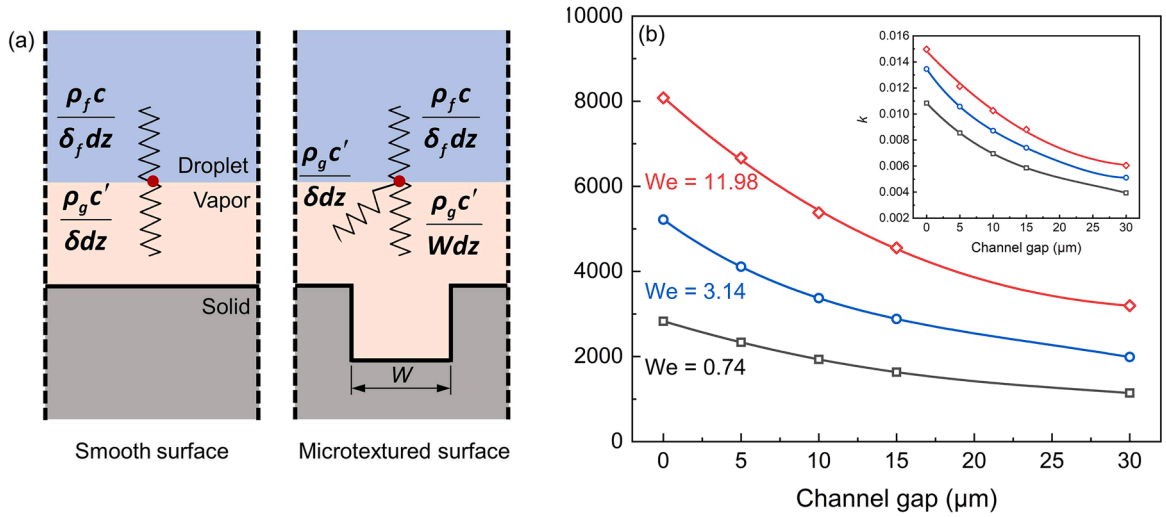

Fig. 19. (a) Schematic of acoustic resistance for smooth and microchannel-shaped surfaces. (b) Calculated water hammer pressures. Adapted from Jerng and Kim [126].

structures shown in Fig. 18(c), which is expressed as

$$k = \left[1 + \frac{\rho_f c}{\rho_g c'} \frac{\delta_g + W}{\delta_f}\right]^{-1} \tag{22}$$

where c' is the speed of sound in the vapor, δ_f is the droplet height, and W is the channel gap with $W = 0$ indicating a smooth surface. Then, the dynamic LFP temperature can be determined by $P_D + P_{WH} = P_g$ with simulated vapor pressure and measured droplet height at the maximum spreading state. It is interesting to note in Fig. 19(b) that the calculated k value is at least an order of magnitude smaller than the 0.2 used in other studies for smooth surfaces [203,215]. However, a simple order of magnitude analysis [158] showed that the vapor pressure is typically in the order of 10^6 Pa for an impacting water droplet, which is much higher than the sum of dynamic pressure (~10^3 Pa) and water hammer pressure (~10^3–10^4 Pa in Fig. 19(b)).

Cao and Chen [128] focused on the dynamic LFP temperature of droplet impact on trapezoidal grooved surfaces, whose dimension parameters are shown in Fig. 18(d). In their model, it was assumed that heat is transferred via forced convection rather than conduction through the vapor layer, and a Nusselt number correlation was adopted to calculate the heat flux. Considering the balance between surface tension force and vapor pressure, where the effect of impact momentum was neglected for low impact velocity cases, they derived the following equation

$$\Delta T_{\mathrm{LFP}} = (EW)^{2/3} \left(\frac{H}{W}\right)^{k_1} \left(\frac{2H + W + S^2}{4HW}\right)^{k_2} \frac{2H(1 + \cot\varphi) + S + W}{H(W + H\cot\varphi)} \tag{23}$$

The explicit expression of the parameter E was not provided in their study, while all other variables in Eq. (23) are dimension parameters of the trapezoidal grooved surface. Overall, they indicated that the model predictions show good agreement with the data, including data with different groove widths and depths.

Recently, Du et al. [141] extended their model for droplet impact on a smooth surface (i.e., Eq. (17)) to micro/nanostructured and macro-pillar surfaces by simply modifying the vapor pressure formulations, which are respectively expressed as

$$\Delta T_{\mathrm{LFP}} = \frac{\rho_g h_{fg} (\delta_g + R_p)^4}{\mu_g \lambda_g d^2} \left(\frac{4\sigma\cos\theta}{d} + \frac{2\rho_f g d}{3}\right) \tag{24}$$

$$\Delta T_{\mathrm{LFP}} = \frac{16\rho_g h_{fg} K_p H^2}{\mu_g \lambda_g d^2} \left(\frac{2\sigma\cos\theta}{S} + \frac{2\rho_f g d}{3}\right) \tag{25}$$

where R_p is the average peak height of micro/nanoscale structures, and K_p is the surface permeability.

Lee et al. [153] theoretically analyzed the dynamic Leidenfrost phenomenon in the scenario of droplet impact on a thin wire. Assuming that the buoyancy force equals the weight of the daughter droplet resulting from droplet breakup, they expressed the dynamic LFP temperature with the aid of several approximations as

$$\Delta T_{\mathrm{LFP}} \sim \frac{u\rho_f\rho_g h_{fg} R}{3(\rho_f-\rho_g)\lambda_g} \tag{26}$$

This scaling relation prediction shows good agreement with data. However, it should be noted that vapor pressure and water hammer pressure are not considered in the force balance equation. Also, the wire diameter, which appreciably influences the interfacial evolution, is not included in Eq. (26). This may motivate future modifications to consider the effect of the droplet-wire size ratio.

Khavari and Tran [33] argued that the dynamic LFP temperature is related to the oscillating boiling phenomenon, which is governed by the competing forces of capillary-inertia-induced rewetting and heterogeneous boiling. During the time t for heterogeneous boiling to generate a vapor layer with a thickness of $2r_c$, the upward vapor generation velocity is balanced by the downward impact velocity at the dynamic Leidenfrost condition, i.e.,

$$u = 2r_c / t \tag{27}$$

where r_c is the critical vapor embryo radius for heterogenous nucleation, $t = Jr_c^2$ with J being the heterogenous nucleation rate, while r_c and J are both evaluated at T_{LFP}. The predictions obtained by Eq. (27) agree well with data for various liquids except for water which has a much higher heat capacity and latent heat, which they explained by the non-negligible decrease in the surface temperature during the impact process. Also, Khavari and Tran noted that Eq. (27) is not applicable to low impact velocity cases where viscous stress by the air-vapor flow begins to play a dominant role.

3.5. Discussions

Each type of theoretical model reviewed above has its respective advantage in predicting the dynamic LFP temperature. For instance, the mechanistic model constructed around the vapor bubble dynamics by Bernardin and Mudawar [203] integrates the surface roughness effect. Meanwhile, it is essentially different from other models since it considers the triggering of dynamic LFP temperature by vapor layer formation rather than vapor layer collapse. However, the model calculation requires surface cavity size characterization, which is inconvenient when using multifarious substrates. The model based on transient heat conduction during droplet impact considers the cooling effect and the solid thermal effusivity. Different assumptions are adopted in different studies to determine the terms in Eq. (7), and to calculate the dynamic LFP temperature. The analogy between the vapor layer and air layer by Gordillo and Riboux [211] yields the dynamic LFP temperature expression, which they proposed as the minimum substrate temperature to prevent liquid-solid contact at the central part of the droplet bottom, although the neck region seems to be more vulnerable to the surface protrusions.

On the other hand, it is seen that the majority of the models based on the pressure balance criterion intrinsically depend on vapor layer thickness. As will be shown in Section 4, however, the vapor layer thickness affected by multiple factors shows complicated spatial and temporal distributions, which brings a great challenge for accurate theoretical modeling. To solve this issue, Park and Kim [60,61], as well as Li et al. [116], reversely calculated the vapor layer thickness using droplet thermophysical properties, Weber numbers, and measured dynamic LFP temperatures. On the other hand, Jerng and Kim [126] adopted the numerically simulated vapor layer thickness when predicting the dynamic LFP temperature. It is concluded that accurate prediction of vapor layer thickness is of great importance for dynamic LFP temperature model calculation, which warrants further intensive theoretical studies.

Another prerequisite to quantitatively calculate the dynamic LFP temperature is the liquid-vapor interface temperature, which is all taken as saturation temperature in the above theoretical models. However, this temperature is somewhat difficult to determine with unknown pressure at the liquid-vapor interface, which cannot be simply regarded as the ambient pressure. Moreover, Bertola [45] estimated that the time required for a millimeter-sized impacting droplet to reach saturation is significantly longer than the contact time. Therefore, the droplet temperature is close to the initial value. On the other hand, Castanet et al. [206] indicated that the thermal contact during droplet impact can be very rapid and intense, causing the droplet temperature to exceed the saturation temperature and even reach the spinodal temperature. Thus, how to accurately determine the droplet-vapor interface temperature still remains an open question.

To sum up, most of the existing prediction models are semi-quantitative and also rely on either experimental measurements or simulated results. Furthermore, only part of the parameters that affect the dynamic LFP temperature is integrated. Therefore, the physics-based quantitative models still need to be developed to fully elucidate the mechanisms and reliably predict the dynamic LFP temperature.

4. Vapor layer thickness underneath an impacting droplet

As indicated by the theoretical models reviewed in Section 3, the dynamic LFP temperature is closely related to the vapor layer underneath an impacting droplet, which shows complicated temporal and spatial evolution characteristics. Measurements showed that the time to form a continuous vapor layer is extremely short, e.g., approximately 0.03 ms for a water droplet at T_w = 210 °C and We = 60 [216]. In general, the vapor layer exhibits a dimple shape [41] with a thickness ranging from several hundreds of nanometers [103] to several micrometers [49,217] during droplet spreading and receding, intricately influenced by surface temperature and the influence factors that affect the dynamic LFP temperature. Such inherent complexity brings great difficulty in both the modeling and measurement of vapor layer thickness.

4.1. Theoretical modeling

Assuming a flat-bottomed sessile droplet in the film boiling regime, Wachters et al. [218] derived a vapor layer thickness relation based on mass, momentum, and energy conservation analysis. Later, they further extended this model to an impacting droplet by modifying the force imposed by the droplet on the heated surface [219]. When deriving the model, they made and justified several assumptions, such as a quasi-stationary vapor temperature profile, isothermal surface, and negligible effects of radiation and vertical vapor velocity. They indicated that the only serious uncertainty relates to the shape of the droplet bottom surface, which may be thinner in the middle than under the expanding brim (note that this is inconsistent with other studies where the vapor layer thickness decreases radially). In the proposed vapor layer thickness expression (which is tabulated in Table 5 together with other models discussed in this section), both the height of the center of gravity and the droplet-solid contact radius are measured from captured images during droplet impact. Fig. 20 compares the calculated vapor layer thickness under a sessile droplet and impacting droplets with various velocities.

Rein [220] developed a disk model to account for the dynamic Leidenfrost effect of an impacting droplet at the maximum spreading state. He assumed that the interface acceleration is caused by pressure difference and the gravitational acceleration. This yields an expression of the second derivative of vapor layer thickness (see Table 5). With a similar derivation to the sessile droplet analysis, Guo and Mishima [221] derived the expression of vapor layer thickness under an impacting droplet. The modification was also embodied in the force balance equation, where the pressure integrated over the entire vapor base is balanced by impact momentum rather than droplet weight. Later, Lelong et al. [222] conducted a follow-up analysis with different methods to predict the contact diameter, heat transfer rate, and

Table 5
Theoretical formulae of vapor layer thickness under an impacting droplet.

Reference	Theoretical expression	Time-varying	Spatially-nonuniform	Temperature-dependent	Velocity-related
Wachters and Westerling [218]	$\delta_g = \left[\frac{9\mu_g\lambda_g(T_w - T_{sat})(T_w + T_{sat})^3 R_c^4}{64\rho_g\rho_f h_{fg} T_{sat}^3 R^3}\right]^{1/4}\left(g + \frac{d^2h_0}{dt^2}\right)^{-1/4}$	✓	×	✓	✓
Rein [220]	$\frac{d^2\delta_g}{dt^2} = \left\{\frac{\rho_g\pi R_{max}^4}{16\delta_g^2}\left[3\left(\frac{d\delta_g}{dt}\right)^2 + 4v\frac{d\delta_g}{dt} + v^2 - 2\delta_g\frac{dv}{dt}\right] - mg\right\}\left(m + \frac{\rho_g\pi R_{max}^4}{8\delta_g}\right)^{-1}$ where $v = -q/\rho_g h_{fg}$	✓	×	✓	✓
Guo and Mishima [221]	$\delta_g = \left[\frac{9\mu_g\lambda_g(T_w - T_{sat})t_r d}{32\rho_g\rho_f h_{fg} u}\right]^{1/4}\frac{R_c}{R}$	×	×	✓	✓
Lelong et al. [222]	$\delta_g = \left[\frac{9\mathrm{Nu}\mu_g\lambda_g(T_w - T_{sat})R}{4\rho_g\rho_f h_{fg}(g + 2u/t_r)}\right]^{1/4}\frac{R_c}{R}$	×	×	✓	✓
Gilet and Bush [223]	$\delta_g \sim \left[\frac{\mu_g\lambda_g R^3(T_w - T_{sat})}{\rho_g h_{fg}\sigma}\right]^{1/4}\mathrm{We}^{-1/4}\mathrm{forvaporthrustdominant}\delta_g \sim \left(\frac{\mu_g^2 R^3}{\rho_f\sigma}\right)^{1/4}\mathrm{We}^{-1/2}\mathrm{forlubricationforcedominant}$	×	×	✓	✓
Park and Kim [60,61]	$\delta_g \sim \begin{cases} R\mathrm{We}^{-1/3}, \mathrm{We} < 10 \\ R\mathrm{We}^{-2/5}, \mathrm{We} > 10 \end{cases}$ or $\delta_g \sim \begin{cases} R\mathrm{We}^{-1/4}, \mathrm{We} < 10 \\ R\mathrm{We}^{-2/5}, \mathrm{We} > 10 \end{cases}$	×	×	×	✓
Castanet et al. [227]	$\frac{d\delta_g}{dt} = -\frac{\alpha\delta_g}{t} + \frac{1}{\rho_g h^*_{fg}}\left[\frac{\lambda_g(T_w - T_{sat})}{\delta_g} - \frac{\sqrt{5}e_f(T_{sat} - T_0)}{\sqrt{\pi t}}\right] - \frac{17\delta_g^3}{15\mu_g R_c^2}\rho_f u^2\exp\left(-\frac{3.1ut}{d}\right)$, where $h^*_{fg} = h_{fg} + (c_{pg}T_g - c_{pg,sat}T_{sat})$	✓	×	✓	✓
Park and Kim [121]	$\delta_g = \frac{2\lambda_g(T_w - T_{sat})}{\rho_g u h_{fg}}$ or $\delta_g = \left[\frac{3\mu_g d^2}{4\rho_f u(1 + 2\eta d/\delta_g)}\right]^{1/3}$	×	×	✓	✓
Chantelot and Lohse [200]	$\delta_{g,min} \sim R\mathrm{We}^{-1}\left[\frac{\mu_g\lambda_g(T_w - T_{sat})}{\sigma\rho_g R h_{fg}}\right]^{1/2}$	×	✓	✓	✓
Gordillo and Riboux [211]	$\delta_{g,min} = RC(8\mu_g/\pi\mu_a)^{1/2}\mathrm{St}^{-7/6}[\sqrt{1 + 2(\mu_a/\mu_g)\psi/3} - 1]^{1/2}$ where $\psi = \frac{\rho_f\lambda_g\Delta T}{\rho_g\mu_a h_{fg}}$, $C^{5/2} = 12.4^{3/2}(C + \psi\mathrm{St}^{-1/3})$	×	✓	✓	✓
Lee et al. [224]	$\delta_g = 730h_{fg}^{-0.42}(T_w - T_{sat})^{0.5}t^{0.5}$	✓	×	✓	×
Tran et al. [115]	$\delta_g = \left[\frac{\mu_g\lambda_g(T_w - T_{sat})}{d\rho_g h_{fg}\sigma}\right]^{3/10} d\mathrm{We}^{-1/10}$	×	×	✓	✓
Wildeman and Sun [225]	$\delta_g \sim R\mathrm{We}^{1/2}$	×	×	×	✓
Breitenbach et al. [213]	$\delta_g = \frac{Ae_w(T_{w0} - T_{sat})}{\rho_f h_{fg}}\sqrt{t}$, where $A = \sqrt{(B_1 - B_2)^2 + \frac{B_2}{\sqrt{\pi}}} - B_1 - B_2$ $B_1 = \frac{\sqrt{5}e_f(T_{sat} - T_0)}{\sqrt{\pi}(T_{w0} - T_{sat})e_w}, B_2 = \frac{\sqrt{\pi}\lambda_g\rho_f h_{fg}}{2(T_{w0} - T_{sat})e_w^2}$	✓	×	✓	×

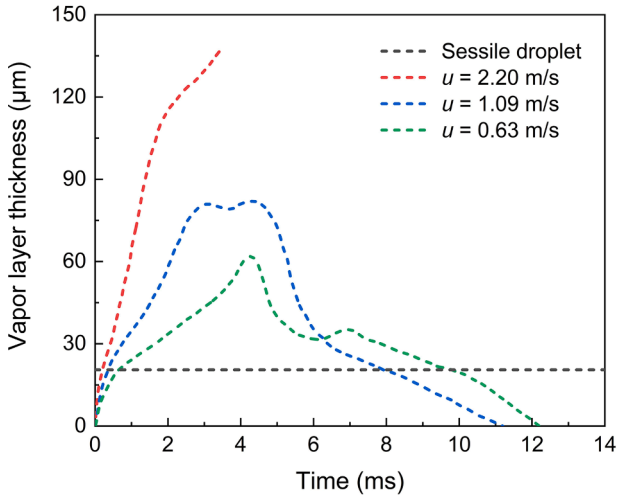

Fig. 20. Calculated vapor layer thickness for water droplets ($d = 2.3$ mm) with different impact velocities. Adapted from Wachters and Westerling [219].

residence time, yielding a new relation of vapor layer thickness.

Gilet and Bush [223] classified the Leidenfrost droplet impact into lubrication-force-dominated and vapor-thrust-dominated conditions, and expressed the corresponding vapor layer thickness by solving the mass, momentum, and energy conservation equations. Lee et al. [224] supposed that the increase in the vapor layer thickness during droplet impact is caused by the difference between the vapor production rate and vapor evacuation rate, while the latter is negligibly small compared to the former based on dimension analysis. Their proposed formula agreed well with data for methanol, ethanol, and isopropanol droplets with a fitted property-relevant coefficient.

Tran et al. [115] scaled the vapor layer thickness at the instant of the maximum spreading state. To simplify the derivation, they assumed that the impacting droplet takes the shape of a pancake with the maximum spreading diameter, and the vapor layer thickness and radial vapor velocity are both uniform. With the aid of conservation equations, the force balance between the drag force caused by viscous vapor flow and capillary force yields the vapor layer thickness expression.

It is supposed by Wildeman and Sun [225] that the droplet decelerates over a distance of δ_g during impact, which results in an effective gravitational acceleration of $g' = u^2/\delta_g$ in the frame of reference of the droplet. Replacing the corresponding term in the sessile droplet expression [226] to account for the impact momentum effect yields the vapor layer thickness under an impacting droplet. They indicated that an equivalent derivation procedure is to simply equate the kinetic energy $\rho_f R^3 u^2$ with the surface deformation energy $\sigma\delta_g^2$. However, it is seen that the effect of surface temperature is not included in this scaling relation.

The spatially uniform vapor layer thickness was also formulated by Castanet et al. [227] by applying energy and momentum balance equations to the vapor layer. They partitioned the wall heat flux for liquid heating, evaporation, and vapor heating, and then analytically calculated the droplet temperature field. Combining the impact force equation for droplet impact on an unheated surface [228], they derived the time rate of change in the vapor layer thickness. It was indicated that for highly subcooled droplets, the vapor layer thickness is independent of the impact velocity since the local heat flux transferred to the liquid dominates.

Park and Kim [60,61] focused on the formation of a dimple-shaped interface at the initial moment of droplet impact, which is subject to inertial force and surface tension. The length scale of the curved interface (i.e., the vapor layer thickness) equals the capillary length $\kappa^{-1} = [\sigma/(\rho_f \xi)]^{1/2}$, where ξ is the inertial force-induced acceleration. It was assumed that the droplet rapidly decelerates from u to 0 during a time period of δ_g/u, which yields $\delta_g \sim d\mathrm{We}^{-1/4}$. They found this relation agrees well with low Weber number data, but remarkable deviation occurs when $\mathrm{We} > 10$, where they supposed that viscous friction begins to take effect. By fitting the calculated values of δ_g/R from Eq. (14) and experimental data, they finally derived a piecewise expression for the vapor layer thickness, where the exponent is also relevant to the Weber number similar to Eq. (14). In a follow-up study by the same authors [121], the initial transient stage before forming a quasi-equilibrium vapor layer was considered. The temporal variation rate of vapor layer thickness can be determined from the energy conservation equation. Integrating the expression within a time interval during which the droplet-vapor interface velocity equals the growth rate of vapor layer thickness, they obtained the vapor layer thickness expression with the aid of the dynamic LFP temperature relation Eq. (16).

With analogy to the derivation process of air layer thickness for droplet impact on an unheated surface, Chantelot and Lohse [200], as well as Gordillo and Riboux [211] extended the previous models [209, 210] to an impacting Leidenfrost droplet to incorporate the effect of evaporation by coupling the classical viscous lubrication equations. They deduced two different equations for the minimum gas layer thickness at the neck region, where they regarded the gas layer as consisting of both produced vapor and entrapped air. They proposed that the gas pressure at the neck region is determined by liquid inertia and vapor production, and ultimately balanced by the increasing interfacial curvature. This is probably the first reported theoretical model in the literature to calculate the minimum vapor layer thickness in droplet impact cases. As shown in Fig. 21, the model predictions achieve a satisfactory agreement with experimental data.

Breitenbach et al. [213] solved the energy equations of the solid and liquid phases to obtain the heat fluxes at vapor-solid and liquid-vapor interfaces, which are respectively indicated in Fig. 22. The heat flux in the thin vapor layer, $\dot{q}_g$, is calculated by Fourier's law of heat conduction. Then, substituting the three expressions to the overall energy balance equation of $q''_l = q''_g = \dot{q}_2 + \rho_f h_{fg} d\delta_g/dt$ yields the temporal variation rate of vapor layer thickness seen in Eq. (28), which can be solved to obtain an explicit solution shown in Table 5.

$$\rho_f h_{fg} \frac{d\delta_g}{dt} = \frac{e_w \lambda_g (T_{w0} - T_{sat})}{\sqrt{\pi t} k_g + e_w \delta_g} - \frac{\sqrt{5} e_f (T_{sat} - T_0)}{\sqrt{\pi t}} \tag{28}$$

The aforementioned models for vapor layer thickness prediction are tabulated in Table 5. Theoretically speaking, the vapor layer thickness

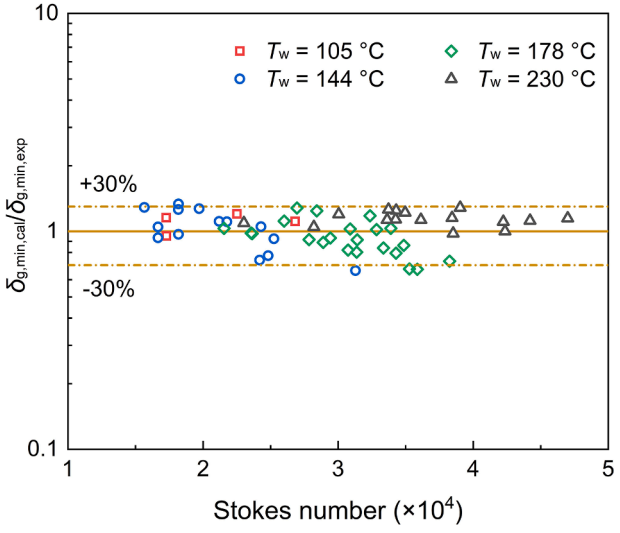

Fig. 21. Comparison of the predicted minimum vapor layer thickness by Gordillo and Riboux [211] and the measured value for ethanol droplet impact on smooth sapphire by Chantelot and Lohse [200].

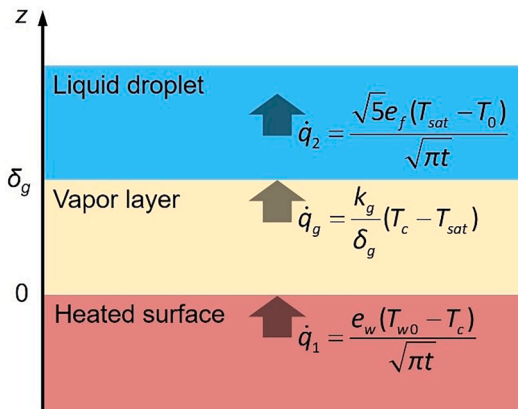

Fig. 22. Schematic of heat fluxes during film boiling of an impacting droplet. The vapor-solid interface is located at $z = 0$ and the liquid-vapor interface is located at $z = \delta_g$. Adapted from Breitenbach et al. [213].

underneath an impacting droplet is time-varying, spatially nonuniform, related to impact velocity, and temperature-dependent. However, it is seen from the table that the existing relations fail to reflect these characteristics more or less. It should also be noted that although being exponential functions of the Weber number, the vapor layer thickness by Wildeman and Sun [225] is positively associated with the Weber number, which is just the reverse of that by Gilet and Bush [223], as well as Park and Kim [60,61].

4.2. Experimental measurement

The measurement of the vapor layer thickness under an impacting droplet requires the detection of the liquid-vapor interface with sufficiently high spatial and temporal resolutions, which is a great challenge for conventional optical imaging techniques due to strong light reflection and visible light scattering. It was shown that the liquid-vapor interface can be clearly captured with ultrafast X-ray imaging [229], and the vapor layer thickness can be obtained with total internal reflection [43,103].

Using the laser optical method, Inada et al. [230] measured the time evolution of vapor layer thickness during the latter half of the residence time. They found an obvious effect of the subcooling degree on the fluctuated vapor layer thickness, e.g., less than 5 μm for $\Delta T_{sub} = 88$ K and more than 10 μm for $\Delta T_{sub} = 2$ K. However, the spatially nonuniform distribution of vapor layer thickness was not provided.

Tran et al. [49] conducted interferometrical measurements of the vapor layer thickness at a certain instant after droplet impact in the gentle film boiling regime via a color high-speed camera. As shown in Fig. 23, the vapor layer thickness profile exerts a dimple-like shape, which is quite similar to the air layer thickness for droplet impact on an unheated surface [231]. Furthermore, Tran et al. pointed out that the vapor layer thickness is one order of magnitude smaller than the sessile droplet case [232], even with such a low Weber number.

Recently, Lee et al. [217] adopted the synchrotron X-ray imaging technique to detect the liquid-vapor interfacial behavior underneath an impacting ethanol droplet on a SiO_2-coated silicon wafer at the early spreading stage. They pointed out that film boiling is featured by final droplet levitation rather than initial droplet rebound. Therefore, momentary droplet-solid contact is still possible at a surface temperature slightly higher than the dynamic LFP temperature, and vigorous nucleation inside the droplet can be observed. Further increasing the surface temperature yields obvious formation and progression of the vapor layer profile, and the measured thickness of the vapor dome at the central position is shown in Fig. 24. With the same technique, however, Lee et al. [224] observed that the vapor layer thickness is uniform and increases linearly with the square root of time (see Fig. 25). When

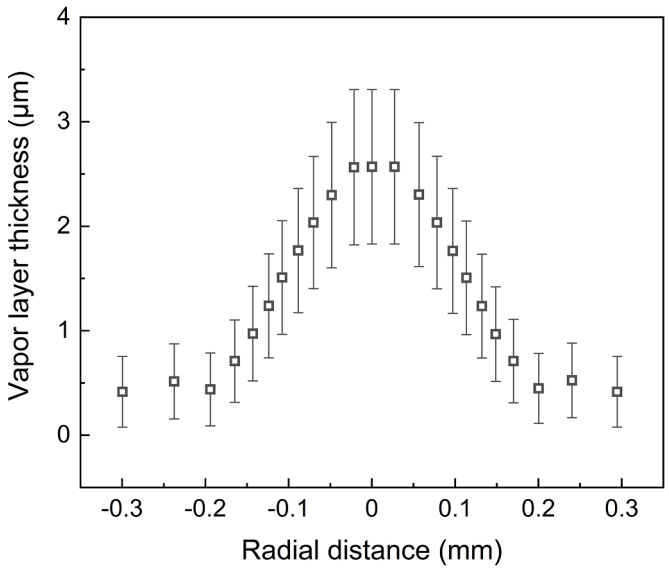

Fig. 23. Measured vapor layer thickness using high-speed color interferometry for a water droplet at $T_w = 350$ °C and We = 3.5. Adapted from Tran et al. [49].

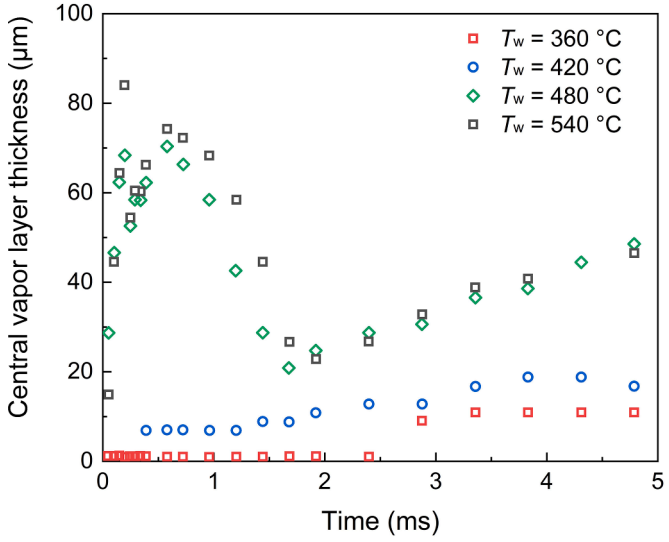

Fig. 24. Time evolution of vapor layer thickness at the central position at various surface temperatures for an ethanol droplet with We = 63.6. Adapted from Lee et al. [217].

attaining a critical thickness, peripheric ripples are generated and then propagate to the center with growing amplitude, which decreases the vapor layer thickness.

Recently, Chantelot and Lohse [200] took the respective advantages of single-wavelength reflection interference and total internal reflection imaging to measure the gas layer thickness composed of air and vapor for droplet impact in the film boiling regime. As shown in Fig. 26, they found that the minimum layer thickness at the neck region strongly increases with the surface temperature, while the non-monotonical dependence is weak for the central dimple height, both decreasing with the impact velocity. Therefore, they concluded that the minimum layer thickness strongly depends on vapor production, while the vapor layer thickness in the central region is subject to gas drainage and liquid inertia.

In the above investigations, the vapor layer thickness is directly measured with advanced optical techniques, while Jung et al. [40], Park and Kim [233], Chaze et al. [234], as well as Castanet et al. [227],

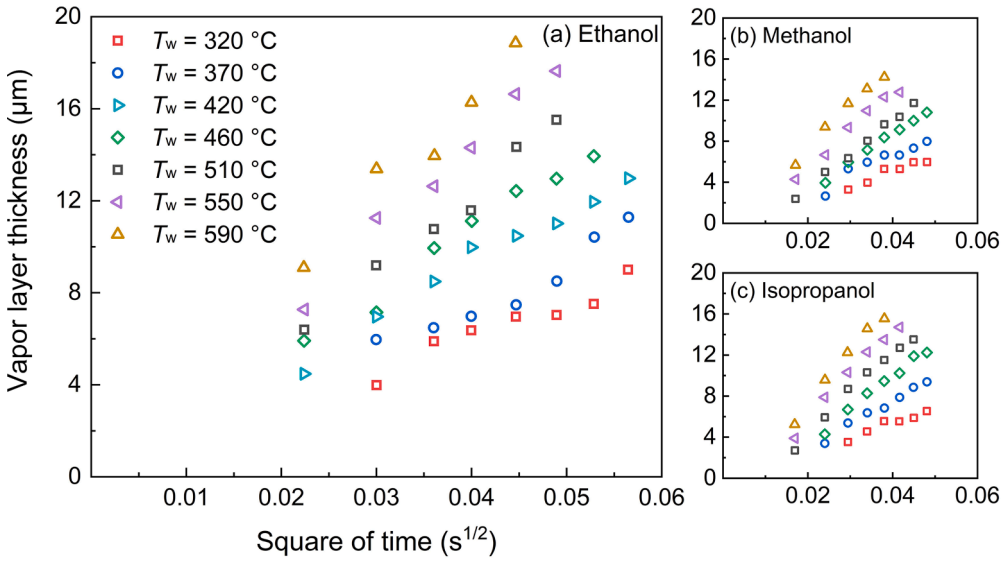

Fig. 25. Variation of vapor layer thickness versus square of time for various substrate temperatures and liquid types. Adapted from Lee et al. [224].

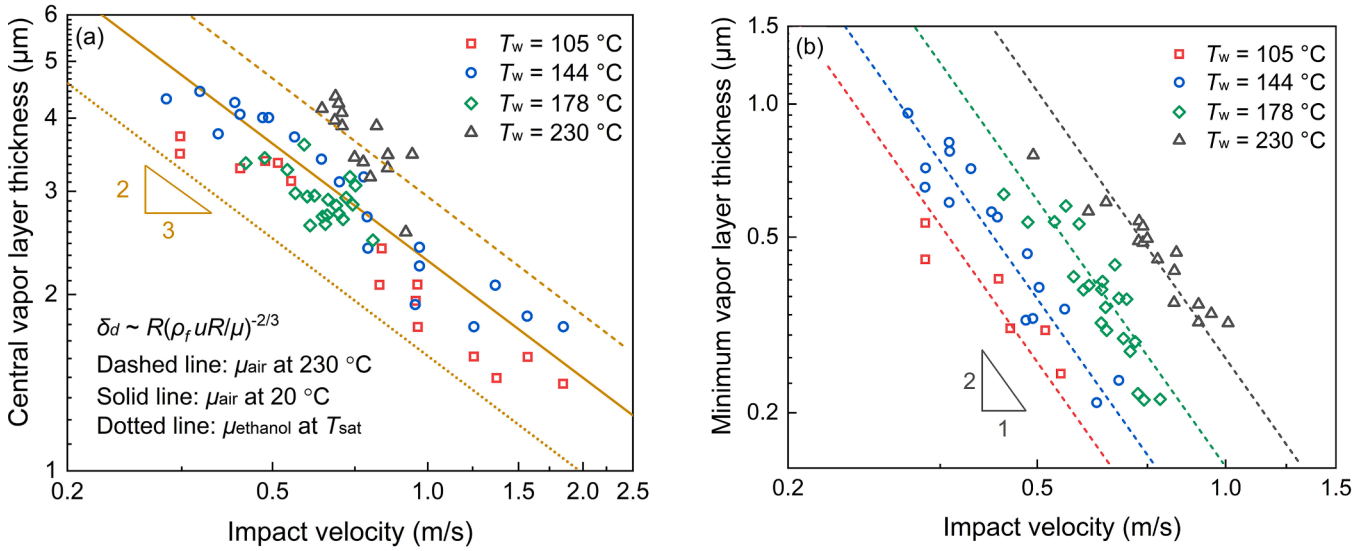

Fig. 26. Variation of vapor layer thickness in the (a) central region and (b) neck region with impact velocity at various surface temperatures. Adapted from Chantelot and Lohse [200].

reported their results from indirect measurement, as shown in Figs. 27 and 28. The infrared-transparent sapphire target enables infrared thermometry of the top-surface temperatures [40,233,234], and Castanet et al. [227] also adopted two-color laser-induced fluorescence imaging to record the droplet temperature. These measured temperatures act as the boundary conditions to numerically solve the heat conduction equations to obtain the surface heat fluxes during droplet impact. In this case, the vapor layer thickness can be simply calculated by Fourier's law of heat conduction.

It is seen from the reviewed studies that using equipment with high spatial and time resolutions, the evolution of the vapor layer thickness distribution under an impacting droplet can be measured either directly or indirectly. This experimental data can be quite helpful to verify transient numerical simulations and analytical solutions.

5. Conclusion

This paper reviews published studies addressing the dynamic LFP temperature of droplet impact on a heated surface. The review is divided into three main sections, one specific to experimental findings of influence factors and the second to theoretical prediction models of the dynamic LFP temperature, and the mechanisms of enhancement or deterioration are also discussed. Other topics addressed are the measurement and modeling of the vapor layer thickness underneath an impacting droplet in the film boiling regime. Key conclusions from this review can be summarized as follows.

Published works:

(1) Numerous experimental investigations have been conducted to study the influences on the dynamic LFP temperature, including impact parameters, fluid properties, surface characteristics, and external environmental conditions. However, considering the diverse working conditions involved in different studies, discrepancies often exist regarding the data trends and the extent of the effects of various influence factors. Some issues, such as the uncertainty concerning the identification of the dynamic LFP temperature, and whether better spreading would cause bubble bursting or vapor layer formation, remain unsolved.

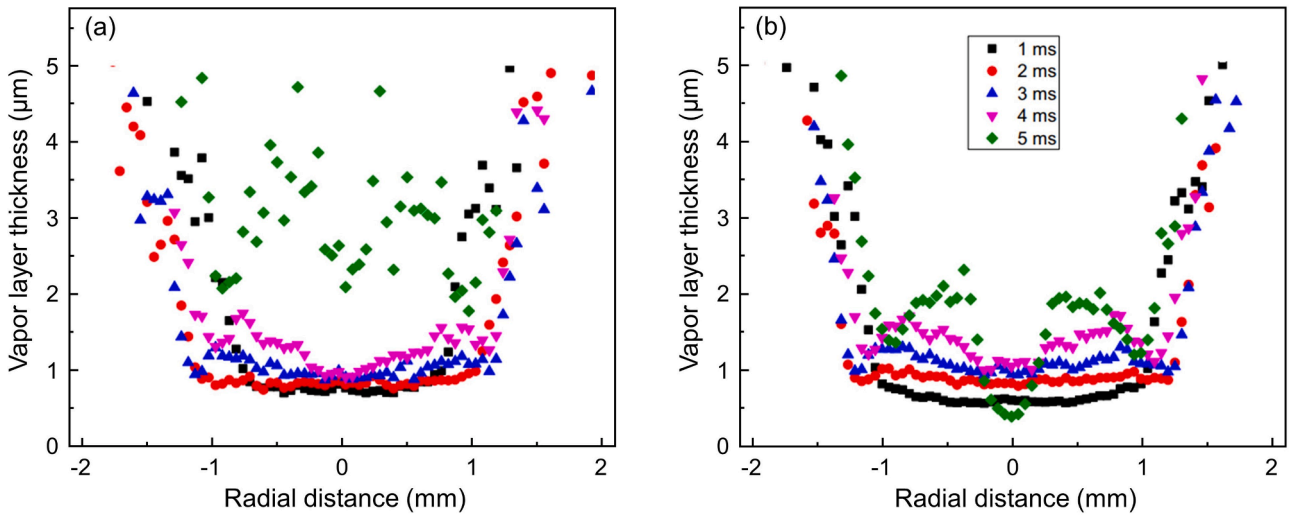

Fig. 27. Radial distribution of vapor layer thickness under an impacting water droplet (We = 6.3). (a) Under the dynamic Leidenfrost condition at $T_w = T_{LFP} =$ 335 °C and (b) in the film boiling regime at $T_w = 370$ °C. Adapted from Jung et al. [40].

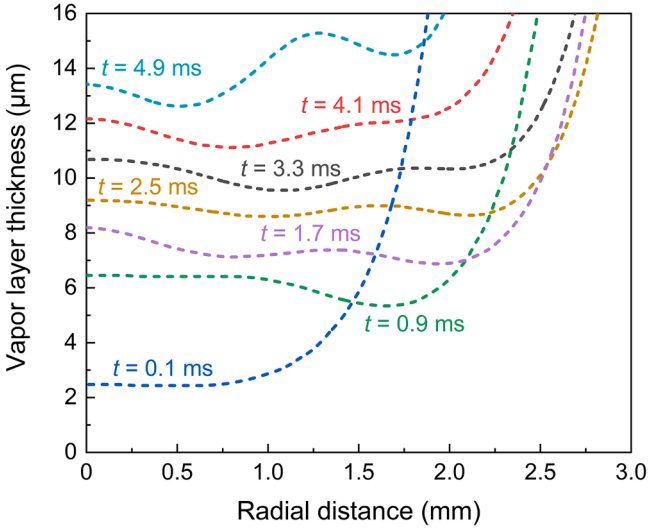

Fig. 28. Spatial and time evolutions of vapor layer thickness under an impacting ethanol droplet (We = 90) at $T_w = 300$ °C. Adapted from Castanet et al. [227].

(2) Due to the inherent complexity of the underlying mechanism, there is a shortage of theoretical modeling work on the dynamic LFP temperature. Overall, four types of model rationales are prevalent in the literature, including the bubble nucleation theory, the transient heat conduction equation, the vapor layer-air layer analogy, and the pressure balance criterion. Among the four models, the pressure balance criterion has received the most attention. Most models are capable of qualitatively predicting the dynamic LFP temperature with the aid of experimental measurement or simulated results. However, only a part of the parameters that affect the dynamic LFP temperature are integrated into these models.

(3) The vapor layer underneath an impacting droplet significantly deteriorates heat transfer, but also induces superior thermal hydrophobicity. The time-varying and spatially nonuniform vapor layer thickness is intrinsically required to predict the dynamic LFP temperature, which is dependent on the surface temperature and on the factors that affect the dynamic LFP temperature.

Recommendatiosn for future work:

(1) The contradictory findings point to a need for future experiments that must be carefully and systematically conducted using various fluid-solid combinations with vastly different thermophysical properties under broad ranges of operating conditions. Microphotographic analysis of the droplet-vapor interfacial features is also recommended, which can be adopted to validate the dynamic LFP temperature mechanisms and models.

(2) Given the complexity of the dynamic LFP temperature and its dependence on a variety of parameters, it is crucial to develop a quantitative model that is based on more insightful physics to fully reveal the mechanisms and validate them with a consolidated database covering wide working conditions.

(3) Since it is particularly difficult to theoretically predict the vapor layer thickness beneath an impacting droplet, new optical diagnostic techniques with high spatial and temporal resolutions are needed to provide detailed capture of vapor layer evolution during the impact process. Such measurements will undoubtedly contribute to elucidating the mechanisms of film boiling heat transfer and dynamic LFP temperature.

Declaration of Competing Interest

The authors declare the following financial interests/personal relationships which may be considered as potential competing interests:

Chang Cai reports financial support was provided by National Natural Science Foundation of China and China Postdoctoral Science Foundation.

Data availability

No data was used for the research described in the article.

Acknowledgement

Financial support from the National Natural Science Foundation of China (Grant No. 52206074) and China Postdoctoral Science Foundation (Grant No. 2023M730464) is gratefully acknowledged.

References

[1] G. Liang, I. Mudawar, Review of drop impact on heated walls, Int. J. Heat Mass Transf. 106 (2017) 103–126.
[2] Z. Wang, J. Xiong, W. Yao, W. Qu, Y. Yang, Experimental investigation on the Leidenfrost phenomenon of droplet impact on heated silicon carbide surfaces, Int. J. Heat Mass Transf. 128 (2019) 1206–1217.
[3] Z. Wang, W. Qu, J. Xiong, M. Zhong, Y. Yang, Investigation on effect of surface properties on droplet impact cooling of cladding surfaces, Nucl. Eng. Technol. 52 (3) (2020) 508–519.
[4] K. Tsukamoto, Y. Kita, S. Inoue, T. Hamanosono, S. Hidaka, S. Ueoka, H. Fukuda, M. Kohno, Y. Takata, On the onset of quench during spray cooling: the significance of oxide layers, Appl. Therm. Eng. 179 (2020), 115682.
[5] S. Chakraborty, I. Sarkar, A. Roshan, S.K. Pal, S. Chakraborty, Spray cooling of hot steel plate using aqueous solution of surfactant and polymer, Therm. Sci. Eng. Prog. 10 (2019) 217–231.
[6] L. Zhang, Q. Duan, X. Meng, K. Jin, J. Xu, J. Sun, Q. Wang, Experimental investigation on intermittent spray cooling and toxic hazards of lithium-ion battery thermal runaway, Energ. Convers. Manag. 252 (2022), 115091.
[7] M. Gupta, A. Pasi, A. Ray, S.R. Kale, An experimental study of the effects of water mist characteristics on pool fire suppression, Exp. Therm. Fluid Sci. 44 (2013) 768–778.
[8] J.M. Tian, B. Chen, Z.F. Zhou, Parametric effect investigation on surface heat transfer performances during cryogen spray cooling, Appl. Therm. Eng. 143 (2018) 767–776.
[9] B. Chen, J. Tian, R. Wang, Z. Zhou, Theoretical study of cryogen spray cooling with R134a, R404A and R1234yf: comparison and clinical potential application, Appl. Therm. Eng. 148 (2019) 1058–1067.
[10] S. Khandekar, G. Sahu, K. Muralidhar, E.Y. Gatapova, O.A. Kabov, R. Hu, X. Luo, L. Zhao, Cooling of high-power LEDs by liquid sprays: challenges and prospects, Appl. Therm. Eng. 184 (2021), 115640.
[11] M. Fabbri, S. Jiang, V.K. Dhir, A comparative study of cooling of high power density electronics using sprays and microjets, J. Heat Transf. 127 (1) (2005) 38–48.
[12] C.Y. Chan, W.B. Lee, H. Wang, Enhancement of surface finish using water-miscible nano-cutting fluid in ultra-precision turning, Int. J. Mach. Tool. Manu. 73 (2013) 62–70.
[13] C. Cen, H. Wu, C.f. Lee, L. Fan, F. Liu, Experimental investigation on the sputtering and micro-explosion of emulsion fuel droplets during impact on a heated surface, Int. J. Heat Mass Transf. 132 (2019) 130–137.
[14] H. Jadidbonab, I. Malgarinos, I. Karathanassis, N. Mitroglou, M. Gavaises, We-T classification of diesel fuel droplet impact regimes, P. Roy. Soc. A Math. Phy. 474 (2215) (2018), 20170759.
[15] A. Tuoliken, L. Zhou, P. Bai, X. Du, On the Leidenfrost effect of water droplet impacting on superalloy plate surface, Int. J. Heat Mass Transf. 172 (2021), 121218.
[16] C. Kuhn, D. Schweigert, C. Kuntz, M. Börnhorst, Single droplet impingement of urea water solution on heated porous surfaces, Int. J. Heat Mass Transf. 181 (2021), 121836.
[17] A.P. Kulkarni, T. Megaritis, L.C. Ganippa, Impact dynamics and morphology of urea-water-solution droplets impinging on a hot plate under urea-SCR relevant conditions: influence of surface tension, Fuel 298 (2021), 120671.
[18] B. Sobac, A. Rednikov, S. Dorbolo, P. Colinet, Self-propelled Leidenfrost drops on a thermal gradient: a theoretical study, Phys. Fluids 29 (8) (2017), 082101.
[19] H. Linke, B.J. Alemán, L.D. Melling, M.J. Taormina, M.J. Francis, C.C. Dow-Hygelund, V. Narayanan, R.P. Taylor, A. Stout, Self-propelled Leidenfrost droplets, Phys. Rev. Lett. 96 (15) (2006), 154502.
[20] T.R. Cousins, R.E. Goldstein, J.W. Jaworski, A.I. Pesci, A ratchet trap for Leidenfrost drops, J. Fluid Mech. 696 (2012) 215–227.
[21] C. Cheng, M. Guy, A. Narduzzo, K. Takashina, The Leidenfrost maze, Eur. J. Phys. 36 (3) (2015), 035004.
[22] P. Agrawal, G.G. Wells, R. Ledesma-Aguilar, G. McHale, A. Buchoux, A. Stokes, K. Sefiane, Leidenfrost heat engine: sustained rotation of levitating rotors on turbine-inspired substrates, Appl. Energy 240 (2019) 399–408.
[23] R. Abdelaziz, D. Disci-Zayed, M.K. Hedayati, J.H. Pöhls, A.U. Zillohu, B. Erkartal, V.S.K. Chakravadhanula, V. Duppel, L. Kienle, M. Elbahri, Green chemistry and nanofabrication in a levitated Leidenfrost drop, Nat. Commun. 4 (1) (2013) 1–10.
[24] B.T. Ng, Z.Y. Lim, Y.M. Hung, M.K. Tan, Phase change modulated thermal switch and enhanced performance enabled by graphene coating, RSC Adv. 6 (90) (2016) 87159–87168.
[25] R.M. Bain, C.J. Pulliam, F. Thery, R.G. Cooks, Accelerated chemical reactions and organic synthesis in Leidenfrost droplets, Angew. Chem. Int. Edit. 55 (35) (2016) 10478–10482.
[26] B.T. Ng, Y.M. Hung, M.K. Tan, Vibration isolation via Leidenfrost droplets, J. Micromech. Microeng. 29 (8) (2019), 085003.
[27] J. Song, W. Cheng, M. Nie, X. He, W. Nam, J. Cheng, W. Zhou, Partial leidenfrost evaporation-assisted ultrasensitive surface-enhanced Raman spectroscopy in a Janus water droplet on hierarchical plasmonic micro-/nanostructures, ACS Nano 14 (8) (2020) 9521–9531.
[28] J.G. Leidenfrost, On the fixation of water in diverse fire, Int. J. Heat Mass Transf. 9 (11) (1966) 1153–1166.
[29] J. Wang, M. Liu, R. Ma, Q. Wang, L. Jiang, In situ wetting state transition on micro- and nanostructured surfaces at high temperature, ACS Appl. Mater. Inter. 6 (17) (2014) 15198–15208.
[30] H. Chaves, A.M. Kubitzek, F. Obermeier, Dynamic processes occurring during the spreading of thin liquid films produced by drop impact on hot walls, Int. J. Heat Fluid Flow 20 (5) (1999) 470–476.
[31] H. Chaves, A.M. Kubitzek, F. Obermeier, Transient phenomena during drop impact on heated walls, Trans. Phenom. Multiph. Multicomp. Syst. (2000) 179–194.
[32] S.C. Yao, K.Y. Cai, The dynamics and Leidenfrost temperature of drops impacting on a hot surface at small angles, Exp. Therm. Fluid Sci. 1 (4) (1988) 363–371.
[33] M. Khavari, T. Tran, Universality of oscillating boiling in Leidenfrost transition, Phys. Rev. E 96 (4) (2017), 043102.
[34] V. Bertola, K. Sefiane, Controlling secondary atomization during drop impact on hot surfaces by polymer additives, Phys. Fluids 17 (10) (2005), 108104.
[35] M. Auliano, M. Fernandino, P. Zhang, C.A. Dorao, Water droplet impacting on overheated random si nanowires, Int. J. Heat Mass Transf. 124 (2018) 307–318.
[36] S.H. Kim, H. Seon Ahn, J. Kim, M. Kaviany, M. Hwan Kim, Dynamics of water droplet on a heated nanotubes surface, Appl. Phys. Lett. 102 (23) (2013), 233901.
[37] S.H. Kim, H.S. Ahn, J. Kim, M.H. Kim, H.S. Park, Experimental study of water droplets on over-heated nano/microstructured zirconium surfaces, Nucl. Eng. Des. 278 (2014) 367–376.
[38] H. Staat, T. Tran, B. Geerdink, G. Riboux, C. Sun, J.M. Gordillo, D. Lohse, Phase diagram for droplet impact on superheated surfaces, J. Fluid Mech. 779 (2015) 1–12.
[39] Y. Wang, A. El Bouhali, S. Lyu, L. Yu, Y. Hao, Z. Zuo, S. Liu, C. Sun, Leidenfrost drop impact on inclined superheated substrates, Phys. Fluids 32 (11) (2020), 112113.
[40] J. Jung, S. Jeong, H. Kim, Investigation of single-droplet/wall collision heat transfer characteristics using infrared thermometry, Int. J. Heat Mass Transf. 92 (2016) 774–783.
[41] M. Shirota, M.A.J. van Limbeek, C. Sun, A. Prosperetti, D. Lohse, Dynamic Leidenfrost effect: relevant time and length scales, Phys. Rev. Lett. 116 (6) (2016), 064501.
[42] S.H. Lee, K. Harth, M. Rump, M. Kim, D. Lohse, K. Fezzaa, J.H. Je, Drop impact on hot plates: contact times, lift-off and the lamella rupture, Soft Matter 16 (34) (2020) 7935–7949.
[43] M. Khavari, C. Sun, D. Lohse, T. Tran, Fingering patterns during droplet impact on heated surfaces, Soft Matter 11 (17) (2015) 3298–3303.
[44] R. Wu, O. Lamini, C.Y. Zhao, Leidenfrost temperature: surface thermal diffusivity and effusivity effect, Int. J. Heat Mass Transf. 168 (2021), 120892.
[45] V. Bertola, An impact regime map for water drops impacting on heated surfaces, Int. J. Heat Mass Transf. 85 (2015) 430–437.
[46] Q. Ma, X. Wu, T. Li, Droplet impact on superheated surfaces with different wettabilities, Int. J. Heat Mass Transf. 141 (2019) 1181–1186.
[47] H. Chen, W. Cheng, Y. Peng, L. Jiang, Dynamic Leidenfrost temperature increase of impacting droplets containing high-alcohol surfactant, Int. J. Heat Mass Transf. 118 (2018) 1160–1168.
[48] C. Cai, H. Liu, H. Chen, C. Si, Alcohol-induced elevation in the dynamic Leidenfrost point temperature for water droplet impact, Int. J. Heat Mass Transf. 215 (2023), 124483.
[49] T. Tran, H.J.J. Staat, A. Prosperetti, C. Sun, D. Lohse, Drop impact on superheated surfaces, Phys. Rev. Lett. 108 (3) (2012), 036101.
[50] J.D. Bernardin, I. Mudawar, The Leidenfrost point: experimental study and assessment of existing models, J. Heat Transf. 121 (4) (1999) 894–903.
[51] L. Zhong, Z. Guo, Effect of surface topography and wettability on the Leidenfrost effect, Nanoscale 9 (19) (2017) 6219–6236.
[52] V. Talari, P. Behar, Y. Lu, E. Haryadi, D. Liu, Leidenfrost drops on micro/nanostructured surfaces, Front. Energy 12 (1) (2018) 22–42.
[53] D. Quéré, Leidenfrost dynamics, Annu. Rev. Fluid Mech. 45 (2013) 197–215.
[54] X. Yu, Y. Zhang, R. Hu, X. Luo, Water droplet bouncing dynamics, Nano Energy 81 (2021), 105647.
[55] G. Wang, J.R. McDonough, V. Zivkovic, T. Long, S. Wang, From thermal energy to kinetic energy: droplet motion triggered by the Leidenfrost effect, Adv. Mater. Interfaces 8 (2) (2021), 2001249.
[56] S.M. Stewart, Leidenfrost drop dynamics: a forgotten past and modern day rediscoveries, Eur. J. Phys. 43 (2) (2022), 023001.
[57] C. Josserand, S.T. Thoroddsen, Drop impact on a solid surface, Annu. Rev. Fluid Mech. 48 (2016) 365–391.
[58] D. Kwon, D. Kang, E. Yeom, Impact and boiling characteristics of an impinging ethanol drop on a heated Al alloy surface, Int. J. Heat Mass Transf. 169 (2021), 120927.
[59] L. Liu, Y. Zhang, G. Cai, P.A. Tsai, High-speed dynamics and temperature variation during drop impact on a heated surface, Int. J. Heat Mass Transf. 189 (2022), 122710.
[60] J. Park, D.E. Kim, Dynamic Leidenfrost behaviors of different fluid drops on superheated surface: scaling for vapor film thickness, Phys. Fluids 31 (10) (2019), 101702.
[61] J. Park, E.K. Dong, Dynamics of liquid drops levitating on superheated surfaces, Int. J. Therm. Sci. 152 (2020), 106321.
[62] D.T. Gonzalez Recio, Influence of Fluids Properties and Droplet Impinging Height On Leidenfrost Phenomena Over a Plain Silicon Surface, Norwegian University of Science and Technology, 2017.
[63] M.A.J. van Limbeek, T.H. Nes, S. Vanapalli, Impact dynamics and heat transfer characteristics of liquid nitrogen drops on a sapphire prism, Int. J. Heat Mass Transf. 148 (2020), 118999.
[64] S.L. Manzello, J.C. Yang, On the collision dynamics of a water droplet containing an additive on a heated solid surface, P. Roy. Soc. A Math. Phy. 458 (2026) (2002) 2417–2444.

[65] G. Castanet, T. Liénart, F. Lemoine, Dynamics and temperature of droplets impacting onto a heated wall, Int. J. Heat Mass Transf. 52 (3–4) (2009) 670–679.
[66] N. Nagai, T. Matsumura, S. Yamaguchi, Y. Maeda, K. Ikebata, Liquid-solid contact at evaporation of water liquid droplet emulsified with lubricant and its adhesion situation, in: Proceedings of the 14th International Heat Transfer Conferences, 2010, pp. 815–821.
[67] S. Sen, V. Vaikuntanathan, D. Sivakumar, Impact dynamics of alternative jet fuel drops on heated stainless steel surface, Int. J. Therm. Sci. 121 (2017) 99–110.
[68] M. Börnhorst, O. Deutschmann, Single droplet impingement of urea water solution on a heated substrate, Int. J. Heat Fluid Flow 69 (2018) 55–61.
[69] M. Zhang, J. Zhu, Z. Tao, L. Qiu, A quantitative phase diagram of droplet impingement boiling, Int. J. Heat Mass Transf. 177 (2021), 121535.
[70] A. Chausalkar, S.C. Kong, J.B. Michael, Multicomponent drop breakup during impact with heated walls, Int. J. Heat Mass Transf. 141 (2019) 685–695.
[71] A.B. Wang, C.H. Lin, C.C. Chen, The critical temperature of dry impact for tiny droplet impinging on a heated surface, Phys. Fluids 12 (6) (2000) 1622–1625.
[72] A.B. Wang, C.H. Lin, C.C. Cheng, Pattern analysis of a single droplet impinging onto a heated plate, Heat Transf. Asian Research 34 (8) (2005) 579–594.
[73] G.P. Celata, M. Cumo, A. Mariani, G. Zummo, Visualization of the impact of water drops on a hot surface: effect of drop velocity and surface inclination, in: Heat Mass Transf., 42, 2006, p. 885.
[74] U. Mezbah, S. Yoshida, S. Someya, O. Koji, Visualization of transient interaction phenomena between droplets and hot walls around Leidenfrost temperature for SUS304, in: Proceedings of the International Conference on Industrial & Mechanical Engineering, Dhaka, Bangladesh, 2007, pp. 1–5.
[75] E. Kompinsky, G. Dolan, E. Sher, Experimental study on the dynamics of binary fuel droplet impacts on a heated surface, Chem. Eng. Sci. 98 (2013) 186–194.
[76] W. Tong, L. Qiu, J. Jin, L. Sun, F. Duan, Unique lift-off of droplet impact on high temperature nanotube surfaces, Appl. Phys. Lett. 111 (9) (2017), 091605.
[77] S. Jowkar, M.R. Morad, Water drop impact on a semi-cylindrical convex hot surface for a diameter ratio of unity, Exp. Therm. Fluid Sci. 106 (2019) 68–77.
[78] S. Jowkar, M.R. Morad, Rebounding suppression of droplet impact on hot surfaces: effect of surface temperature and concaveness, Soft Matter 15 (5) (2019) 1017–1026.
[79] S. Jowkar, M. Jafari, M.R. Morad, Heat transfer characteristics of high flow rate electrospray and droplet cooling, Appl. Therm. Eng. 162 (2019), 114239.
[80] P. Dhar, S.R. Mishra, A. Gairola, D. Samanta, Delayed Leidenfrost phenomenon during impact of elastic fluid droplets, P. Roy. Soc. A Math. Phy. 476 (2243) (2020), 20200556.
[81] G.V.V.S.V. Prasad, P. Dhar, D. Samanta, Postponement of dynamic Leidenfrost phenomenon during droplet impact of surfactant solutions, Int. J. Heat Mass Transf. 189 (2022), 122675.
[82] J. Luo, S.Y. Wu, L. Xiao, S.Y. Zhou, Z.L. Chen, Transient boiling heat transfer mechanism of droplet impacting heated cylinder, Int. J. Mech. Sci. 233 (2022), 107675.
[83] G.V.V. Prasad, M. Yadav, P. Dhar, D. Samanta, Morphed inception of dynamic Leidenfrost regime in colloidal dispersion droplets, Phys. Fluids 35 (1) (2023), 012107.
[84] G.V.V.S. Vara Prasad, H. Sharma, N. Nirmalkar, P. Dhar, D. Samanta, Augmenting the Leidenfrost temperature of droplets via nanobubble dispersion, Langmuir 38 (51) (2022) 15925–15936.
[85] O. Lamini, R. Wu, C. Zhao, Experimental study on the effect of the liquid/surface thermal properties on droplet impact, Therm. Sci. 25 (1 Part B) (2021) 705–716.
[86] W. Zhang, T. Yu, J. Fan, W. Sun, Z. Cao, Droplet impact behavior on heated micro-patterned surfaces, J. Appl. Phys. 119 (11) (2016), 114901.
[87] C.E. Clavijo, J. Crockett, D. Maynes, Hydrodynamics of droplet impingement on hot surfaces of varying wettability, Int. J. Heat Mass Transf. 108 (2017) 1714–1726.
[88] D. Zhou, Y. Zhang, Y. Hou, X. Zhong, J. Jin, L. Sun, Film levitation and central jet of droplet impact on nanotube surface at superheated conditions, Phys. Rev. E 102 (4) (2020), 043108.
[89] J.D. Bernardin, C.J. Stebbins, I. Mudawar, Effects of surface roughness on water droplet impact history and heat transfer regimes, Int. J. Heat Mass Transf. 40 (1) (1996) 73–88.
[90] J.D. Bernardin, C.J. Stebbins, I. Mudawar, Mapping of impact and heat transfer regimes of water drops impinging on a polished surface, Int. J. Heat Mass Transf. 40 (2) (1997) 247–267.
[91] J. Senda, K. Yamada, H. Fujimoto, H. Miki, The heat-transfer characteristics of a small droplet impinging upon a hot surface, JSME Int. J. 31 (1) (1988) 105–111.
[92] Y. Zhang, M. Zhang, J. Zhu, Z. Tao, L. Qiu, Elevating Leidenfrost temperature by orderly droplet stream impingement boiling, Int. J. Heat Mass Transf. 194 (2022), 122976.
[93] L. Rayleigh, On the capillary phenomena of jets, P. Roy. Soc. A Math. Phy. 29 (196–199) (1879) 71–97.
[94] B. Zabala, A. Igartua, V. Scarpis, G. Timelli, F. Girot, R. Nevshupa, Multiparametric study of Leidenfrost point and wettability of lubricants on high-pressure die-casting dies, Int. J. Therm. Sci. 125 (2018) 66–73.
[95] Z. Tamura, Y. Tanasawa, Evaporation and combustion of a drop contacting with a hot surface, Symp. Int. Combust. 7 (1959) 509–522.
[96] T.Y. Xiong, M.C. Yuen, Evaporation of a liquid droplet on a hot plate, Int. J. Heat Mass Transf. 34 (7) (1991) 1881–1894.
[97] W. Deng, A. Gomez, The role of electric charge in microdroplets impacting on conducting surfaces, Phys. Fluids 22 (5) (2010), 051703.
[98] S.M. Sajadi, P. Irajizad, V. Kashyap, N. Farokhnia, H. Ghasemi, Surfaces for high heat dissipation with no Leidenfrost limit, Appl. Phys. Lett. 111 (2) (2017), 021605.
[99] G.C. Lee, S.H. Kim, J.y. Kang, M.H. Kim, H. Jo, Leidenfrost temperature on porous wick surfaces: decoupling the effects of the capillary wicking and thermal properties, Int. J. Heat Mass Transf. 145 (2019), 118809.
[100] E. Marin, Thermal physics concepts: the role of the thermal effusivity, Phys. Teach. 44 (7) (2006) 432–434.
[101] K.J. Baumeister, F.F. Simon, Leidenfrost temperature—Its correlation for liquid metals, cryogens, hydrocarbons, and water, J. Heat Transf. 95 (2) (1973) 166–173.
[102] M.A.J. Van Limbeek, P.B.J. Hoefnagels, C. Sun, D. Lohse, Origin of spray formation during impact on heated surfaces, Soft Matter 13 (41) (2017) 7514–7520.
[103] M. Limbeek, M. Shirota, P. Sleutel, S. Chao, A. Prosperetti, D. Lohse, Vapour cooling of poorly conducting hot substrates increases the dynamic Leidenfrost temperature, Int. J. Heat Mass Transf. 97 (2016) 101–109.
[104] S.Y. Misyura, Wall effect on heat transfer crisis, Exp. Therm. Fluid Sci. 70 (2016) 389–396.
[105] S.Y. Misyura, The effect of Weber number, droplet sizes and wall roughness on crisis of droplet boiling, Exp. Therm. Fluid Sci. 84 (2017) 190–198.
[106] C. Cai, I. Mudawar, H. Liu, C. Si, Theoretical Leidenfrost point (LFP) model for sessile droplet, Int. J. Heat Mass Transf. 146 (2020), 118802.
[107] G.C. Lee, J.y. Kang, H.S. Park, K. Moriyama, S.H. Kim, M.H. Kim, Induced liquid-solid contact via micro/nano multiscale texture on a surface and its effect on the Leidenfrost temperature, Exp. Therm. Fluid Sci. 84 (2017) 156–164.
[108] L. Guo, Y. Chen, N. Cai, W. Sun, Y. Yan, H. Wang, Y. Gao, Dynamic behaviors of fuel droplets impacting on the wall surfaces with different wettability and temperatures, Appl. Therm. Eng. 212 (2022), 118536.
[109] C.T. Avedisian, J. Koplik, Leidenfrost boiling of methanol droplets on hot porous/ceramic surfaces, Int. J. Heat Mass Transf. 30 (2) (1987) 379–393.
[110] S. Chandra, C.T. Avedisian, Observations of droplet impingement on a ceramic porous surface, Int. J. Heat Mass Transf. 35 (10) (1992) 2377–2388.
[111] N. Lipson, S. Chandra, Cooling of porous metal surfaces by droplet impact, Int. J. Heat Mass Transf. 152 (2020), 119494.
[112] W.S. Kim, S.Y. Lee, Behavior of a water drop impinging on heated porous surfaces, Exp. Therm. Fluid Sci. 55 (2014) 62–70.
[113] P. Zhao, G.K. Hargrave, H.K. Versteeg, C.P. Garner, B.A. Reid, E.J. Long, H. Zhao, The dynamics of droplet impact on a heated porous surface, Chem. Eng. Sci. 190 (2018) 232–247.
[114] X.W. Wang, J.Y. Ho, K.C. Leong, An experimental investigation of single droplet impact cooling on hot enhanced surfaces fabricated by selective laser melting, Int. J. Heat Mass Transf. 120 (2018) 652–670.
[115] T. Tran, H. Staat, A. Susarrey-Arce, T.C. Foertsch, A.V. Houselt, H. Gardeniers, A. Prosperetti, D. Lohse, C. Sun, Droplet impact on superheated micro-structured surfaces, Soft Matter 9 (12) (2013) 3272–3282.
[116] J. Li, Y. Hou, Y. Liu, C. Hao, M. Li, M.K. Chaudhury, S. Yao, Z. Wang, Directional transport of high-temperature Janus droplets mediated by structural topography, Nat. Phys. 12 (6) (2016) 606–612.
[117] T. Zhang, J. Wang, L. Chen, J. Zhai, Y. Song, L. Jiang, High-temperature wetting transition on micro- and nanostructured surfaces, Angew. Chem. Int. Edit. 123 (23) (2011) 5423–5426.
[118] I.W. Park, M. Fernandino, C.A. Dorao, Effect of micropillar characteristics on Leidenfrost temperature of impacting droplets, in: Proceedings of the ASME 15th International Conference on Nanochannels, Microchannels, and Minichannels, 2016. American Society of Mechanical Engineers, American Society of Mechanical EngineersV001T009A001.
[119] M. Auliano, M. Fernandino, P. Zhang, C.A. Dorao, The Leidenfrost phenomenon on sub-micron tapered pillars, in: Proceedings of the ASME 15th International Conference on Nanochannels, Microchannels, and Minichannels, 2017. American Society of Mechanical Engineers, American Society of Mechanical Engineers Digital Collection.
[120] J. Park, D.E. Kim, Droplet dynamics on superheated surfaces with circular micropillars, Int. J. Heat Mass Transf. 142 (2019), 118459.
[121] J. Park, D.E. Kim, Dynamic Leidenfrost temperature of saturated water drops on textured surfaces, Int. J. Heat Mass Transf. 150 (2020), 119298.
[122] S.C. Park, M.H. Kim, D.I. Yu, H.S. Ahn, Geometrical parametric study of drop impingement onto heated surface with micro-pillar arrays, Int. J. Heat Mass Transf. 168 (2021), 120891.
[123] D.E. Kim, Dynamic Leidenfrost temperature behaviors on uniformly distributed micropillars, Exp. Therm. Fluid Sci. 111 (2020), 109954.
[124] S.H. Kim, G. Lee, H. Kim, M.H. Kim, Leidenfrost point and droplet dynamics on heated micropillar array surface, Int. J. Heat Mass Transf. 139 (2019) 1–9.
[125] M. Wei, Y. Song, Y. Zhu, D.J. Preston, C.S. Tan, E.N. Wang, Heat transfer suppression by suspended droplets on microstructured surfaces, Appl. Phys. Lett. 116 (23) (2020), 233703.
[126] D.W. Jerng, D.E. Kim, Dynamic Leidenfrost temperature on micro-textured surfaces: acoustic wave absorption into thin vapor layer, Appl. Phys. Lett. 112 (5) (2018), 053902.
[127] S. Ogata, R. Nakanishi, Effect of surface textures and wettability on droplet impact on a heated surface, Processes 9 (2) (2021) 350.
[128] Q. Cao, Y. Chen, Leidenfrost temperature on trapezoidal grooved surface, Energies 15 (8) (2022) 2875.
[129] Y. Guo, X. Liu, J. Ji, Z. Wang, X. Hu, Y. Zhu, T. Zhang, T. Tao, K. Liu, Y. Jiao, Delayed Leidenfrost effect of a cutting droplet on a microgrooved tool surface, Langmuir (2023).
[130] R.L. Agapov, J.B. Boreyko, D.P. Briggs, B.R. Srijanto, S.T. Retterer, C.P. Collier, N. V. Lavrik, Asymmetric wettability of nanostructures directs Leidenfrost droplets, ACS Nano 8 (1) (2014) 860–867.

[131] C.M. Weickgenannt, Y. Zhang, S. Sinha-Ray, I.V. Roisman, T. Gambaryan-Roisman, C. Tropea, A.L. Yarin, Inverse-Leidenfrost phenomenon on nanofiber mats on hot surfaces, Phys. Rev. E 84 (3) (2011), 036310.
[132] S. Sinha-Ray, Y. Zhang, A.L. Yarin, Thorny devil nanotextured fibers: the way to cooling rates on the order of 1kW/cm2, Langmuir 27 (1) (2011) 215–226.
[133] H. Nair, H.J.J. Staat, T. Tran, A. van Houselt, A. Prosperetti, D. Lohse, C. Sun, The Leidenfrost temperature increase for impacting droplets on carbon-nanofiber surfaces, Soft Matter 10 (13) (2014) 2102–2109.
[134] M. Auliano, M. Fernandino, P. Zhang, C.A. Dorao, The Leidenfrost phenomenon on silicon nanowires, in: Proceedings of the International Conference on Nanochannels, Microchannels, and Minichannels (ICNMM), 2016. American Society of Mechanical Engineers, American Society of Mechanical EngineersV001T009A004.
[135] V. Sahoo, C.W. Lo, M.C. Lu, Leidenfrost suppression and contact time reduction of a drop impacting on silicon nanowire array-coated surfaces, Int. J. Heat Mass Transf. 148 (2020), 118980.
[136] X. Zhong, Y. Zhang, Y. Hou, H. Feng, L. Sun, Unique dynamics of water-ethanol binary droplets impacting onto a superheated surface with nanotubes, Int. J. Heat Mass Transf. 164 (2021), 120571.
[137] E. Lim, B.T. Ng, Y.M. Hung, M.K. Tan, Graphene-mediated suppression of Leidenfrost effect for droplets on an inclined surface, Int. J. Therm. Sci. 174 (2022), 107426.
[138] L. Liu, G. Cai, P.A. Tsai, Drop impact on heated nanostructures, Langmuir 36 (34) (2020) 10051–10060.
[139] N. Farokhnia, S.M. Sajadi, P. Irajizad, H. Ghasemi, Decoupled hierarchical structures for suppression of Leidenfrost phenomenon, Langmuir 33 (10) (2017) 2541–2550.
[140] M. Jiang, Y. Wang, F. Liu, H. Du, Y. Li, H. Zhang, S. To, S. Wang, C. Pan, J. Yu, Inhibiting the Leidenfrost effect above 1,000°C for sustained thermal cooling, Nature 601 (7894) (2022) 568–572.
[141] J. Du, Y. Li, X. Wang, X. Wu, Q. Min, Dynamics and heat transfer of water droplets impacting on heated surfaces: the role of surface structures in Leidenfrost point, Int. J. Heat Mass Transf. 212 (2023), 124241.
[142] J. Li, P. Weisensee, Droplet impact and Leidenfrost dynamics on a heated post, Int. J. Heat Mass Transf. 201 (2023), 123581.
[143] R. Chen, M.C. Lu, V. Srinivasan, Z. Wang, H.H. Cho, A. Majumdar, Nanowires for enhanced boiling heat transfer, Nano Lett. 9 (2) (2009) 548–553.
[144] S.H. Kim, J.Y. Kang, H.S. Ahn, H.J. Jo, M.H. Kim, Study of Leidenfrost mechanism in droplet impacting on hydrophilic and hydrophobic surfaces, Int. J. Air Cond. Refri. 21 (04) (2013), 1350028.
[145] S.H. Kim, Y. Jiang, H. Kim, Droplet impact and LFP on wettability and nanostructured surface, Exp. Therm. Fluid Sci. 99 (2018) 85–93.
[146] Y. Takata, S. Hidaka, A. Yamashita, H. Yamamoto, Evaporation of water drop on a plasma-irradiated hydrophilic surface, Int. J. Heat Fluid Flow 25 (2) (2004) 320–328.
[147] Y. Takata, S. Hidaka, J.M. Cao, T. Nakamura, H. Yamamoto, M. Masuda, T. Ito, Effect of surface wettability on boiling and evaporation, Energy 30 (2–4) (2005) 209–220.
[148] Q. Ma, X. Wu, T. Li, F. Chu, Droplet boiling on heated surfaces with various wettabilities, Appl. Therm. Eng. 167 (2020), 114703.
[149] Y. Chen, L. Guo, N. Cai, W. Sun, Y. Yan, D. Li, H. Wang, R. Xuan, Evaporation characteristics and morphological evolutions of fuel droplets after hitting different wettability surfaces, J. Bionic Eng. (2022) 1–14.
[150] C.T. Huang, C.W. Lo, M.C. Lu, Reducing contact time of droplets impacting superheated hydrophobic surfaces, Small 18 (13) (2022), 2106704.
[151] H. Jadidbonab, N. Mitroglou, I. Karathanassis, M. Gavaises, Experimental study of diesel-fuel droplet impact on a similarly sized polished spherical heated solid particle, Langmuir 34 (1) (2018) 36–49.
[152] C. Guo, Y. Sun, D. Zhao, Experimental study of droplet impact on superheated cylindrical surfaces, Exp. Therm. Fluid Sci. 121 (2021), 110263.
[153] S.J. Lee, J.H. Cha, K.M. Kim, W. Choi, Dynamics of drop impact on heated metal wires: thermally induced transition from tail to splash to jumping modes, Int. J. Heat Mass Transf. 131 (2019) 226–236.
[154] Y.M. Arifin, M. Arai, The effect of hot surface temperature on diesel fuel deposit formation, Fuel 89 (5) (2010) 934–942.
[155] A. Chausalkar, C.B.M. Kweon, J.B. Michael, Multi-component fuel drop-wall interactions at high ambient pressures, Fuel 283 (2021), 119071.
[156] Z. Zhao, X. Huang, H. Sheng, Z. Chen, H. Liu, Promoted stable combustion of alcohol-based fuel accompanied by inhibition of Leidenfrost effect in a wide temperature range, Energy 234 (2021), 121248.
[157] T. Kudra, Y.K. Pan, A.S. Mujumdar, Evaporation from single droplets impinging on heated surfaces, Drying Technol. 9 (3) (1991) 693–707.
[158] U. Sen, T. Roy, R. Ganguly, L.A. Angeloni, W.A. Schroeder, C.M. Megaridis, Explosive behavior during binary-droplet impact on superheated substrates, Int. J. Heat Mass Transf. 154 (2020), 119658.
[159] R. Raj, C. Kunkelmann, P. Stephan, J. Plawsky, J. Kim, Contact line behavior for a highly wetting fluid under superheated conditions, Int. J. Heat Mass Transf. 55 (9) (2012) 2664–2675.
[160] B. Horacek, K.T. Kiger, J. Kim, Single nozzle spray cooling heat transfer mechanisms, Int. J. Heat Mass Transf. 48 (8) (2005) 1425–1438.
[161] Q. Cui, S. Chandra, S. McCahan, The effect of dissolving gases or solids in water droplets boiling on a hot surface, J. Heat Transf. 123 (4) (2001) 719–728.
[162] J.S. Bjørge, S.A. Bjørkheim, M.M. Metallinou, T. Log, Ø. Frette, Influence of acetone and sodium chloride additives on cooling efficiency of water droplets impinging onto hot metal surfaces, Energies 12 (12) (2019) 2358.
[163] J. Zhu, X. Chen, J. Sheng, S. Li, T. Lu, X. Chen, Hydrodynamics and crystallization of NaCl aqueous solution droplet impact on heated surface, Appl. Therm. Eng. 219 (2023), 119670.
[164] C.K. Huang, V.P. Carey, The effects of dissolved salt on the Leidenfrost transition, Int. J. Heat Mass Transf. 50 (1–2) (2007) 269–282.
[165] M. Low, W.S. Sow, Y.M. Hung, M.K. Tan, Increase in Leidenfrost point via plasma-activated water, Int. J. Therm. Sci. 184 (2023), 107908.
[166] A. Kumar, D.K. Mandal, Impact of emulsion drops on a plane solid: effect of composition and wall temperature, in: Heat Mass Transf., 58, 2022, pp. 505–529.
[167] K. Nabbout, M. Sommerfeld, E. Uhlmann, E. Barth, J. Kuhnert, Interaction of cooling lubricant droplets with hot metal surfaces, in: Proceedings of the 7th World Congress of Momentum, Heat and Mass Transfer (MHMT'22, 2022, p. 154.
[168] M.G. Joksimovic, J.B. Schmidt, I.V. Roisman, C. Tropea, J. Hussong, Impact of a suspension drop onto a hot substrate: diminution of splash and prevention of film boiling, Soft Matter 19 (7) (2023) 1440–1453.
[169] T.J. Mach, R.L. Sung, P.M. Liiva, W.P. Acker, J.C. Swindal, R.K. Chang, Experimental determination of fuel additive effects on Leidenfrost temperature and deposit formation, 930774, SAE Technical Paper, 1993.
[170] Y.M. Qiao, S. Chandra, Experiments on adding a surfactant to water drops boiling on a hot surface, P. Roy. Soc. A Math. Phys. 453 (1959) 673–689, 1997.
[171] P. Zhang, B. Peng, X. Yang, J. Wang, L. Jiang, Regulating droplet dynamic wetting behaviors using surfactant additives on high-temperature surfaces, Adv. Mater. Interfaces 7 (14) (2020), 2000501.
[172] Z. Cai, B. Wang, S. Liu, H. Li, S. Luo, Z. Dong, Y. Wang, Enhancing boiling heat transfer on a superheated surface by surfactant-laden droplets, Langmuir 38 (34) (2022) 10375–10384.
[173] V. Bertola, Drop impact on a hot surface: effect of a polymer additive, Exp. Fluid 37 (5) (2004) 653–664.
[174] B. Li, L. Chen, S. Joo, Impact dynamics of newtonian and viscoelastic droplets on heated surfaces at low Weber number, Case Stud. Therm. Eng. 26 (2021), 101109.
[175] G. Paul, P.K. Das, I. Manna, Nanoparticle deposition from nanofluid droplets during Leidenfrost phenomenon and consequent rise in transition temperature, Int. J. Heat Mass Transf. 148 (2020), 119110.
[176] L. Ulahannan, K. Krishnakumar, A.R. Nair, S.K. Ranjith, An experimental study on the effect of nanoparticle shape on the dynamics of Leidenfrost droplet impingement, Exp. Comp. Multiph. Flow 3 (1) (2021) 47–58.
[177] D. Orejon, K. Sefiane, Y. Takata, Effect of ambient pressure on Leidenfrost temperature, Phys. Rev. E 90 (5) (2014), 053012.
[178] F. Celestini, T. Frisch, Y. Pomeau, Room temperature water Leidenfrost droplets, Soft Matter 9 (40) (2013) 9535–9538.
[179] R.H. Stanglmaier, C.E. Roberts, C.A. Moses, Vaporization of individual fuel drops on a heated surface: a study of fuel-wall interactions within direct-injected gasoline (DIG) engines, SAE Transactions (2002) 1365–1373.
[180] I. Buchmüller, Influence of Pressure On Leidenfrost effect, Technische Universität, 2014.
[181] A. Chausalkar, C. Kweon, S.C. Kong, J.B. Michael, Leidenfrost behavior in drop-wall impacts at combustor-relevant ambient pressures, Int. J. Heat Mass Transf. 153 (2020), 119571.
[182] P. Testa, L. Nicotra, Influence of pressure on the Leidenfrost temperature and on extracted heat fluxes in the transient mode and low pressure, J. Heat Transf. 108 (1986) 916–921.
[183] X. Yu, R. Hu, X. Zhang, B. Xie, X. Luo, Explosive bouncing on heated silicon surfaces under low ambient pressure, Soft Matter 15 (21) (2019) 4320–4325.
[184] M.A.J. Van Limbeek, P.B.J. Hoefnagels, M. Shirota, C. Sun, D. Lohse, Boiling regimes of impacting drops on a heated substrate under reduced pressure, Phys. Rev. Fluids 3 (5) (2018), 053601.
[185] L. Maquet, M. Brandenbourger, B. Sobac, A.L. Biance, P. Colinet, S. Dorbolo, Leidenfrost drops: effect of gravity, Europhys. Lett. 110 (2) (2015) 24001.
[186] Y.M. Qiao, S. Chandra, Boiling of droplets on a hot surface in low gravity, Int. J. Heat Mass Transf. 39 (7) (1996) 1379–1393.
[187] Y.M. Qiao, S. Chandra, Impact of n-heptane droplets on a hot surface in low gravity, T. Can. Soc. Mech. Eng. 19 (3) (1995) 271–284.
[188] B.T. Ng, Y.M. Hung, M.K. Tan, Suppression of the Leidenfrost effect via low frequency vibrations, Soft Matter 11 (4) (2014) 775–784.
[189] O. Ozkan, V. Bahadur, Electrical impedance-based characterization of electrostatic suppression of the Leidenfrost state, Appl. Phys. Lett. 114 (15) (2019), 153701.
[190] Y. Lu, J. Bao, D. Liu, An experimental and theoretical investigation of electrostatic suppression of the Leidenfrost state, Int. J. Heat Mass Transf. 170 (2021), 121036.
[191] A. Shahriari, P.S. Wilson, V. Bahadur, Acoustic detection of electrostatic suppression of the Leidenfrost state, Phys. Rev. E 98 (1) (2018), 013103.
[192] B.T. Ng, Y.M. Hung, M.K. Tan, Acoustically-controlled Leidenfrost droplets, J. Colloid Interface Sci. 465 (2016) 26–32.
[193] H. Xu, J. Wang, K. Yu, B. Li, W. Zhang, L. Zuo, H.B. Kim, Droplet impact on hot substrates under a uniform electric field, Phys. Fluids 34 (9) (2022), 092111.
[194] R.J. Issa, Numerical Modeling of the Dynamics and Heat Transfer of Impacting Sprays For a Wide Range of Pressures, University of Pittsburgh, 2003.
[195] G. Liu, V.S.J. Craig, Macroscopically flat and smooth superhydrophobic surfaces: heating induced wetting transitions up to the Leidenfrost temperature, Faraday Discuss 146 (2010) 141–151.
[196] J.B. Schmidt, J. Hofmann, F.M. Tenzer, J. Breitenbach, C. Tropea, I.V. Roisman, Thermosuperrepellency of a hot substrate caused by vapour percolation, Comm. Phy. 4 (1) (2021) 1–8.
[197] R. Hatakenaka, J. Breitenbach, I.V. Roisman, C. Tropea, Y. Tagawa, Magic carpet breakup of a drop impacting onto a heated surface in a depressurized environment, Int. J. Heat Mass Transf. 145 (2019), 118729.

[198] M. Rein, Interactions Between Drops and Hot surfaces, Drop-surface Interactions, Springer, 2002, pp. 185–217.
[199] P. Chantelot, D. Lohse, Leidenfrost effect as a directed percolation phase transition, Phys. Rev. Lett. 127 (12) (2021), 124502.
[200] P. Chantelot, D. Lohse, Drop impact on superheated surfaces: short-time dynamics and transition to contact, J. Fluid Mech. 928 (2021).
[201] H. Kim, B. Truong, J. Buongiorno, L.W. Hu, Effects of micro/nano-scale surface characteristics on the Leidenfrost point temperature of water, J. Therm. Sci. Technol. 7 (3) (2012) 453–462.
[202] J.D. Bernardin, I. Mudawar, A cavity activation and bubble growth model of the Leidenfrost point, J. Heat Transf. 124 (5) (2002) 864–874.
[203] J.D. Bernardin, I. Mudawar, A Leidenfrost point model for impinging droplets and sprays, J. Heat Transf. 126 (2) (2004) 272–278.
[204] O.G. Engel, Waterdrop collisions with solid surfaces, J. Res. Natl Bur. Stand. 54 (5) (1955) 281–298.
[205] O.G. Engel, Note on particle velocity in collisions between liquid drops and solids, J. Res. Natl Bur. Stand. 64 (6) (1960) 497–498.
[206] G. Castanet, O. Caballina, W. Chaze, R. Collignon, F. Lemoine, The Leidenfrost transition of water droplets impinging onto a superheated surface, Int. J. Heat Mass Transf. 160 (2020), 120126.
[207] G. Castanet, O. Caballina, F. Lemoine, Drop spreading at the impact in the Leidenfrost boiling, Phys. Fluids 27 (6) (2015), 063302.
[208] W. Bouwhuis, R.C.A. van der Veen, T. Tran, D.L. Keij, K.G. Winkels, I.R. Peters, D. van der Meer, C. Sun, J.H. Snoeijer, D. Lohse, Maximal air bubble entrainment at liquid-drop impact, Phys. Rev. Lett. 109 (26) (2012), 264501.
[209] M. Mani, S. Mandre, M.P. Brenner, Events before droplet splashing on a solid surface, J. Fluid Mech. 647 (2010) 163–185.
[210] G. Riboux, J.M. Gordillo, Experiments of drops impacting a smooth solid surface: a model of the critical impact speed for drop splashing, Phys. Rev. Lett. 113 (2) (2014), 024507.
[211] J.M. Gordillo, G. Riboux, The initial impact of drops cushioned by an air or vapour layer with applications to the dynamic Leidenfrost regime, J. Fluid Mech. 941 (2022).
[212] B.I. Nigmatulin, N.I. Vasiliev, V.V. Guguchkin, Interaction between liquid droplets and heated surface, Wärme Stoffübertragung 28 (6) (1993) 313–319.
[213] J. Breitenbach, I.V. Roisman, C. Tropea, Heat transfer in the film boiling regime: single drop impact and spray cooling, Int. J. Heat Mass Transf. 110 (2017) 34–42.
[214] S. Dash, M.T. Alt, S.V. Garimella, Hybrid surface design for robust superhydrophobicity, Langmuir 28 (25) (2012) 9606–9615.
[215] T. Deng, K.K. Varanasi, M. Hsu, N. Bhate, C. Keimel, J. Stein, M. Blohm, Nonwetting of impinging droplets on textured surfaces, Appl. Phys. Lett. 94 (13) (2009), 133109.
[216] J.Yong Park, A. Gardner, W.P. King, D.G. Cahill, Droplet impingement and vapor layer formation on hot hydrophobic surfaces, J. Heat Transf.Transf. 136 (9) (2014), 092902.
[217] G.C. Lee, H. Noh, H.J. Kwak, T.K. Kim, H.S. Park, K. Fezzaa, M.H. Kim, Measurement of the vapor layer under a dynamic Leidenfrost drop, Int. J. Heat Mass Transf. 124 (2018) 1163–1171.
[218] L.H.J. Wachters, H. Bonne, H.J. Van Nouhuis, The heat transfer from a hot horizontal plate to sessile water drops in the spherodial state, Chem. Eng. Sci. 21 (10) (1966) 923–936.
[219] L.H.J. Wachters, N.A.J. Westerling, The heat transfer from a hot wall to impinging water drops in the spheroidal state, Chem. Eng. Sci. 21 (11) (1966) 1047–1056.
[220] M. Rein, The Reflection of Drops Off Hot Surfaces, 79, Zeitschrift für angewandte Mathematik und Mechanik, 1999, pp. 743–744.
[221] Y. Guo, K. Mishima, A non-equilibrium mechanistic heat transfer model for post-dryout dispersed flow regime, Exp. Therm. Fluid Sci. 26 (6–7) (2002) 861–869.
[222] F. Lelong, M. Gradeck, N. Seiler, P. Ruyer, G. Castanet, P. Dunand, Behaviour of liquid droplets bouncing onto a hot slab, in: Proceeding of the 23rd Annual Conference on Liquid Atomization and Spray Systems, Brno, Czech Republic, 2010.
[223] T. Gilet, J.W.M. Bush, Droplets bouncing on a wet, inclined surface, Phys. Fluids 24 (12) (2012), 122103.
[224] S.H. Lee, S.J. Lee, J. San Lee, K. Fezzaa, J.H. Je, Transient dynamics in drop impact on a superheated surface, Phys. Fluids 3 (12) (2018), 124308.
[225] S. Wildeman, C. Sun, Electric field makes Leidenfrost droplets take a leap, Soft Matter 12 (48) (2016) 9622–9632.
[226] L. Mahadevan, Y. Pomeau, Rolling droplets, Phys. Fluids 11 (9) (1999) 2449–2453.
[227] G. Castanet, W. Chaze, O. Caballina, R. Collignon, F. Lemoine, Transient evolution of the heat transfer and the vapor film thickness at the drop impact in the regime of film boiling, Phys. Fluids 30 (12) (2018), 122109.
[228] I.V. Roisman, E. Berberović, C. Tropea, Inertia dominated drop collisions. I. On the universal flow in the lamella, Phys. Fluids 21 (5) (2009), 052103.
[229] S.H. Lee, M. Rump, K. Harth, M. Kim, D. Lohse, K. Fezzaa, J.H. Je, Downward jetting of a dynamic Leidenfrost drop, Phys. Rev. Fluids 5 (7) (2020), 074802.
[230] S. Inada, Y. Miyasaka, K. Sakamoto, K. Hojo, Liquid-solid contact state and fluctuation of the vapor film thickness of a drop impinging on a heated surface, J. Chem. Eng. Jpn. 21 (5) (1988) 463–468.
[231] R.C.A. van der Veen, T. Tran, D. Lohse, C. Sun, Direct measurements of air layer profiles under impacting droplets using high-speed color interferometry, Phys. Rev. E 85 (2012), 026315.
[232] A.L. Biance, C. Clanet, D. Quéré, Leidenfrost drops, Phys. Fluids 15 (6) (2003) 1632–1637.
[233] J. Park, H. Kim, An experimental investigation on dynamics and heat transfer associated with a single droplet impacting on a hot surface above the Leidenfrost point temperature, Kerntechnik 81 (3) (2016) 233–243.
[234] W. Chaze, O. Caballina, G. Castanet, J.F. Pierson, F. Lemoine, D. Maillet, Heat flux reconstruction by inversion of experimental infrared temperature measurements–application to the impact of a droplet in the film boiling regime, Int. J. Heat Mass Transf. 128 (2019) 469–478.